Vysoké učení technické v Brně
Fakulta strojního inženýrství
Ústav konstruování

Brno University of Technology
Faculty of Mechanical Engineering
Institute of Machine and Industrial Design

MAGNETORHEOLOGICAL STRUT FOR VIBRATION ISOLATION SYSTEM OF SPACE LAUNCHER

Ing. Ondřej Macháček
Autor práce
Author

doc. Ing. Ivan Mazůrek, CSc
Vedoucí práce
Supervisor

Disertační práce
Dissertation Thesis

Brno 2018

STATEMENT

I hereby declare that I have written the PhD thesis Magnetorheological Strut for Vibration Isolation System of Space Launcher on my own according to the advice of my supervisor Doc. Ing. Ivan Mazůrek, CSc. and using the sources listed in the references.

Brno, _____ …….

Ondřej Macháček

BIBLIOGRAPHICAL REFERENCE

MACHÁČEK, O. Magnetorheological Strut for Vibration Isolation System of Space Launcher. PhD thesis. Brno University of Technology, Faculty of Mechanical Engineering, Institute of Machine and Industrial Design. Supervisor: Doc. Ing. Ivan Mazůrek, CSc.

ACKNOWLEDGEMENT

I would like to thank my supervisor Doc. Ing. Ivan Mazůrek, CSc. and whole department of condition monitoring for their support and advice during my doctoral study. Special thanks goes to my family for their support during my PhD study.

ABSTRACT

The dissertation thesis deals with the design of magnetorheological (MR) strut for vibration isolation system (VIS) of the launch vehicle. Previously used VIS and their struts are described in state of the art. Each of the struts which contained any fluid was sealed by static seals and elastic bellows made of steel. The strut of a passive system called ELVIS was chosen as an inspiration and therefore analysed thoroughly. The strut is three-parametric that means the damper is elastically connected. The stiffness of this connection is identical to the projection of bellows volumetric stiffness into the axial direction which is called the pressure thrust stiffness.

The method of the pressure thrust stiffness determination from the bellows dimensions is presented in the thesis. Moreover, the parameters which can be used for the modification of the ratio between axial and pressure thrust stiffness of bellows is also discussed. This ratio affects the dynamic behaviour of the strut, thus also the behaviour of whole VIS.

The multi-body model of VIS based on the Stewart platform mechanism and detailed multi-body model of a single strut was created for the prediction of their dynamic behaviour in a vibration environment. Simulations have revealed the parameters which affect the efficiency of the MR strut: the time response and the dynamic force range of the MR valve. The range of these parameters which should ensure an effective vibration isolation by the MR strut in the specific VIS was determined by the multi-body model; specifically, time response: *0-5 ms* and the dynamic force range *5-10*.

The final design of the MR strut for the VIS of the launch vehicle preceded the design, manufacture and testing of the experimental strut. The parameters of the experimental strut were measured and consequently used for the verification of models used in the thesis. Knowledge obtained during the tests were used in the final design of the strut. One of the most important detections was that the ferrite (material used in the magnetic circuit) cracked during the semi-active control of the experimental strut. Therefore, a method of the fast magnetic circuit designing was established and subsequently patented. The method is based on a shape modification of the magnetic circuit which ensures shorter time response and the magnetic circuit is manufactured by 3D printing. The MR strut designed in this thesis has a predicted time response of *1.2 ms* and dynamic range *10*. The method which was used for the design process is summarised in conclusions.

KEYWORDS

vibration isolation system, launch vehicle, payload adapter, magnetorheological, damper, strut, valve, vibrations, suspension, damping, isolation, elastically connected damper, short time response, pressure thrust stiffness, metal bellows

ABSTRAKT

Práce se zabývá návrhem magnetoreologické (MR) vzpěry vibroizolačního systému (VIS) pro kosmický nosič. V rešeršní části jsou popsány vybrané VIS a vzpěry těchto systémů, které byly v kosmických nosičích využity v minulosti. Každá z těchto vzpěr obsahující kapalinu byla těsněna pomocí statických těsnění a pružných vlnovců vyrobených z oceli. Důkladněji byla analyzována vzpěra pasivního systému VIS s označením ELVIS, jehož konstrukce se stala inspirací pro tuto práci. Jedná se o tříparametrický systém, v němž je tlumič uložen na pružině, jejíž tuhost přibližně odpovídá objemové tuhosti vlnovců respektive jejímu průmětu do axiálního směru (pressure thrust stiffness).

V práci je představena metodika pro stanovení “pressure thrust stiffness” na základě geometrie vlnovce a také uvedeny parametry vlnovce díky kterým je možné měnit poměr mezi axiální a “pressure thrust stiffness” vlnovce. Tento poměr ovlivňuje v dané koncepci vzpěry její dynamické chování a tím i chování celého VIS.

Pro predikci dynamického chování vzpěry byl vytvořen multi-body model VIS založeného na Stewartově plošině a detailnější model jediné vzpěry. Simulace provedené v tomto modelu odhalily parametry, které mají vliv na výkonost tlumiče ve VIS: časová odezva a dynamický rozsah. Díky modelu byl určen rozsah těchto parametrů, ve kterých bude zaručena efektivní funkce vzpěry ve VIS, konkrétně: časová odezva: 0-5ms, dynamický rozsah: 5-10.

Před finálním návrhem vzpěry byla sestrojena vzpěra experimentální vzpěra, jejíž parametry byly přesně naměřeny a využity pro verifikaci jednotlivých modelů. Poznatky získané během experimentů byly využity při návrhu finální vzpěry. Jeden z nejdůležitějších poznatků byla nutnost náhrady feritového magnetického obvodu s ohledem na jeho křehkost. Proto byl odvozen tvarový přístup k navrhování rychlých magnetických obvodů z oceli s využitím 3D tisku, který byl následně patentován. Navržená vzpěra obsahuje magnetoreologický ventil jehož odezva je predikována na 1.2 ms a dynamický rozsah 10. V závěru práce je představena metodika, díky které byla vzpěra navržena.

KLÍČOVÁ SLOVA

vibroizolační systém, kosmický nosič, magnetoreologický, tlumič, vzpěra, ventil, vibrace, odpružení, tlumení, isolace, pružně uložený tlumič, krátká časová odezva, objemová tuhost

CONTENT

1 INTRODUCTION

Spacecraft is one of the most sophisticated things in of these days. It is used for communication, navigation, research etc. Currently used spacecrafts have made significant progress in comparison with the first one - Sputnik (launch in 1957), unlike launch vehicles. Especially the principle of the launch vehicle traction stays almost the same for more than 50 years.

The vibration environment is much harder than the on-orbit vibration environment. Although the spacecraft spends most of the lifetime on orbit, its components are dimensioned for the flight vibration environment, which takes only around 5 minutes. This approach leads to the high weight of the spacecraft components thus high mission costs, because transport of 1 kg to low orbit cost from 4 000 – 40 000 USD, depends on the total weight of the payload [1].

Vibration isolation system usually made of aluminium or composite is inserted between the sensitive payload (spacecraft) and the booster which is the main source of the vibrations. However, sometimes reduce the vibration transmissibility is a priority. This happened, for example, in the transport of the Hubble Telescope [2]. Thus, the vibration isolation system used in this mission was more efficient, but also heavier compared to other flights.

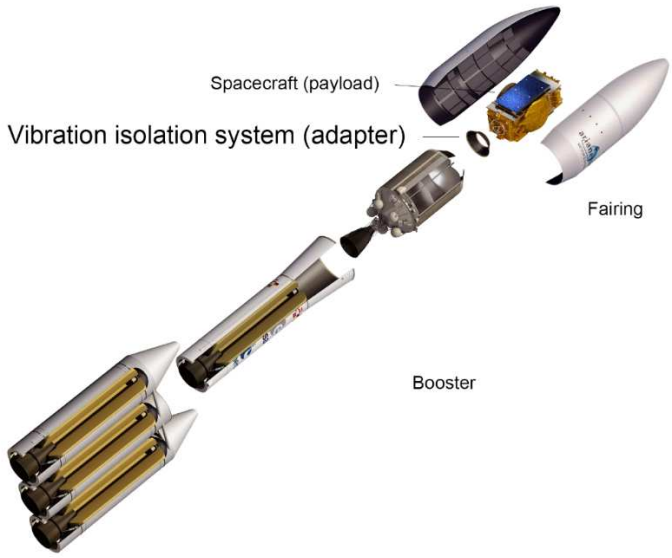

Fig. 1 Concept of the launch vehicle Ariane 6 (ESA) [3]

Even more payload comfort can be achieved by active vibration elimination. However, the weight of active vibration isolation system designed for spacecraft Artemis was approximately 5 times higher than the passive adapter intended for the same flight [4]. The weight increase was caused especially by the power supply and other electrical equipment.

A perfect vibration isolation system would be lightweight and very effective. This thesis examines the possibility of using semi-active vibration isolation system based on magnetorheological damper which efficiency is much higher than passive dampers. The power consumption of such as damper is in watts, so it could not increase the weight of the vibration isolation system significantly.

2 STATE OF THE ART

2.1 Vibration elimination – theory

Vibrations - an accompanying feature of movement - are generally undesirable. There are several ways of how to reduce them. Commonly used springs accumulate the vibration energy. However, the energy accumulation results in oscillation of a sprung mass on theoretically infinitely high amplitude at natural frequency:

$$f_n = \frac{1}{2 \cdot \pi} \cdot \sqrt{\frac{k}{m}} \tag{1}$$

Where: k is the spring stiffness
m is sprung mass

The infinitely high amplitude of oscillation devastates the system. For that reason, the spring is usually connected with the damper in parallel. The damper transfers the energy accumulates in spring to heat – dissipation. The damped system has a resonance frequency:

$$f_r = \frac{1}{2 \cdot \pi} \cdot \sqrt{(2 \cdot \pi \cdot f_n)^2 - \xi^2} \tag{2}$$

Where: ξ is the damping ratio, which can be determined as a fraction of real damping c and critical damping c_c:

$$\xi = \frac{c}{c_c} = \frac{c}{2 \cdot \sqrt{k \cdot m}} \tag{3}$$

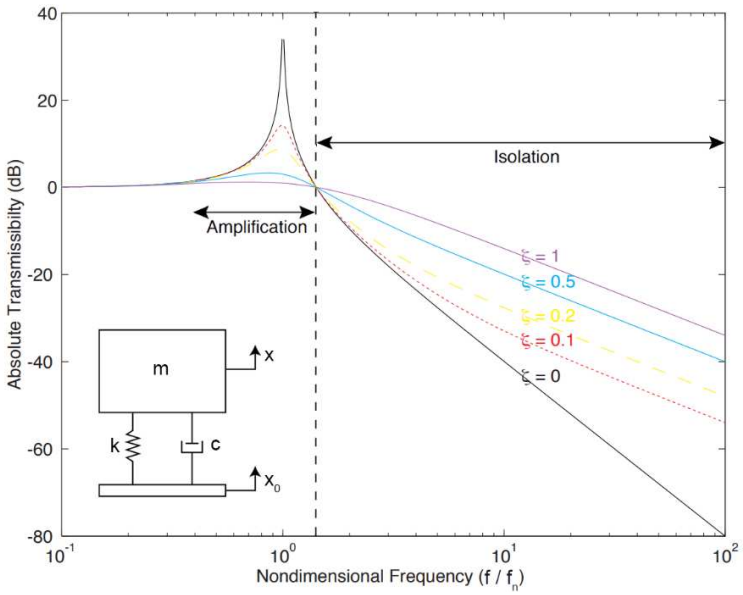

Fig. 2 Absolute transmissibility of 1 DOF system [5]

The damping ratio affects the transmissibility of the system which is usually illustrated by a transfer function. Transmissibility of 1 DOF system is shown in Fig. 2. This system consists of two passive elements connected in parallel – spring and damper. The increase of damping ratio causes a decrease in transmissibility (x/x_0) in the amplification area (vicinity of resonance). On the contrary, the damping ratio increase causes an increase of transmissibility in the isolation area [5].

Proposal of a damping ratio which for a specific system suitable is always a trade-off between maximum transmissibility in the vicinity of resonance and slope of decline of the transfer function in the isolation area.

However, transmissibility decrease can be achieved by elastically connected damper [6]. The damper is connected with a spring with stiffness k_1 in series. Honeywell Company called this disposition a three-parameter system [7, 8]. This system allows a significant decrease of transmissibility in the isolation area, while the transfer in the vicinity of resonance is not substantially increased. It can be achieved by suitable selection of ratio between primary and secondary stiffness $N = k_1/k$, see Fig. 3.

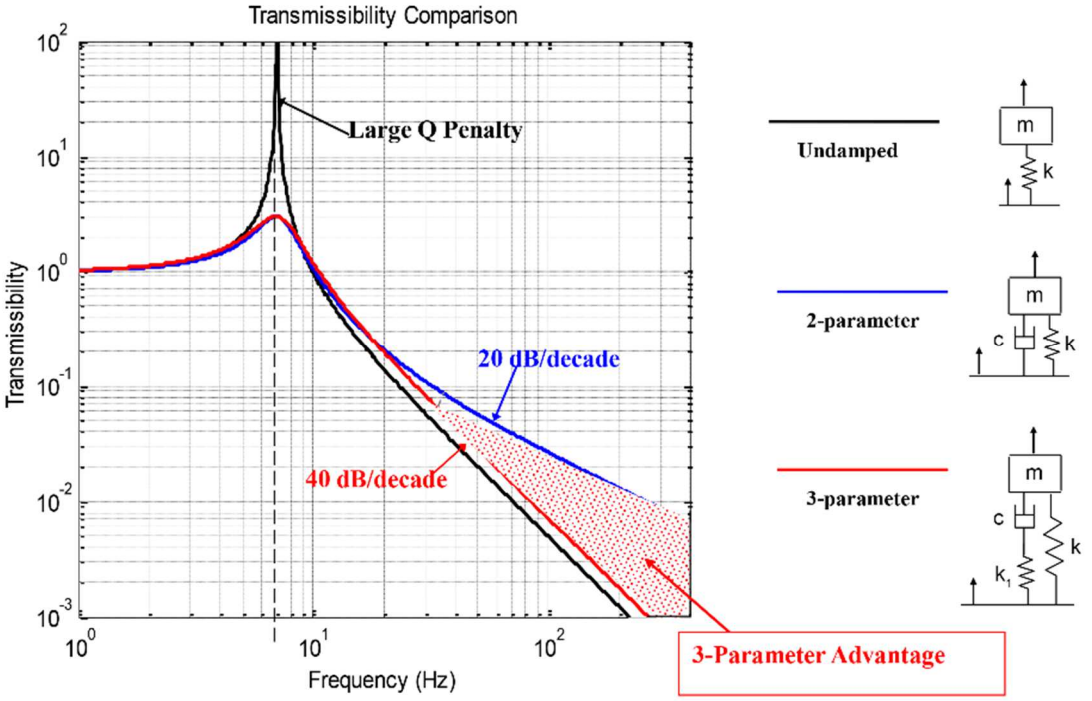

Fig. 3 Transmissibility comparison of 1, 2 and 3 parametric system [7]

Relatively high ratio N may cause an increase of resonance frequency and also the transmissibility increase at this frequency, Fig. 5. This effect occurs in case of high velocity and small stroke of the damper piston when the damping force is higher than the force necessary to compression of spring with stiffness k_1. The sprung mass oscillates on two springs which total stiffness is the sum of $k + k_1$. In extreme, this effect results in dangerous undamped oscillation, in the case of many times higher damping force than the force of spring k_1.

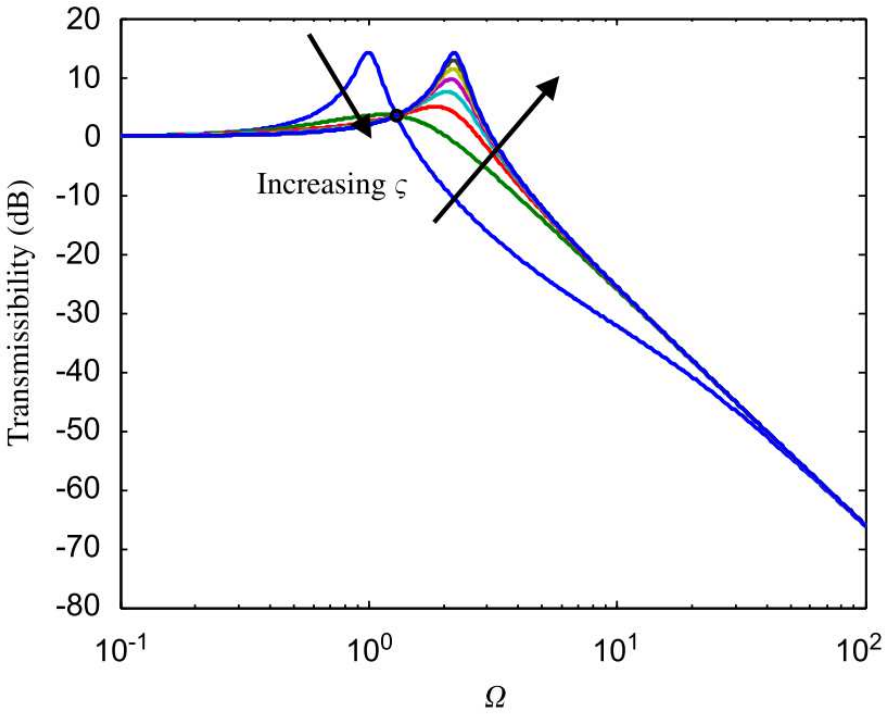

Fig. 4 Transmissibility of the 3-parameter system [9]

In addition of elastically connected damper, there is one more sophisticated method of vibration transfer decrease. Namely, by using a damper which damping can be re-adjusted, 1 DOF system with this damper is shown in Fig. 5 a).

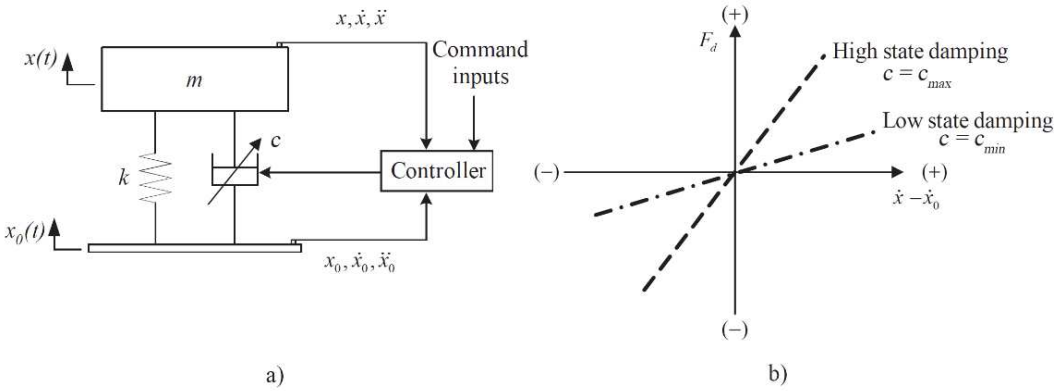

Fig. 5 1 DOF system with controlled damper a) and the force-velocity dependency of the damper [10]

In the case that the damper exhibits just two different force-velocity dependencies, see Fig. 5 b) it is advantageous to keep high damping in the vicinity of resonance and low (ideally none) damping in isolation area. This simple algorithm is called **adaptive-passive control** [10]. Mathematically it is described by this system of equations:

$$\begin{aligned} RMS(\ddot{x}) \geq RMS(\ddot{x}_0) &\rightarrow c = c_{max} \\ RMS(\ddot{x}) < RMS(\ddot{x}_0) &\rightarrow c = c_{min} \end{aligned} \tag{4}$$

The application of this algorithm is especially for the harmonic signal of excitation [10]. The switch between high and low damping is happening when the excitation frequency overcomes the border between amplification (transmissibility >1) and isolation area (transmissibility <1). This border is marked by a dashed line in Fig. 2.

Semi-active algorithms switch the damping even several times during a single oscillation period. There is a lot of semi-active algorithms for various purposes and various applications. However, only one of them: ON/OFF Skyhook will be described for the purpose of this thesis. The ON/OFF skyhook was developed for the transmissibility minimizing. When the sprung mass (payload) is deflected from the equilibrium position and excitation body (launch vehicle) moves in the direction which would mean even greater deflection of the payload, the damping force is minimal. Conversely, if the excitation body forces the sprung mass to move back to the equilibrium position, the damping is maximal. Mathematically it is described by:

$$\begin{aligned} \dot{x} \cdot (\dot{x} - \dot{x}_0) \geq 0 \ &\rightarrow c = c_{max} \\ \dot{x} \cdot (\dot{x} - \dot{x}_0) < 0 \ &\rightarrow c = c_{min} \end{aligned} \tag{5}$$

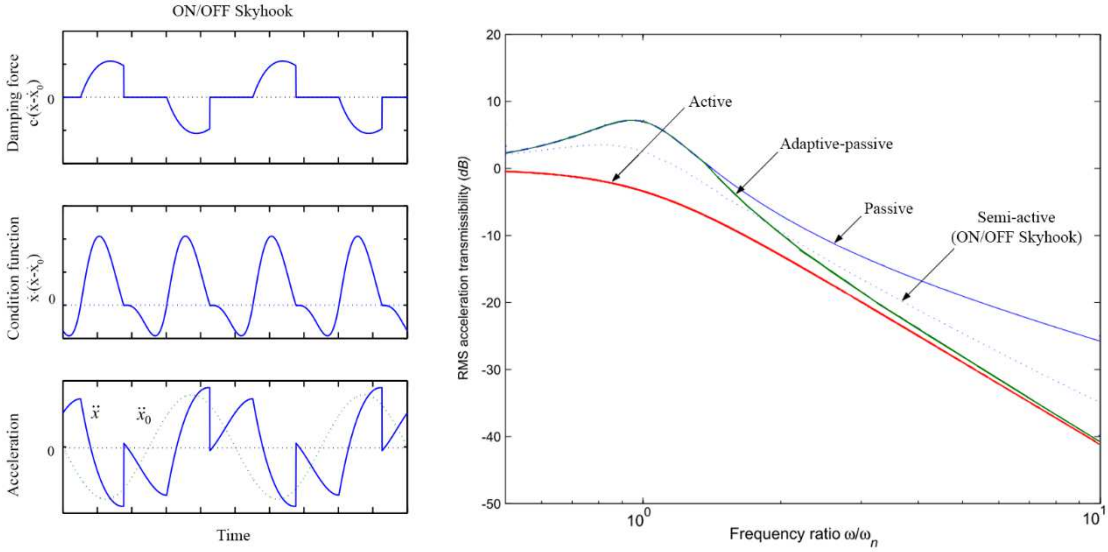

Fig. 6 Steady state response of on-off skyhook semi-active control at $\omega/\omega_n = 1$ (a), transmissibility comparison (b) [10]

The results of ON/OFF Skyhook shows a significant decrease of vibration transmissibility in the vicinity of resonance (dashed curve in Fig. 6) in comparison of the passive damper (blue curve). Even higher efficiency can be achieved by **Active** vibration isolation system [11]. The active vibration elimination is based on the forced movement of the sprung mass in opposite direction to the excitation. However, this method is huge energy consuming therefore, it was used especially pro light sprung masses [12].

2.2 Vibration isolation systems for the space application

Vibration isolation systems (VIS) are used in launch vehicle to decrease of vibration transmissibility between excitation body (launch vehicle) and sprung mass (payload). Acceleration bellow (blue signal in Fig. 7) and above (yellow signal) the VIS was measured during the launch vehicle Taurus (NASA) flight [13]. Vibrations and shocks are most often formed by booster oscillation, fairing separation of by lift-off blastwave. The payload must resist (to stay undamaged) in this vibration environment.

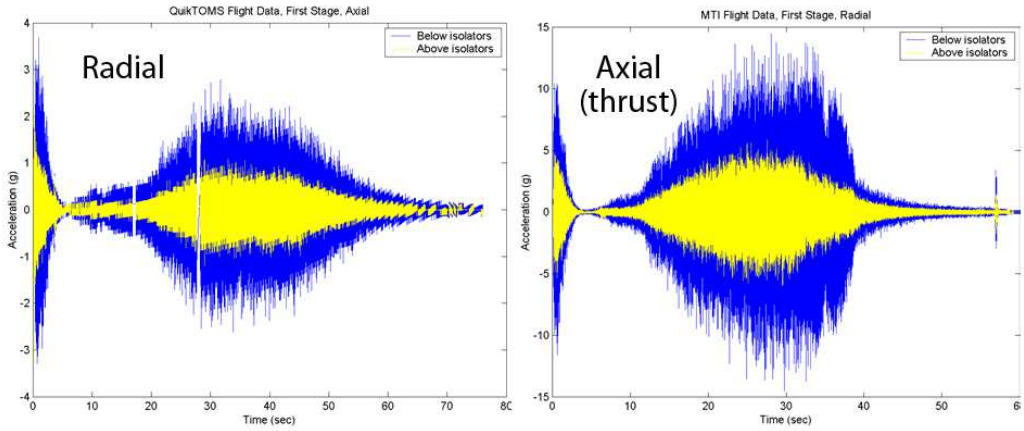

Fig. 7 Taurus/GFO flight data, bellow and above isolators [13]

VIS can be divided by application to whole spacecraft VIS or satellite part VIS (antennas, optical equipment etc.). The main difference between these two groups is their lifetime. Whole spacecraft vibration isolation is necessary only during the flight – separating of the satellite (payload) from the launch vehicle happens approximately 5 minutes after the start. On the other hand, the satellites VIS has to ensure On-orbit vibration isolation which usually takes several years.

2.2.1 Structural vibration isolation systems

Usually passive systems which isolate the vibrations by the suitably designed shape of their structure. The SoftRide products belong to this group, see Fig. 8. The Uniflex (left) and the Omniflex (middle) systems were developed to isolate frequency lower than *80 Hz*. Higher frequencies can be isolated for example by ShockRing which reduces vibration most effectively around *1 kHz* [14].

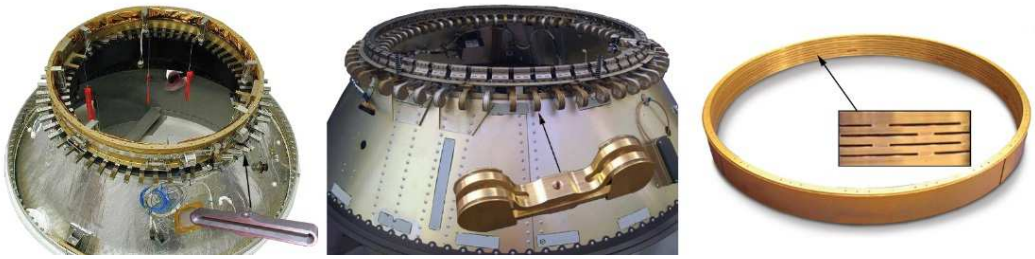

Fig. 8 SoftRide products from the left: Uniflex, Omniflex, ShockRing [14]

A disadvantage of the structural systems is that the frequency range of their effective using can be changed only by redesigning. Moreover, internal damping of structural systems material is not high; therefore, the transmissibility of these systems is relatively high in the vicinity of resonance.

An interesting structural system is a composite lattice conical shell, which is composed of the helical and circumferential hoop (ribs) made of a composite material called unidirectional carbon-fibre-reinforced plastic (CFRP).

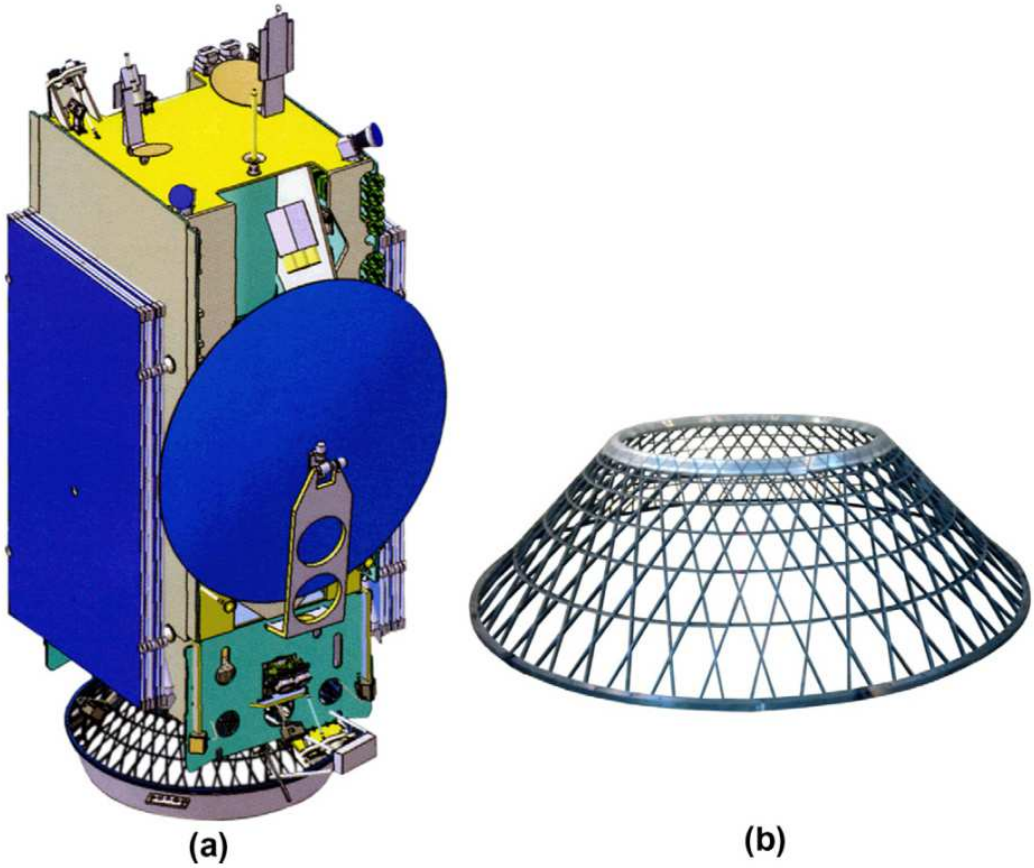

Fig. 9 Anisogrid composite conical payload adapter. [15]

Morozov optimized the ribs parameter with regard to weight and load capacity of VIS (adapter). Buckling stability of each rib was a limiting factor of the parameters determination. Total load capacity of the adapter was $P_{cr} = 100\ kN$. Mass of the adapter with conical shape was *3.2 kg* and diameters *800*, *1600 mm* respectively. High of the cone was *600 mm*. However, Morozov's study is primarily focused on the load capacity of the adapter thus, the vibration isolation properties of the cone were not determined.

Payload adapters used by ESA

Cone made of composite material is the most common element for launch vehicle payload vibration protection. This structural VIS are sometimes called payload adapter.

The adapter diameters are normalized. The lower (base) diameter corresponds to the connection with the launch vehicle, diameter 2624 mm is used in Ariane 5, *1920 mm* in Vega, *2000 mm* in Soyuz *2000 mm*, etc. The upper diameter depends on the payload

which is used. Launch vehicles user manuals defined these upper (payload) diameters: *937, 1194, 1663, 1666* a *2624 mm* [16, 18].
However, not just the dimensions have to be kept, another important parameter is the natural frequency of the system consist of payload and adapter. The payload modal shapes may disturb the flight control (sampling frequency is usually 50 Hz). Therefore, there is a request to keep the natural frequency of the system within the range *20 – 45 Hz* in the longitudinal direction. The natural frequency in lateral direction has to be higher than *7.5 Hz*, this value is relevant for a payload mass *6 500 kg*. Thy system with a payload lighter than *2 500 kg* has to have a frequency higher than 15 *Hz*.

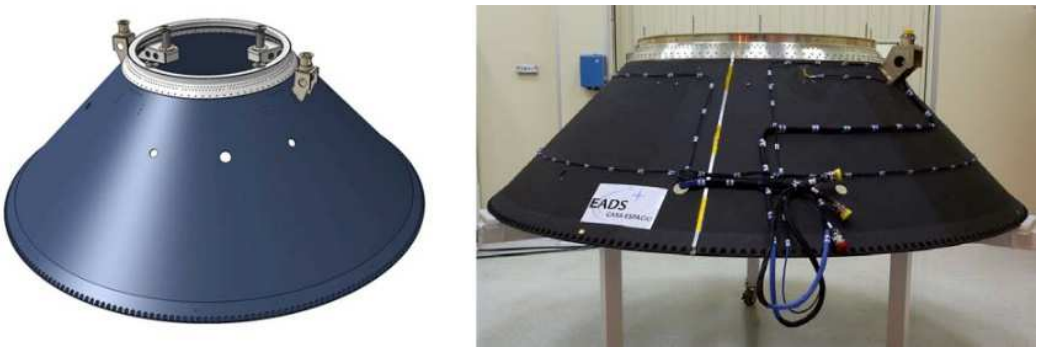

Fig. 10 ESA adapters: PAS 937C (left) [16] a PAS 1194C (right) [19]

There are two most commonly used adapters in Fig. 10. The payload adapter PAS 937 covered 15% PAS 1194 even 65% of ESA missions [19].
The payload (satellite) has to be separated from the launch vehicle at the end of the mission. Therefore, the adapters have a specially shaped flanges Fig. 11 which are used for connecting by ring including a pyrotechnic patron.

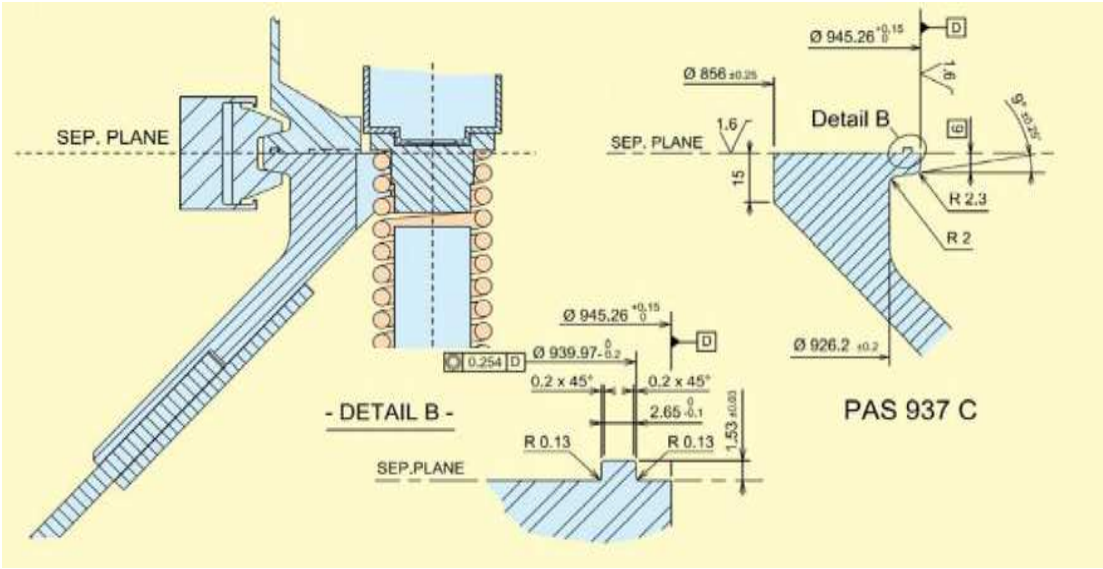

Fig. 11 Connection dimensions of adapter PAS 937C [18]

Composite cones are designed to eliminate vibration at low frequency. Additionally, another system can be used to improve the vibration isolation at high frequency, for example, system SASSA effectively decreases vibrations higher than *100 Hz*. This

system is consisted of two connection parts by groove, tongue and deformation element, usually made of elastomer. The simulation predicted the mechanical behaviour of the elastomer was preceded the development [20].

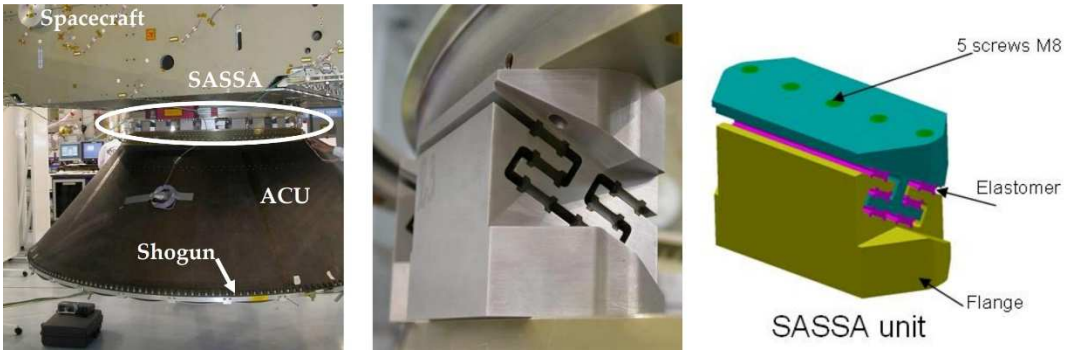

Fig. 12 SASSA [20]

2.2.2 Mechanical vibration isolation systems

Vibration energy spreads in all directions, therefore the Stewart platform (6 DOF mechanisms) is used almost exclusively [7, 21, 22]. The Stewart platforms have various numbers of struts. But, at least 6 struts guarantee 6 DOF mechanisms. The strut may consist of spring and damper [7], actuator [23] or both [22]. With regards to what is the strut consists of, the Stewart platforms are divided into the two groups: **Passive**, the energy in the system is accumulated by spring and dissipated by damper; and **Active**, the payload is moved by actuators, thus the energy has to be supplied to the system [11].

Evolved Launch Vibration Isolation System (ELVIS)

Passive system ELVIS was tested with experimental payload, which had similar geometric parameters to parameters of commonly used satellite, see table 1. Experimental payload was consisting of shell body made of aluminium alloy and solid weight made of steel.

tab. 1 Experimental payload parameters

Parametr	Value	Unit
Payload mass	1 135	[kg]
Connection diameter	1 155	[mm]
Centre of gravity height	1 600	[mm]

Lateral excitation was provided by dynamometer with harmonic movement: with a constant amplitude of stroke *5 mm* up to frequency *10 Hz* and constant amplitude of acceleration *1* g for the frequencies higher than *10 Hz*. Accelerometers were connected to the payload at various position, their amplitude-frequency dependency is shown in Fig. 13.

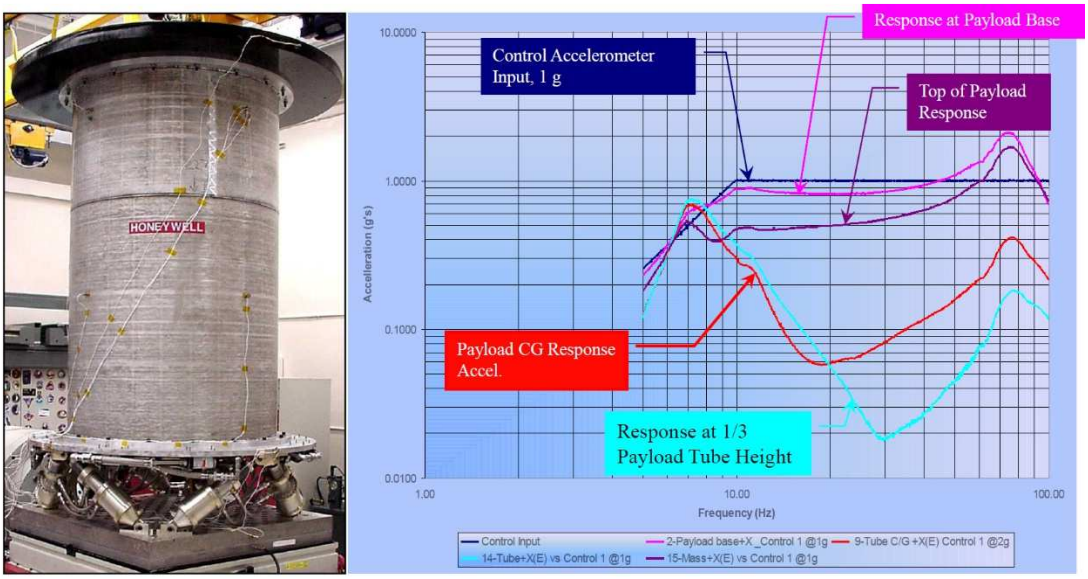

Fig. 13 ELVIS and acceleration measured in the lateral direction [7]

The acceleration signals revealed the presence of two modal shapes in range *5 – 100 Hz*. The payload behaviour can be estimated due to that the accelerometers were fixed in the various height of payload. The low-frequency acceleration peak (around *7 Hz*) has a similar shape along the whole payload height. Of which it can be concluded that the translation movement was dominant for this modal shape. On the other hand, transmissibility of high-frequency peak (around *70 Hz*) differs significantly along the payload height. This modal shape was probably similar to the rotation with the axis of rotation near the point with the lower transmissibility. This point is approximately in a third of height by measurement, see blue curve in Fig. 13.

A 6-DOF Passive Vibration Isolator Based on Stewart Structure with X-shaped Legs

The article deals with the possibility of using the X-shaped strut see Fig. 14 a) for lower transmissibility of Stewart platform in comparison with conventional passive strut b). The mechanism was analyzed in multi-body system ADAMS and manufactured subsequently, see Fig. 14 c).

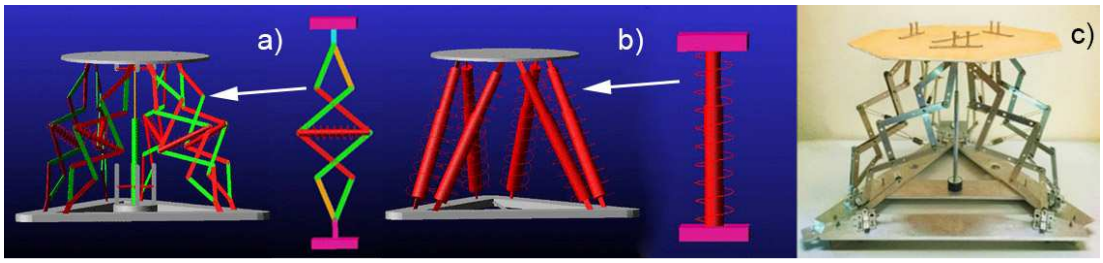

Fig. 14 Stewart platform with X-shaped legs [24]

Influence of chosen parameters of the system on the mechanism behaviour was examined. It was evaluated by transmissibility of vibrations from base to sprung mass. For the purpose of this work, only a few parameters are relevant and discussed: sprung mass *m*, and spring stiffness *K*. The excitation was provided by axial (vertical) movement of the base plate. The results obtained by simulation and experiment can be

compared problematically by non-compliance with the same sprung mass and high level of noise (measurement), see Fig. 15. The noise was created especially by the passive loses that means the friction in the X-shaped legs.

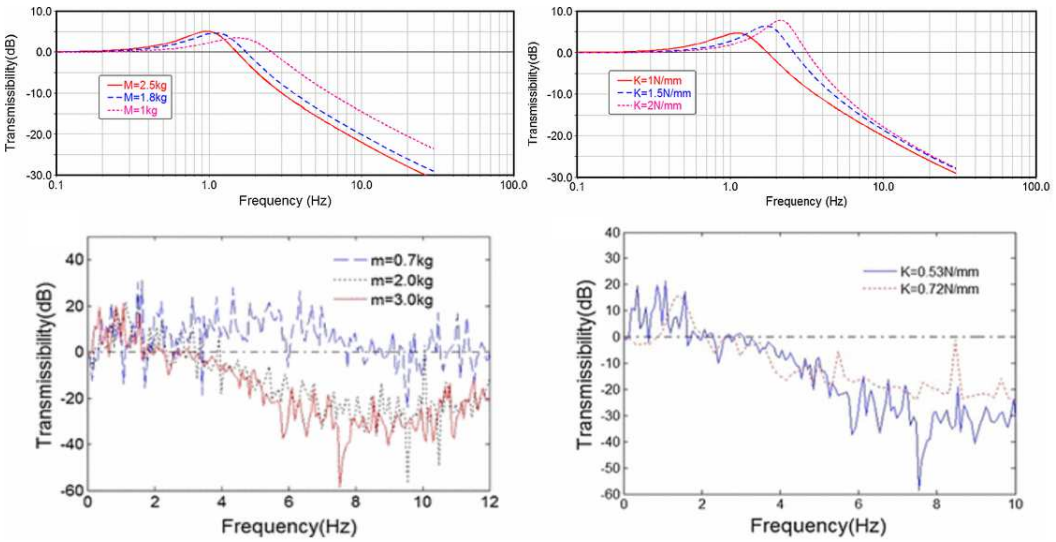

Fig. 15 Sprung mass dependency on the transmissibility (simulation vs. experiment) [24]

Experimental Study on On-orbit and Launch Environment Vibration Isolation Platform

Each of 6 strut of VIS mentioned in the study of Lee [22] consists of spring, damper and voice coil actuator, see Fig. 16 a). This is called a "Hybrid Isolation Device" and it is based on Cobb study [25]. Significant reduction of vibration transmissibility to the sprung mass can be achieved by control of the strut pulling off. Manufactured VIS, see Fig. 16 b) was developed for the vibration elimination on orbit, which affected the testing methodology.

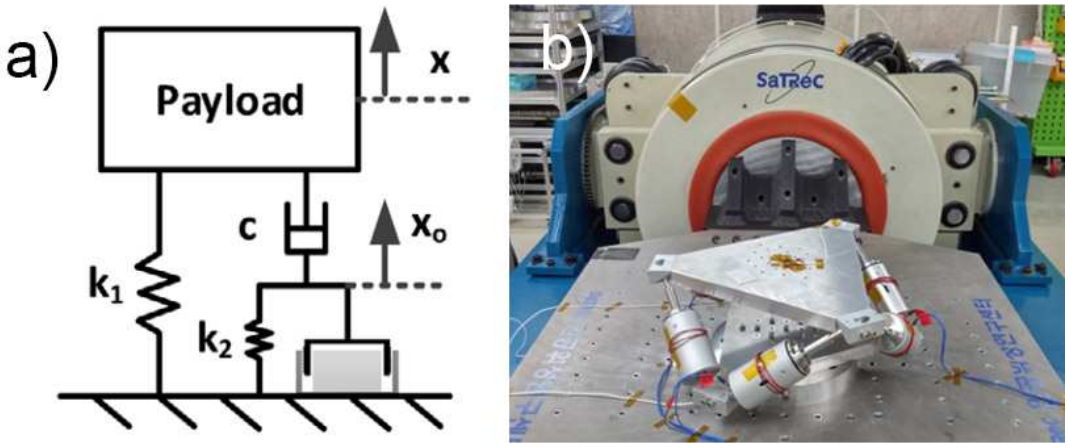

Fig. 16 Hybrid isolation device b) and its simplified scheme a) [22]

The acceleration of base (excitation) and sprung mass (response) was measured in specific conditions, which were similar to the on-orbit environment. That means the

pressure lower than atmospheric, in the case of experiment *1.3 Pa* and the temperature range from *-10°C* to *50°C*.

The result shown that the transmissibility is significantly influenced by the ambient pressure, see Fig. 17 a). This is caused by the strut concept (described in chap. 2.3.2) which is based on metal bellows. The stiffness of the bellows is dependent on the ambient pressure. Perhaps, lower ambient pressure caused deformation of the bellows, which result in a decrease of the bellows stiffness, thus a decrease of natural frequency, but paradoxically increase of the transmissibility maximum.

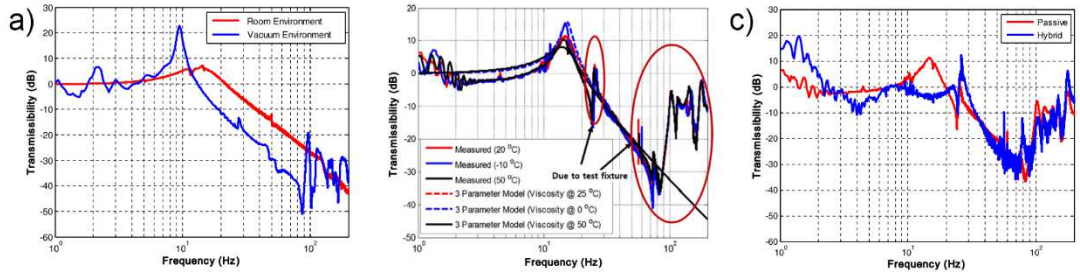

Fig. 17 Tests results of Hybrid VIS [22]

Temperature affects the viscosity of the damping medium – silicon oil, which affect transmissibility near natural frequency slightly, see Fig. 17 b). Active control suppresses the resonance peak completely, see Fig. 17 c).

The contribution of this article is a study of the VIS behaviour in conditions similar to the on-orbit environment. The fact, that the ambient pressure influenced the bellows stiffness does not correspond to a study of Thakkar (in chap. 2.4.1), which determined the stiffness of formed metal bellows as linear for a wide range of deformation. The explanation may be that Lee uses welded bellows for the strut for VIS while, Thakkar used formed bellows.

Another surprising result deals with temperature influence on the damping. The higher the temperature the lower the viscosity of the silicone oil [26]. The lower the viscosity of damping oil is the lower the damping a viscous damper exhibits. The higher the damping the damper has the lower the transmissibility of the system is. But in this case, the lower temperature causes the higher transmissibility. However, in the case of elastically connected damper does not apply in general that the higher the attenuation, the lower the [6, 9], see chap. 2.1.

Voice Coil Motor (VCM)-Based Stewart Platform used for Active Vibration Isolation

An active system was developed for positioning and vibration isolation of precise devices placed in the satellite – cameras, telescopes, interferometers, laser communicators etc. [23]. The mechanism consists of 6 struts, each of strut can change its length in range $\pm 5\ mm$ due to voice coil actuators. The payload with maximum mass *4.85 kg* is located on the top plate.

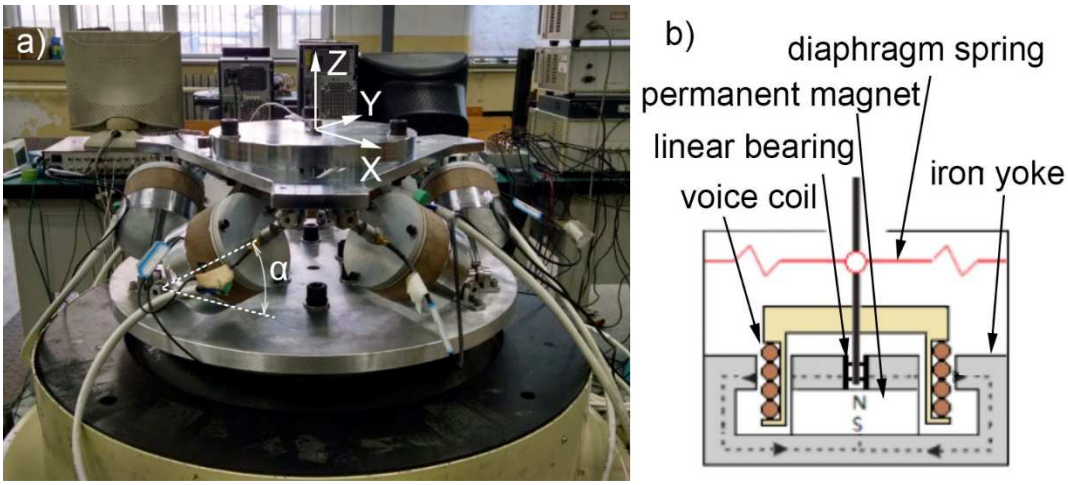

Fig. 18 An active VIS a) strut with a voice coil actuator b) [23]

Sharp angle α between strut and base plate, see Fig. 18 causes a relatively low load capacity of the platform. However, there was a requirement that the system should have similar natural frequencies in lateral (X, Y) and axial (Z) direction. Top plate vibrations were compared in two versions of vibration elimination. The first – passive was based on constant electrical current in the coil. Therefore, the strut worked similarly as coulomb damper. The acceleration measured with passive control of current in the coils is in Fig. 19 a). It can be compared with acceleration measured with active control of the struts, see Fig. 19 b). Length of each strut was controlled by an algorithm what results in lower acceleration compared with passive control. The difference is obvious, especially in lateral directions.

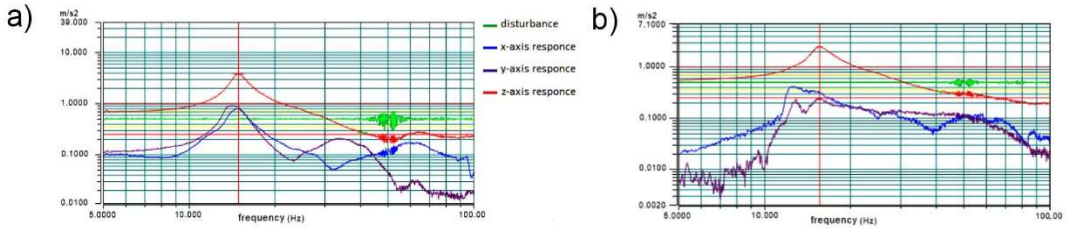

Fig. 19 payload acceleration in passive mode a) active mode of VIS b) [23]

There are two peaks in acceleration measured in the lateral direction (Y), it is caused by excitation of two natural shapes as well as in ELVIS measurements. The ratio between the low-frequency and high-frequency natural shape of VIS designed by Chi is significantly lower than the ratio of ELVIS despite that the payload used by Chi is apparently less prone to yawing than the payload used by Ruebsamen (ELVIS). However, ELVIS uses a fluid stabilizer which significantly increased the stiffens in lateral direction and allowed to design struts with lower carrying capacity.

2.2.3 Stabilizers

Stewart platform consists of several struts used for support of the whole spacecraft as the Honeywell tested (chap. 3.1.4), is extremely loaded because of the payload shape and commonly used connection diameters (chap. 2.2.1). It is clear to see in Fig. 20, which illustrated an ambitious plan of SpaceX company – to transport school bus

on the orbit of the Moon. A similar situation of payload shape is in VEGA launch vehicle by ESA in the right side of Fig. 20.

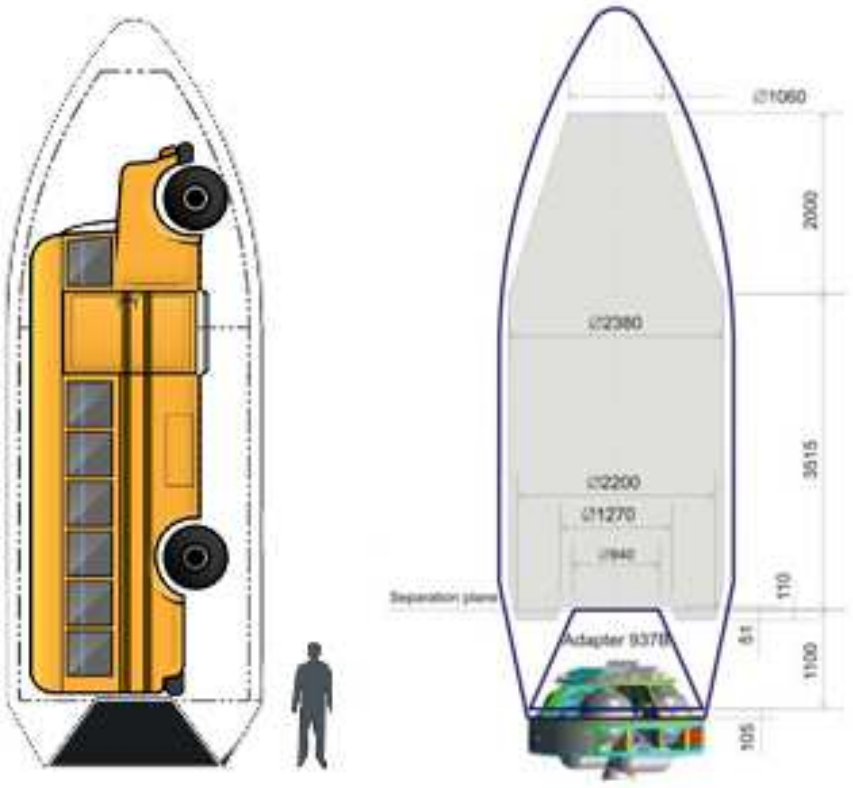

Fig. 20 Shape and dimensions of the launch vehicle payload [27, 16]

The payload geometry, especially its centre of gravity height causes an enormous bending load of the payload adapter. Moreover, there is a risk of the control distribution by the payload yawing, therefore the yawing should be minimized. But the natural frequency of vertical direction should be low. This two contradictory requirement is not possible to achieve by common VISs. Therefore, the ELVIS was equipped with the hydraulic stabilizer.

Many applications (automotive, railway etc.) use mechanical stabilizer, which transfers undesirable yawing to the torsion bar which works as a torsion spring.

The hydraulic stabilizer of ELVIS

Experiments showed that lack of mechanical VIS is that the strut affected lateral and axial parameters of the VIS simultaneously. Consequently, it is complicated to tune the system to similar natural frequencies in lateral and axial direction. This is the motivation which started a development of hydraulic stabilizer for ELVIS called “cross-link”; see Fig. 21. The cross-link increases the stiffness of VIS in the lateral direction while the axial stiffness remains the same.

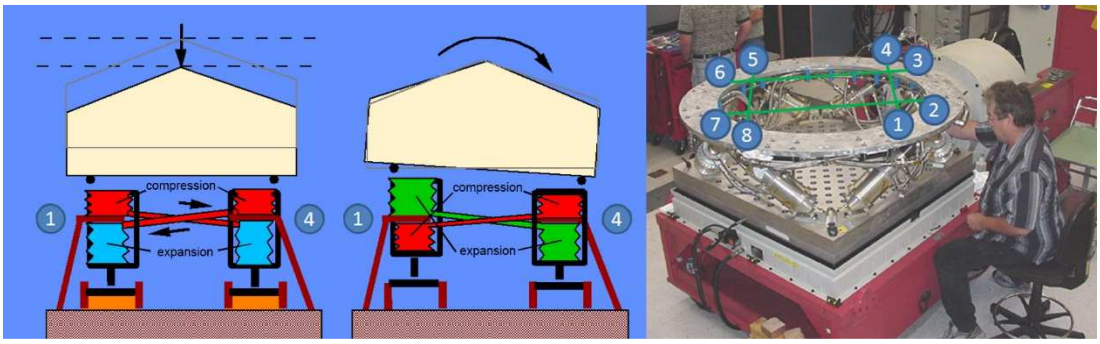

Fig. 21 The hydraulic stabilizer of ELVIS [7]

As the name suggests, stabilizer principle is based on cross-linked chambers of the struts. When the VIS is loaded by an axial force (left side of Fig. 21), the compression and the expansion exist in the chambers of each strut. It causes the fluid flow between the strut which is cross-linked. But when the bending moment is applied, there is a compression in both of connected chambers and the stabilizer becomes much stiffer, thus the yawing is minimized. The cross-link system was patented [28] and results in lateral direction seem to be very promising.

However, axial oscillation of payload is accompanied by fluid flow. There is an effort to minimize the volume of flowing volume because of mass and high stiffness of pipes, which result in small pipe diameters. But, pipe diameter reducing causes hydraulic loses that means damping, which is necessary to add to the strut damping. That means the stabilizer works as an additional damper for the axial direction.

The literature [29, 30] say that the reciprocal flow of a fluid in the flexible pipeline can be seen as a mass oscillation on a spring. The authors of the above-mentioned articles used the term “fluid mass effect“. The fluid mass oscillates even in the case of compression in both chambers which are cross-linked because of non-rigid pipes used for the link. It results in a resonance which increases the vibration transmissibility of the VIS.

Mechanical stabilizer

Mechanical stabilization is based on the torsion elasticity of a bar. Thus usually it is called a torsion bar. A rod and a lever transfer linear movement to the torsion of the bar, which is usually fixed in bearings. Mechanical stabilization is used in many applications, perhaps best known is the torsion stabilizer in a car, which using started Coleman’s patent in 1919 [31].

Torsion stiffness of the mechanical stabilizer is tuned by material and geometry of the torsion bar and also the length of levers where the rods are placed. Sometimes, a change of the stiffness is required; there are several methods to adjust suitable stiffness without replacing the torsion bar. Two of the methods were shown in Elephant racing stabilizers.

The first method uses various lengths of levers which can be changed step by step using several holes, see on the right side of Fig. 22 or smoothly by the groove, on the left of Fig. 22. The second method is based on the rotation of the lever which has a cross-section similar to the letter *I*. Maximum of the lever stiffness is when the force is applied along the longer side of the cross-section.

Fig. 22 Mechanical stabilizer [32]

Mechanical stabilization is one of the possible ways in space applications. However, the weight-stiffness balance is necessary to provide before the design. Moreover, the same stiffness in both lateral directions of VIS can be achieved only by at least two perpendicular torsion stabilizers.

2.3 Struts of VIS for space application

The strut of mechanical VIS combines a function of spring and damper. The spring accumulates the vibration energy and it is necessary to payload support. The damper dissipates the kinetic energy of the vibration and it is necessary to decrease of vibration amplitude in the vicinity of resonance.

2.3.1 The D-strut

Dual strut (D-strut) is patented [33], presented in the article [29] and referred to as three-parametric system. This term is based on the fact that the strut consists of three elements which can produce a force: **primary spring**, which is connected with the **damper** in parallel. The damper is connected with **secondary spring** in series. The advantage of this disposition is mentioned in chap. 2.1. From the perspective of the designer, three-parametric disposition can be achieved by filling the damping fluid into the elastic case. Davis (author of D-strut) used a metal bellows as the case.

D-strut consists of two pairs of metal bellows – primary and secondary. A fluid can flow between them by annulus between the shaft and the piston, see Fig. 23. The strut is attached by flexible joint (blade) and flange. Stiffness k of the primary bellows prevents relative movement between the blade and the flange. The axial deformation of the bellows causes a change of the internal volume, which causes an increase in pressure on one side of the piston and decrease in pressure on the other side, thus the fluid start to flow. However, the flow is not the only one consequence of the pressure unbalance; the other result is an axial deformation of the secondary bellows with stiffness k_1. Therefore, the damper in this strut can be considered as elastically connected by Harris [6] and three-parametric by Davis [29]. The ratio between the secondary and the primary stiffness $N = k1/k$ influences the vibration transmissibility of the strut [6].

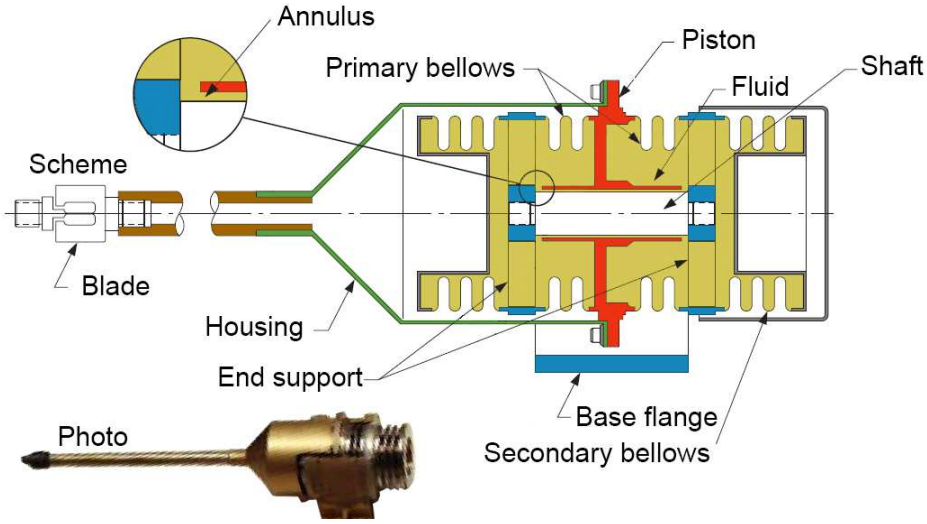

Fig. 23 Scheme and photo of D-strut [29]

The elastically connected damper is well known and usually realized by silent blocks in eyes of the damper. However, this simple and cheap solution can't be used in strut because connection parts attached damper and also the spring of the strut. The elastic connection has to be realized inside the strut for example by elastic bellows.

The bellows application, in addition, solves the volume changes caused by temperature, therefore there is not necessary to use an expansion tank or a flow piston. The struts with the bellows were applied in many application, for example, magnetorheological damper described in chap. 3.5.4, strut in the Millennium Bridge in the London [34], and so on.

2.3.2 The Hybrid Strut of Lee et al.

Authors do not deny an inspiration in D-strut. The elasticity of the strut is realized by the axial stiffness of the bellows which is located between the payload side and middle flange, which is fixed; see Fig. 24. The damping is caused by fluid flow through an orifice in the flange, the fluid (oil) flows from bellows 1 to bellows 2 or back. An axial stiffness of bellows 2 causes that the damper is elastically connected. Two bellows serve to the vibration energy accumulation, passive damper dissipates the energy. Moreover, there is a voice coil actuator which can be controlled by an algorithm. Combination of passive and active elements causes that the strut is hybrid.

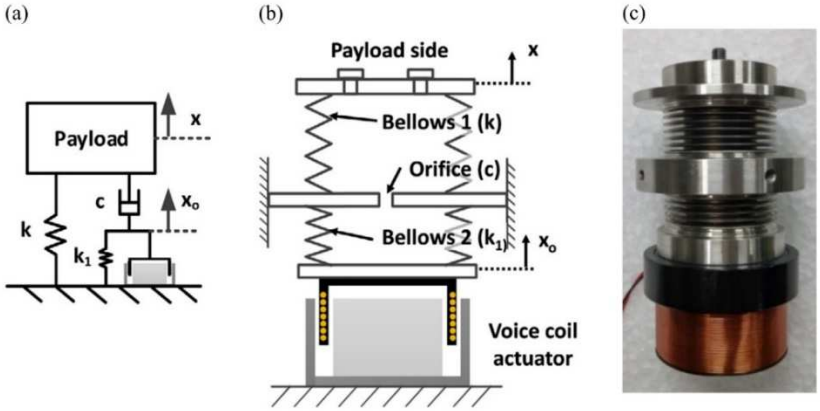

Fig. 24 Hybrid strut [22]

2.3.3 The strut of the ELVIS

This strut is also inspired by the D-strut, the main difference is that strut of ELVIS uses just one pair of bellows with the same stiffness in instead of two pairs in D –strut with primary and secondary stiffness. The fluid flows between the bellows due to the hole in the piston rod. The pressure in the fluid cannot stretch the secondary bellows. Nevertheless, this concept is also called three-parametric, because the pressure causes "inflating" of bellows.

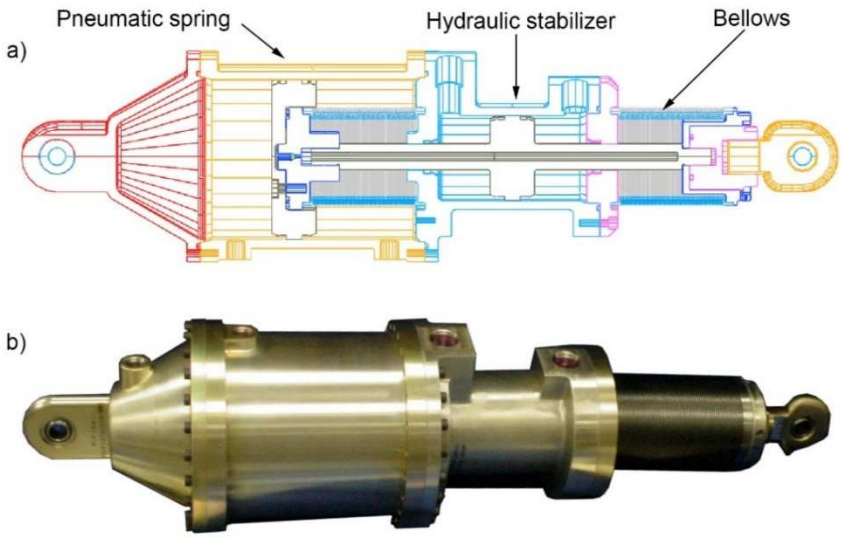

Fig. 25 Scheme a) and photo b) of ELVIS strut [7]

Davis defines the resistance against this deformation as volumetric stiffness [29]. However, this stiffness is marginal in his conception with respect to the difference in orders between the volumetric stiffness and axial stiffness of the secondary bellow. The volumetric stiffness cannot be neglected in the strut of ELVIS. The value of volumetric stiffness is the key parameter to the stiffness determination of the damper elastic connection, marked as k_1, in Fig. 3.

Stiffness k in the scheme is formed by the axial stiffness of primary bellows and a stiffness of pneumatic spring. The pressure in chambers of the pneumatic spring is equal under the static load of the strut [7]. The difference between the effective area above and below the piston of pneumatic spring multiplied by the pressure inside the chambers defines the static load of the strut. The various pressure in the spring allows using this strut for various sprung mass with the same compression of the strut. The bellows are not preloaded in this position.

The piston rod extension used as a piston of stabilizer is located in the cylinder between the bellows. This piston separates the chambers of hydraulic stabilizer mentioned in chap. 2.2.3.

The strut of ELVIS is innovative in the solution of elastically connected damper. The disadvantage of this concept is that the volumetric stiffness is not listed in datasheets of bellows. Therefore, the chose of the bellows for this application is complicated. Without known, the volumetric stiffness cannot be guaranteed the strut functionality. Therefore, next chapter will be focused on the elastic metal bellows and determination of its parameters.

2.4 Metal bellows

2.4

Metal bellows are commonly used for thermal expansion in pipelines – loaded by axial force; for a component of the clutch – loaded by torsion, or for pressure accumulators – loaded by internal pressure. However, the bellows can be used as the case of damping fluid.

A leakage of a fluid has destructive effects on electronics of spacecraft (payload). Damper with conventionally sealing placed between the piston rod and body of the damper is prone to leaks because the sealing is between parts whit relative movement. Dynamic sealing of piston rod can be replaced by static sealing of flexible bellows. The leakage risk of static sealing is much lower than the risk of a dynamic one. Moreover, the static type of sealing has no friction, which brings benefits in the dynamic behaviour of the semi-actively damped system.

The metal bellows are made by two technologies: forming or welding; see Fig. 26. Formed bellows are especially used for pipelines compensators because this bellows allows high axial deformation and high maximum internal pressure. On the other hand, welded bellows have very low axial stiffness; therefore, the most common application is mechanical sealing in vacuum pumps or in the petrochemical industry [36].

Fig. 26 Formed and welded bellows [35]

The volume change, which is caused by piston movement in conventional damper can be substituted by two sealed bellows which are connected above and under the piston a connected together by an orifice in the piston. Axial stiffness of bellows is much lower than a resistance against the volume change caused by internal pressure. The volume change is accompanied by the length change in axial direction. It is caused by force which is called pressure thrust [42]. So, the projection of volumetric stiffness to the axial direction is in this thesis called **pressure thrust stiffness**. Axial stiffness commonly available in product lists, while the pressure thrust stiffness is not available there. Final Element Analysis (FEA) is one of a possible approach to determining the pressure thrust stiffness using the bellows dimensions and parameters.

2.4.1 FEA of metal bellows

2.4.1

Above mentioned shell parts were simulated by many authors [36 - 40[40]. The FEA used two general approaches:

3D model meshed by “SHELL“ elements [40]
2D model with axial symmetry meshed by “SOLID“ elements [38]

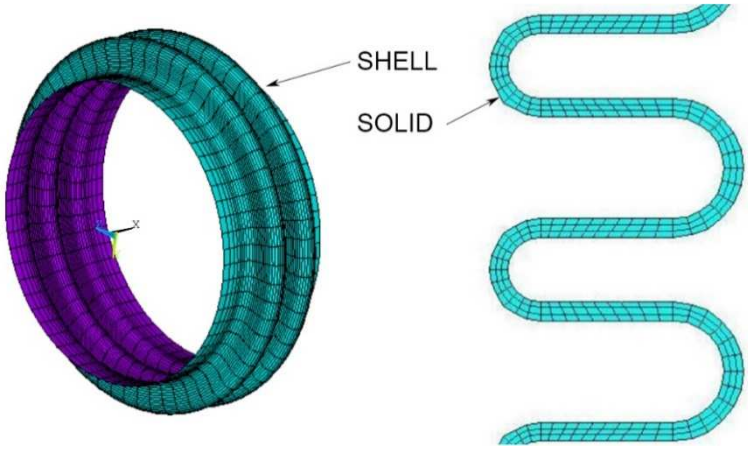

Fig. 27 3D shell and 2D solid model of metal bellows [41]

Thakkar compared both methods in his dissertation thesis [41], the difference between these approaches is shown in Fig. 27 and the result of circumferential and longitudinal stress is in Fig. 28. Moreover, the results are compared with the analytical counting. The stresses obtained by both approaches of FEAs are almost the same. In addition, consistent with the results obtained analytical, the deviation is approximately *20 %*.

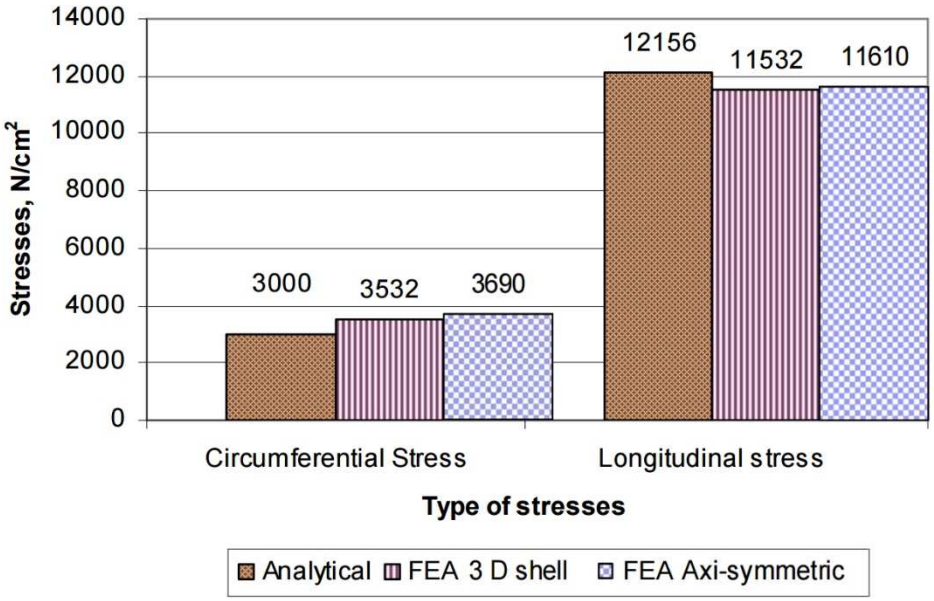

Fig. 28 Stress in metal bellows [41]

The analytical counting was in Thakkar's study compared with the measurement by axial stiffness and the deviation was acceptable. The axial stiffness was predicted constant (independent on the internal pressure). However, the measurement showed a slight deviation from this hypothesis, see Fig. 29. The deviation between measurement and simulation was determined of 18% after averaging of measured data.

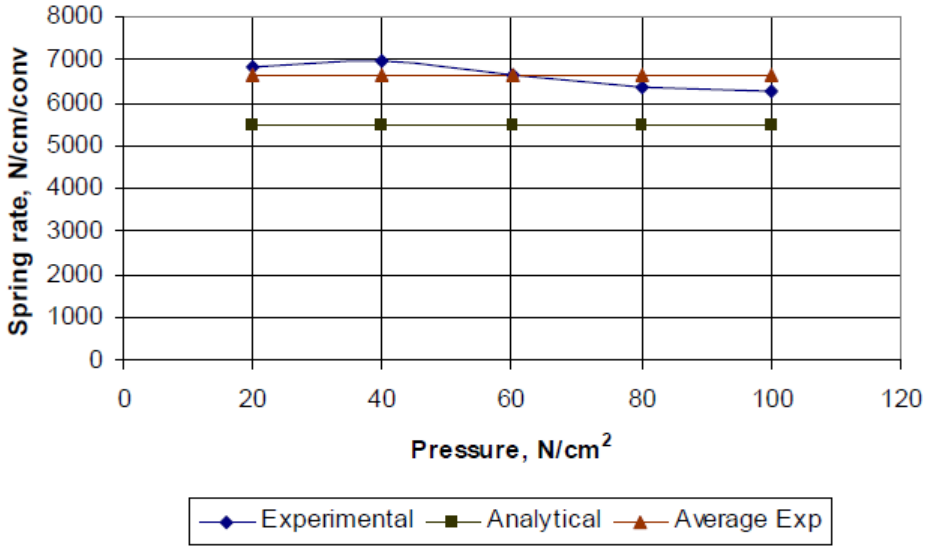

Fig. 29 Spring rate comparison [41]

Search in the literature did not reveal any FEA of metal bellows deals with the interaction between the filling of the bellows and the wall. However, there were some mentions that the internal pressure causes the length deformation of pipelines. It is caused by the pressure thrust force on the surface between the minimum and maximum diameter of bellows.

2.5 Magnetorheological dampers

In general, a damper dissipates vibration and shocks energy, which is previously transferred to oscillating by a spring. Internal friction of damping material converted the oscillation energy to heat each stroke of the damper. The damping material can be solid in coulomb dampers [43], oil in hydraulic dampers [29], or suspension of solid particles in a fluid used in magnetorheological (MR) dampers.

This smart material – MR fluid composed of ferromagnetic microparticles dispersed in a non-magnetic fluid in most cases oil [44]. Such a suspension can change its rheological properties especially the yield stress when the magnetic [46] or electric field [45] is applied, see Fig. 30. The yield stress is defined as a value of shear stress which has to be exceeding to start the flow of the fluid [47]; see Fig. 30.

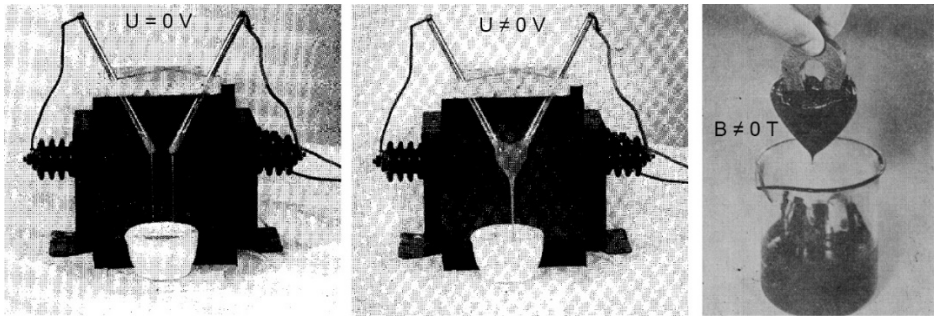

Fig. 30 MR fluid in electric [45] and magnetic [46] field

Research in this field was started in 1939 [45]. However, application of the MR effect occurred at the end of 20th century. The conventional design of MR damper

contains a gap in the piston, see Fig. 31. The magnetic field can be applied in the gap using an electromagnetic coil. The ferromagnetic particles of the MRF fluid are dispersed randomly and the damping in this state is not high. But, when the coil is powered by an electric current, magnetic flux density in the gap increase, the particles are formed into a chain-like structure, the yield stress of the fluid increase and the damping force in this state is significantly higher than the force of the inactivated state.

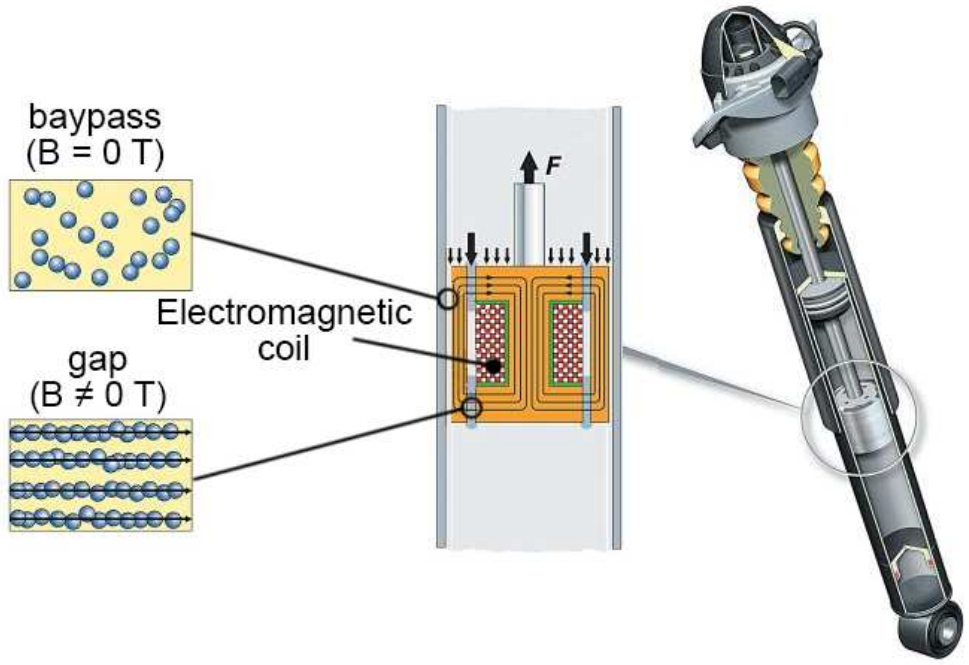

Fig. 31 MR damper with the magnetic circuit in piston [48]

2.5.1 Dynamic force range of MR dampers

Magnetic field influences the MR damper force. Therefore, the force-velocity dependency of the MR damper has to be measured for various magnetic flux density in the gap that means various current in the coil of the damper. Dynamic force range – one of a performance parameter of MR damper is defined by ratio between damping force generated with maximum magnetic flux density in the gap $F_{max}(v,B)$ and the damping force generated with minimum magnetic flux density in the gap $F_{min}(v)$ [49]:

$$D(v_0) = \frac{F_{max}(v_0)}{F_{min}(v_0)} = \frac{F_\tau(\tau_{max}) + F_\eta(v_0) + F_f}{F_\eta(v_0) + F_f} = 1 + \frac{F_\tau(\tau_{max})}{F_\eta(v_0) + F_f} \quad (6)$$

Dimensions of channels which affected the damping force are usually designed using analytical counting base on a so-called parallel plate model, see Fig. 32. The model considers the fluid flow between two parallel plates; the geometry is similar to flowing through the gap of the MR damper [49].

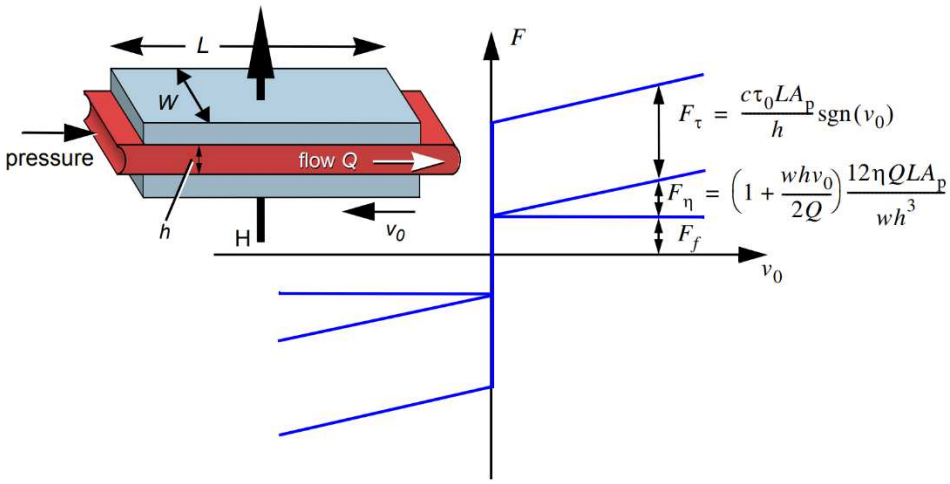

Fig. 32 Forces component of the MR damper [49]

Where: F_f is friction force created by seals, guiding, etc.

F_η is viscous force created by the internal friction of the fluid, $A_p = (\pi/4)\cdot(D\text{-}d)^2$ is an effective area, which is given by the piston D and piston rod d diameters. The viscous force is dependent on the piston velocity v_0.

F_τ is force necessary to overcome the yield stress of MR fluid τ_0, the force can be control by the electric current in the coil. Coefficient c is within the range 2.07 to 3.07 [50].

As shown in Fig. 32, the dynamic range D is dependent on the piston velocity v_0. However, often it is mentioned as a single value, in this case, the value is maximum of dynamic force range – velocity dependency. An example of measured force-velocity dependencies is in Fig. 33 the maximum value of the dynamic force range is approximately 4 around the piston velocity of *0.4 m/s*.

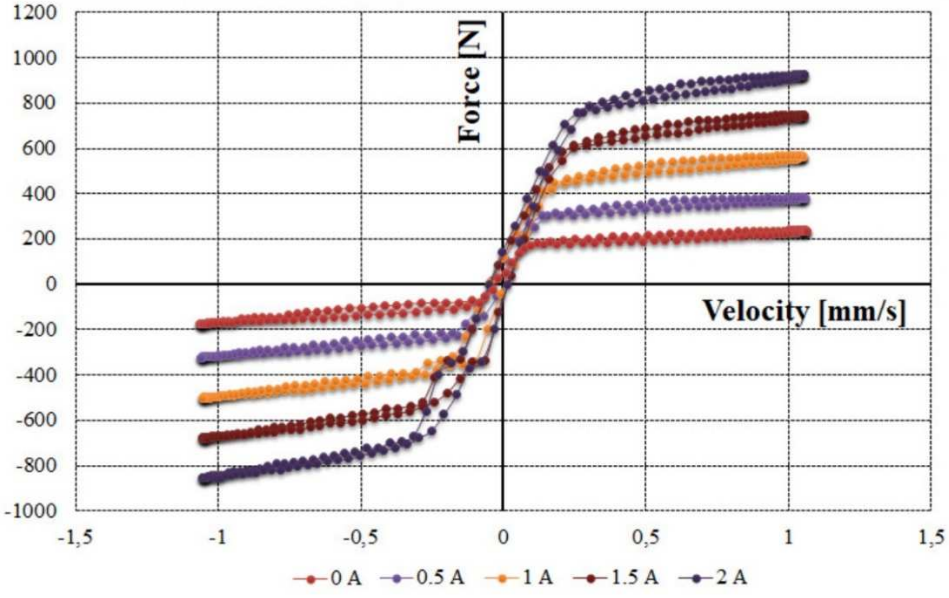

Fig. 33 A typically measured characteristic of MR Damper Force-Velocity response [51]

Measured curves in Fig. 33 exhibit a hysteresis, especially for a low piston velocity. The hysteresis is caused by the elasticity of the measured damper, which cannot be suppressed totally. Therefore, data for force-velocity dependency are processed by the method mentioned in [47], then the final force-velocity dependency has no hysteresis.

2.5.2 The response time of MR dampers

Semi-actively controlled damper performance is among the dynamic force range, given by time period which is necessary to change of damping force - response time. The force increases steeply at the beginning of the switch process, but after a short time, the directive of force increase is lower and lower, see Fig. 34 a). Thus, it is complicated to determine the time between changes of the force from minimum to maximum. Therefore, the time response is reported as time between 0 to 62.3% of maximum value [52, 53] – the primary response or 0 to 95% [49, 55] – the secondary response.

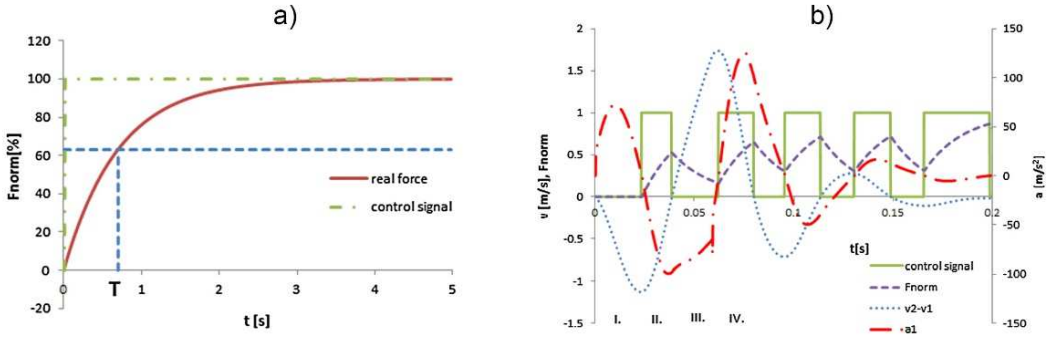

Fig. 34 The response time of MR damper and the influence of response time on semi-active control [53]

Fact that the damping force does not increase immediately due to the effect which is demonstrates in Fig. 34 b). The green curve shows the requirements of damping force. But the response of damper exhibits some delay. Thus, the value of real damping force is not the same to maximum damping force at any time when it is required. This is apparent particularly in pulls around *0.1 s*. At the beginning of this step, the damping force should be zero, but the value managed to fall only to *30 %* of maximal value due to the previous step. After that, the force should be maximal immediately. However, it grows only up to *60%* of maximal value. It is easy to imagine, that the longer the time response the lower the difference between maximum and minimum of damping force, which results in low efficiency of semi-active control.

Total time response of MR damper is influenced by time of current rise, which can be significantly shortened by current [49]; time response of MR fluid itself [52, 56]; and eddy currents which are generated in the coil core [53]. The influence of eddy effect on the MR damper time response depends on the geometry and material of magnetic circuit (coil core).

The eddy currents flow in the perpendicular direction to the magnetic field and they are inducted by magnetic flux density changes [57]. The currents are always closed in loops. These loops generate a secondary magnetic field which has opposite direction to the magnetic field, which causes the eddy currents. The total magnetic

field in the magnetic circuit is given by the sum of both above mentioned magnetic fields. The secondary magnetic field caused by eddy currents achieves the highest intensity during the current step and then decreases over time. Thus, the total magnetic field rises gradually although the current in the coil increase almost immediately. Time response is affected by the size of the material area where the loops can be formed. The smaller the area is the shorter time response the circuit of MR damper exhibits [58].

There are two different approaches to prevent forming of eddy currents in literature: a **material approach** using composite materials for example sintered ferrites of Soft Material Composites (SMC) [59]; or **shape approach** using laminated coil cores [60].

The eddy current loop is not able to cross the insulating layer on the border of metal sheets, see Fig. 34 a) or insulating film in the case of composite material, see Fig. 34 b). The smaller size of loops the lower effect of the eddy currents that result in shorter time response of MR damper.

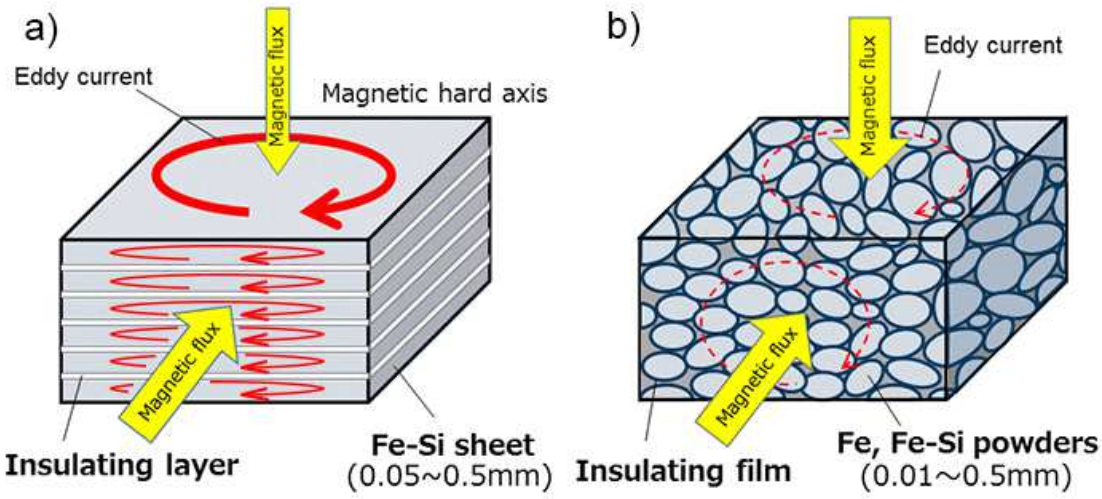

Fig. 35 Eddy currents in magnetic core a) laminated b) composite [61]

2.5.3 MR damper types

2.5.3

Performance of MR dampers is influenced by the design. There are several conceptions: double ended MR damper in Fig. 36 a); double ended damper with external MR valve in Fig. 36 b); and single-ended MR damper in Fig. 36 c). At first glance, a change in the installation dimensions is evident. However, there is also different in which parts are used to magnetic circuit closing. When the magnetic flux flow through parts which can move each other (a) the magnetic field prevents to this movement, this force doesn't depend on the piston velocity and it has the same effect to force-velocity dependency as the Coulomb friction. MR fluid is loaded in shear mode in the case (a). The other MR damper types Fig. 36 b), c) loads the MR fluid in valve mode.

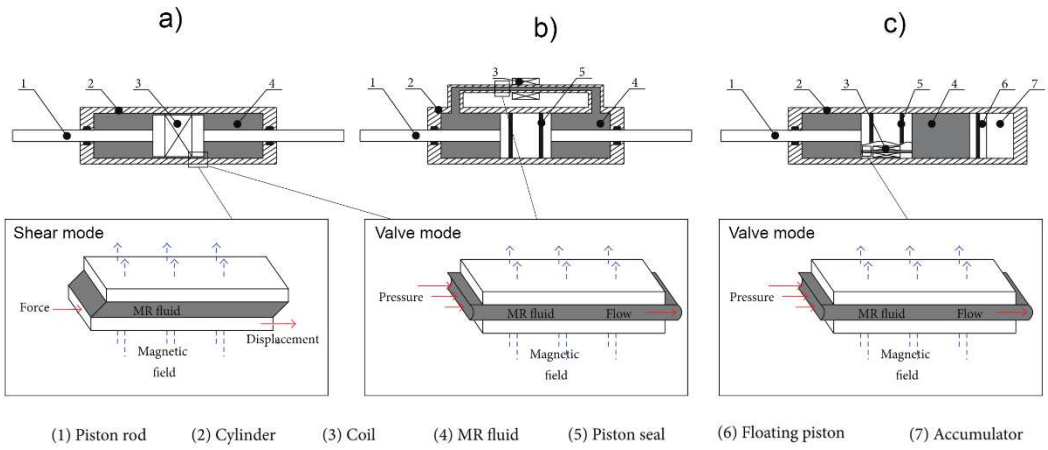

Fig. 36 MR damper types and the modes of MR fluid inside them [62]

Double ended valve MR damper is shown in Fig. 37. It was developed for the civil engineering as a seismic damper of a cable stay bridges. The damping force is very high which is achieved among others using 3 coils in the piston.

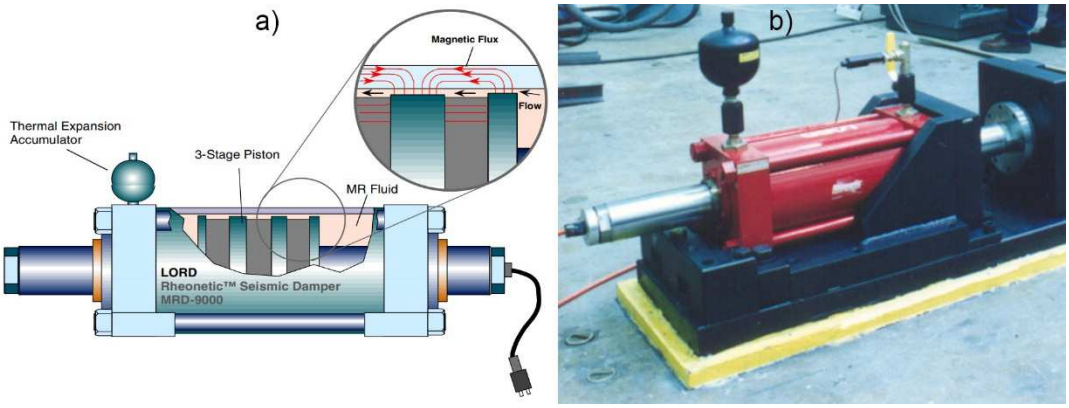

Fig. 37 Large-scale MR damper [49]

Double ended piston rod doesn't provide any changes of internal volume during the damper compression. However, huge damping forces (up to 200 kN) generates a lot of heat, so the damper is equipped with an accumulator for thermal expansion of MR fluid. The accumulator has a membrane which separates the MR fluid and the pressure gas which helps to eliminate the pressure fluctuations caused by temperature.

Damper with an external MR valve was designed for instance by Guo, see [63]. The damper was developed for the railway suspension. An interesting feature of the damper is that the foot valve forces fluid to flow at the same direction regardless of whether the piston moves up or down. Single-directional fluid flow is advantageous for preventing settling of MR fluid, what is caused by the different density of the MR fluid particles and carrier oil. Places with the minimal fluid flow in conventional damper are prone to settle making. Moreover, single-directional fluid flow is better for remixing the fluid.

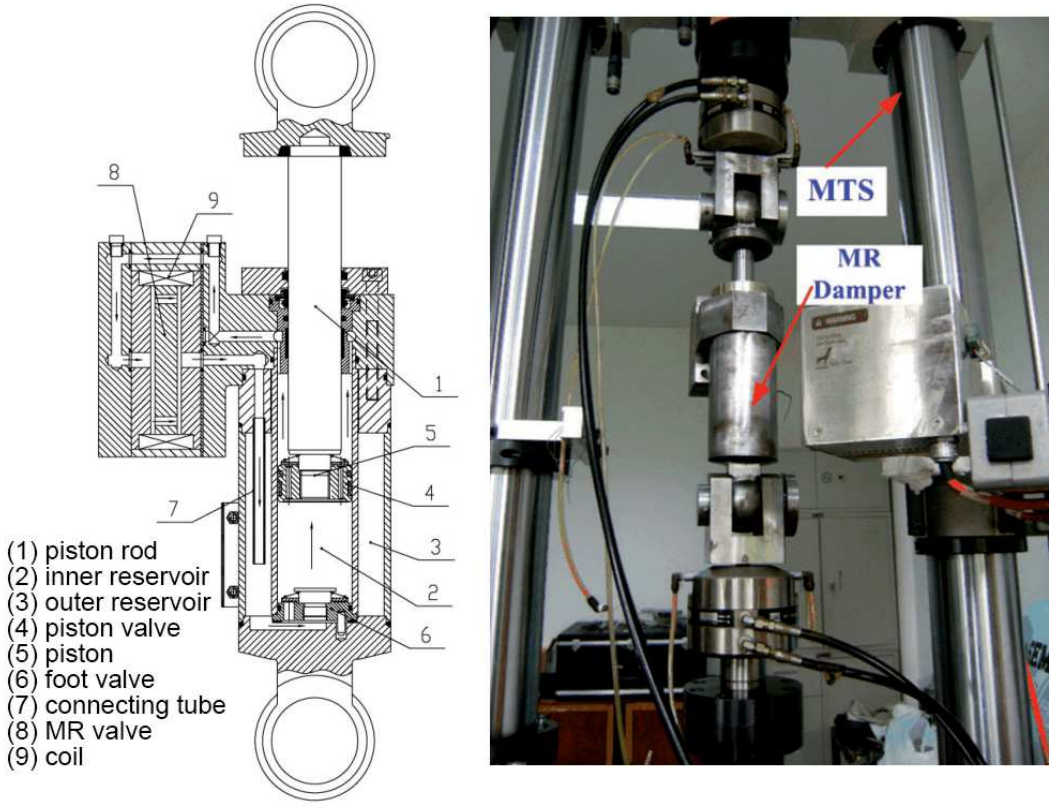

Fig. 38 MR damper with an external MR valve and single-directional flow of fluid [63]

Volume change caused by piston rod insertion is compensated by the pressure increase of the gas in the outer reservoir, see Fig. 38. Mixing the fluid with the gas in the outer reservoir is disable due to the working position of the damper is just vertical and the lower end of the connecting tube is always flooded.

Another way how to compensate of volume changes in a single-ended damper is to used expansion accumulator, see Fig. 39 a) [64] or floating piston, which was used in mass-produced MR damper by Delphi; see Fig. 39 b). This damper was modified in the study [54], Fig. 39 c).

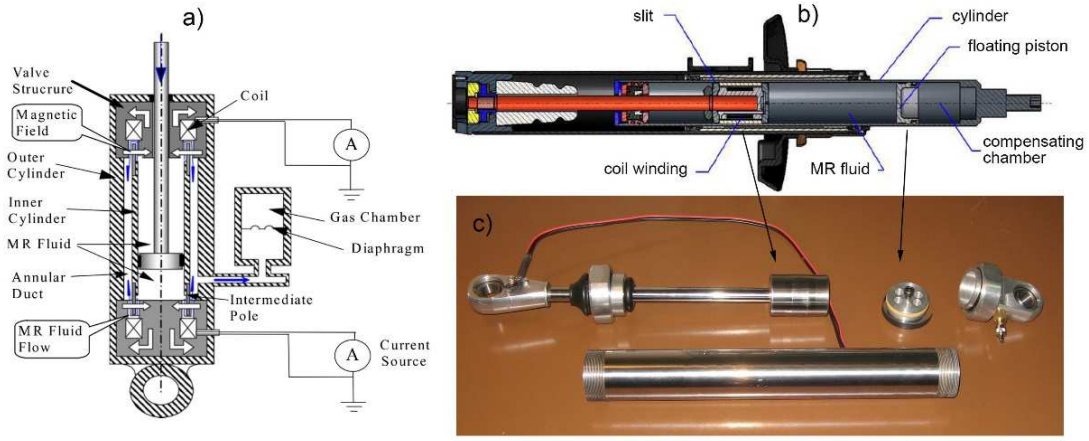

Fig. 39 Several types of MR dampers a) [64], b) [65], c) [54]

Nyguen [64] increased the dynamic range by magnetic circuit optimization. Strecker [54] significantly decrease the time response by the re-design of the magnetic circuit which was made of different material in comparison to the original damper. A comparison of the dynamic force range and the time response of all of the above-mentioned dampers is in chap. 3.

2.5.4 MR damper for the space application

One of the few MR dampers, which were designed for space application, was patented in 2005 [66]. This damper, more precisely strut or an isolator, has internal MR valve and there is no piston rod for a guiding as mentioned in the MR damper types overview in chap. 2.5.3.

Piston movement of the damper causes the fluid flow. There are two possible paths of flow from the outer chamber to the inner one: the first through two gaps with coil along the housing or directly through only one gap and bypass, see in Fig. 40. Both paths cause high damping.

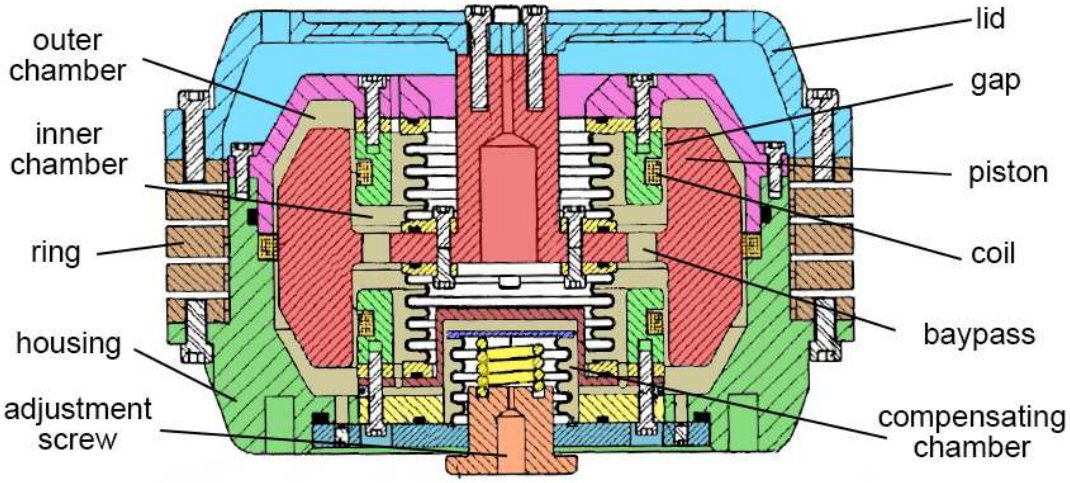

Fig. 40 The response time of MR damper and the influence of response time on semi-active control [66]

An elimination of a thermal expansion is provided by metal bellows which creates a compensating chamber. The bellows is connected by adjustment screw to set a required pressure inside the damper.

The lid serves to the guidance of the piston because the upper part of the lid is weakened what results in elastic deformation in the axial direction, while the stiffness of the lid lateral direction is much higher. Therefore the isolator can be considered single-axis and it is designed for low-stroke applications. The absence of dynamic seals and guidance guarantees no friction force, what should result in high dynamic force range.

2.6 The Evolved Launch Vibration Isolation System analysis

The strut of ELVIS has the most suitable conception for the purpose of this thesis; therefore, it will be analysed thoroughly. The ELVIS was developed by Honeywell, thus in the company which cooperates with on the project which sponsors this thesis. However, the customer was NASA (a competitor of ESA). Therefore, any detailed information about the system was not provided.

2.6.1 Estimation of essential dimensions

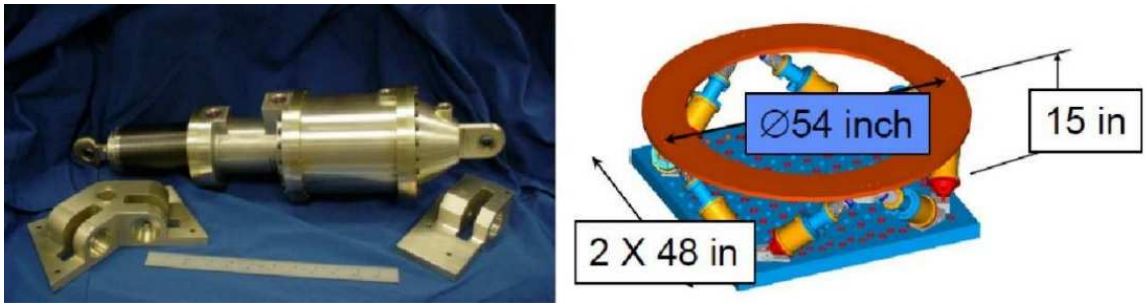

Fig. 41 The dimensions of the ELVIS strut [7]

The total length of the strut was estimated due to the ruler and dimensions in Fig. 41. Subsequently, other dimensions were derived and shown in Fig. 42. This is not a precise method however sufficient for an estimation of several strut parameters.

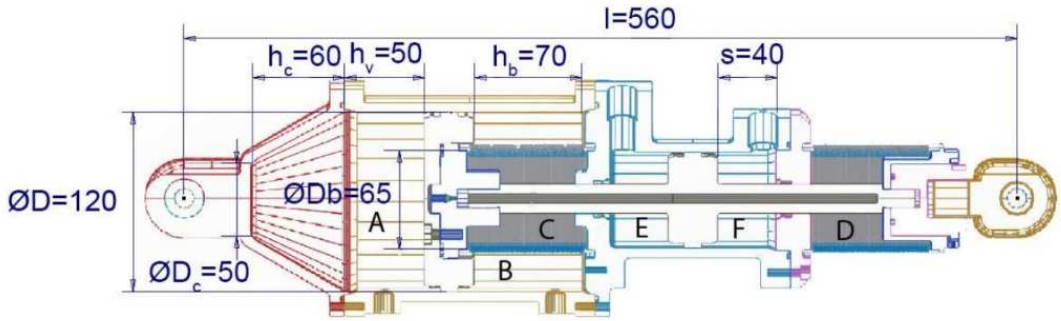

Fig. 42 The estimated dimension of the ELVIS strut [7] (modified)

2.6.2 Stiffness estimation

The stiffness estimation is based on the result of measurement mentioned in chap. 2.2.2. The inclination of the strut in the system was estimated from Fig. 41. Several simplifications have been considered during the estimation: the modal shape of the low-frequency peak is considered purely translational; just 4 struts (oriented to the excitation direction) are active during the excitation in the lateral direction. The equation for determination of the total stiffness of the system in lateral direction k_x was created based on this simplification and the axial stiffness k_A of the strut listed in [7].

$$k_x = \frac{F_x}{\Delta l_x} = \frac{i_x \cdot F_A \cdot \cos\alpha}{\frac{\Delta l}{\cos\alpha}} = i_x \cdot k_A \cdot (\cos\alpha)^2$$

The system stiffness estimation is based on the result shown in Fig. 13.

$$k_x = (2\pi)^2 \cdot m \cdot {f_{xn}}^2$$

The system of equation solution:

$$k_A = \frac{{f_{xn}}^2 \cdot m \cdot (2\pi)^2}{i_x \cdot (\cos\alpha)^2} = \frac{8^2 \cdot 1135 \cdot (2\pi)^2}{4 \cdot (\cos 35)^2} = 1068\ N/mm$$

2.6.3 Bellows axial stiffness estimation

Axial stiffness of the strut consists of a pneumatic spring, stiffness and axial stiffness of both bellows. The pneumatic spring stiffness can be estimated from force-deformation dependency obtained by dimensions of the spring chambers. Consequently, bellows axial stiffness can be counted as total strut stiffness minus the pneumatic spring stiffness.

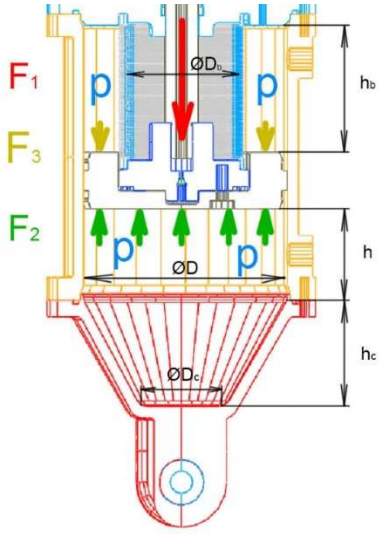

Fig. 43 Scheme of the pneumatic spring in ELVIS strut [7]

The basic feature of the pneumatic spring of the ELVIS strut is equal pressure in both chambers during loading by payload in gravity field *1 g*. Other assumptions are: none preload of the bellows; medium of pneumatic spring is nitrogen with an adiabatic index $\kappa = 1.4$.

An effective area of the chamber under the piston, see Fig. 43:

$$S_A = \pi \cdot \frac{D^2}{4} = \pi \cdot \frac{120^2}{4} = 11\,310\ mm^2$$

An effective area of the chamber above the piston:

$$S_B = \pi \cdot \frac{D^2 - {D_b}^2}{4} = \pi \cdot \frac{120^2 - 65^2}{4} = 7\,991\ mm^2$$

The volume of the chamber under the piston (no strut deformation) consists of the volume of cylindrical *Vv* and conical *Vc* part:

$$V_A = V_v + V_c = h_v \cdot S_A + \frac{\pi \cdot h_c \cdot \left(D^2 + D \cdot D_c + {D_c}^2\right)}{12} =$$
$$50 \cdot 11\,310 + \frac{\pi \cdot 60 \cdot (120^2 + 120 \cdot 50 + 50^2)}{12} = 9{,}072 \cdot 10^5 mm$$

The volume of the chamber above the piston (no strut deformation):

$$V_B = h_b \cdot S_B = 70 \cdot 7\,991 = 5.59 \cdot 10^5 mm$$

A portion of the payload (*m=1135kg*) causes a gravity force acting in the axis of single strut:

$$F_1 = \frac{m \cdot g}{i \cdot \sin(\alpha)} = \frac{1135 \cdot 9.81}{8 \cdot \sin(35)} = 2426N$$

The pressure in both chambers is given forces equilibrium illustrated in Fig. 43.

$$F_1 - F_2 + F_3 = 0$$
$$F_2 = p \cdot S_A$$
$$F_3 = p \cdot S_B$$

Simplified:

$$p = \frac{F_1}{S_A - S_B} = \frac{2426}{11310 - 7991} = 0.731\ MPa$$

Force-deformation dependency is based on dimensions and parameters of the pneumatic spring:

$$F_p(Y) = p.\left(S_A.\left(\frac{V_A}{V_A - S_A \cdot Y}\right)^{\kappa} - S_B.\left(\frac{V_B}{V_B + S_B \cdot Y}\right)^{\kappa}\right)$$

The pneumatic spring stiffness as a point estimation around zero deformation of the strut (*Y=0mm*)

$$k_p = \frac{F_p(1) - F_p(-1)}{2} = \frac{2687 - 2164}{2} = 261\ N/mm$$

Axial stiffness of both bellows:

$$k_{ax\_bell} = k_A - k_p = 1068 - 261 = 807\ N/mm$$

Force-deformation dependency of the strut

$$F_s = F_p + Y \cdot k_{ax\_bell}$$

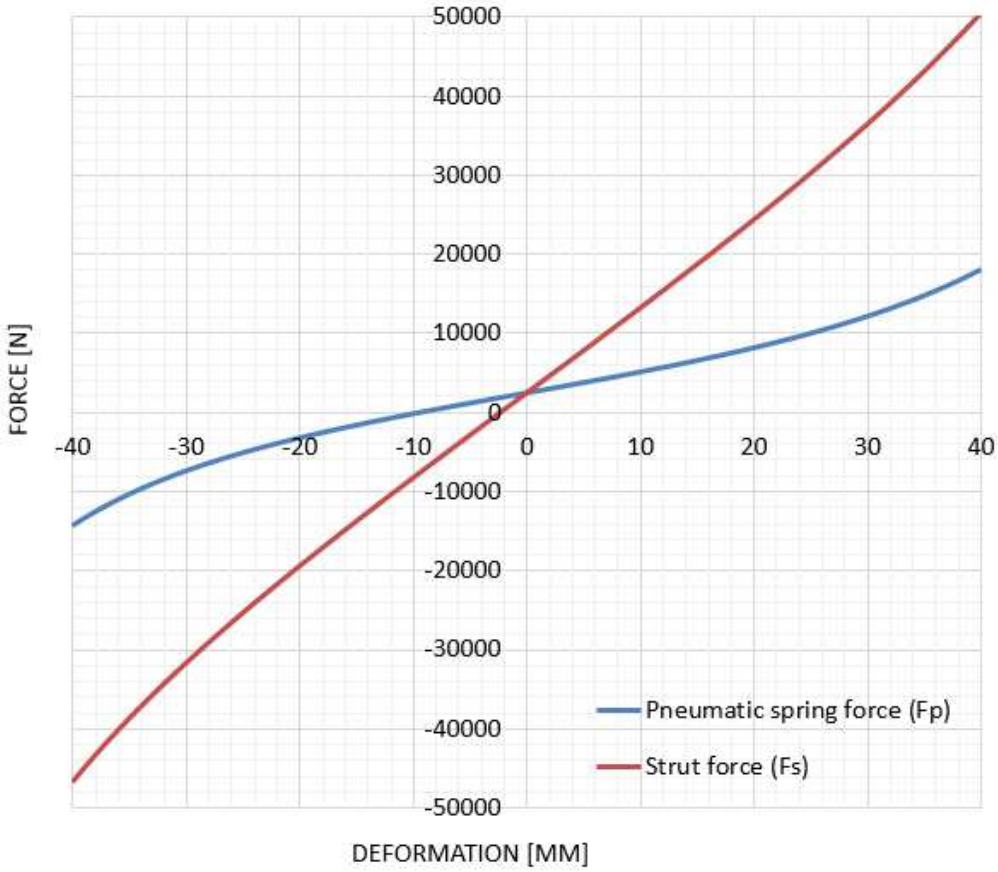

Fig. 44 Estimated force-deformation dependency of the ELVIS strut

3 CONCLUSIONS OF LITERATURE REVIEW

The vibration environment during a flight of the launch vehicle is very dangerous for the valuable payload (spacecraft). Two basic types of vibration isolation systems (VIS) were used for the space applications: mechanical and structural. Mechanical VISs were used with passive (whole spacecraft isolation) or active (light part of the spacecraft) control.

The passive VIS excels with reliability and none energy consumption, on the other hand, the active VIS is very effective in vibration elimination. However, the efficiency is accompanied by high energy consumption of the actuators [67]. The third option of vibration elimination is a semi-active system, which has much lower energy demands compared with the active one but at the same time, it is more efficient than the passive VIS. Semi-active control can be achieved by MR dampers.

Single axis elements such as actuators, struts etc. used for vibration elimination must be united in a mechanism with 6 DOF. A literature review points out the Stewart platform as the best candidate. It is usually consists of 6 actuators and this active mechanism, is used also for positioning of light mass devices. However, this design can be also applied for the passive platform where the legs are struts, which combines spring and damper. One of such as the design of passive Stewart platform is called ELVIS.

The Stewart platform's strut parameters (stiffness, damping, etc.) affect the platform parameter in all directions simultaneously. It is advantageous to get much stiffer lateral direction of VIS than the axial one, because of payload shape, especially centre of gravity height. Therefore, the ELVIS is equipped with a hydraulic stabilizer, which prevents the payload yawing; while, the axial stiffness is not influenced by the stabilizer. Pipeline diameter of the ELVIS stabilizer were designed small in order to minimize weight and maximize its stiffness. It caused additional damping during oscillation in the axial direction, caused by the fluid flow. It can be taken as an advantage in passive VIS, but in semi-active control, the OFF state damping should be as low as possible. Therefore, this version of the stabilizer is not convenient, for a semi-active VIS.

The lateral stiffness increase can be also provided by torsion stabilizer, which has minimal passive losses. However, the torsion stabilizer has to be placed into at least two perpendicular planes to increase the stiffness in any lateral direction (perpendicular to the lunch vehicle flight).

All struts used for the space applications which were filled with a fluid were sealed by elastic metal bellows and some static seals. Conventional sealing by dynamic seals between the piston rod and a damper body are not allowed in this field, because a leaked fluid would evaporate due to atmospheric pressure drop. Consequently, condensation of the vapour, could short circuit of the spacecraft electronic parts, which may endanger the mission.

Available literature did not provide any information on how to determine the volumetric stiffness of metal bellows neither the pressure thrust stiffness (projection of volumetric stiffness into the axial direction). The pressure thrust stiffness determination is necessary for the strut design. Therefore, FEA will be used for the pressure thrust stiffness determination using the bellows geometry. Thakkar [41] compared two approaches of shell parts structural analysis. The first approach used "shell" elements and the part was modelled without any symmetry. The second

approach used “solid” elements and the rotational symmetry. Results obtained by these two methods were similar. However, a model of bellows filled with a fluid cannot use “shell” elements, because of the fluid and the wall interaction.

An effective MR damper used for semi-active control is characterized by a short time response and a high dynamic force range. The area of interest is given by a specific application of the damper. This can be illustrated as a rectangle in Fig. 45 which dimensions correspond to ranges of mentioned parameters (time response, dynamic force range) suitable for the specific application. Suspension system employing the MR damper with the parameters lying in this area will be able to significantly decrease the transmissibility of vibration in comparison with the suspension system using the MR damper with one or both parameters out of this rectangle.

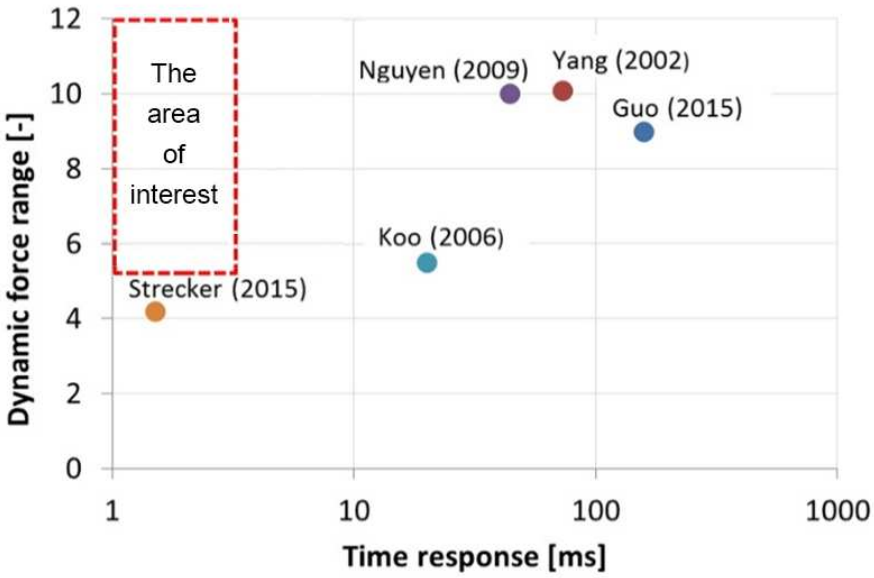

Fig. 45 Time response – Dynamic force range dependency of existing MR dampers

The aim of this thesis is to design a semi-active vibration isolation strut consist of MR damper and springs. The ELVIS strut was chosen as one of the possible sources of inspiration. Therefore, this strut was thoroughly analyzed.

4 AIM OF THE THESIS

Vibration isolation system for the launch vehicle is a complex task, which was planned as a multiannual project for the specialized companies with the comprehensive research team. This thesis is focused on the design of key element of the vibration isolation system.

The aim of the thesis:
Design of semi-active strut combining spring and damper function for the vibration isolation system of the launch vehicle.

Sub-aims:

- Multi-body model of vibration isolation system
- Detailed multi-body model of the single strut for VIS
- Mechanical, hydraulic, pneumatic and magnetic analysis for the optimal strut dimensioning
- Design and manufacture of an experimental strut for laboratory testing
- Verification the experimental strut functionality during vibration tests
- Design of the strut for VIS of the launch vehicle

Assignment and methods:

The strut dimensioning is based on the whole VIS requirements:

Dimensions of VIS:	Connection diameter $\emptyset D_B = 1920\ mm$ (VIS and the launch vehicle interface) Minimum height $h_{min} = 400\ mm$
Payload:	Mass $m = 1500\ kg$ Centre of gravity height $h_{CoG} = 1{,}5\ m$ Connection diameter $\emptyset D = 1280\ mm$ (VIS and the payload interface)
Max. acceleration in launch vehicle:	Lateral direction $a_x = \pm 0{,}9$ g Axial (longitudinal) direction $a_y = +5.5$ g
VIS + payload natural frequency:	Lateral direction $f_x = 3 – 25$ Hz Axial direction $f_y = 8 – 45$ Hz
Max. displacement of payload:	Lateral direction $d_x = 30$ mm Axial direction $d_y = 10$ mm

The VIS multi-body model will be used for determination of those strut parameters, which will secure the above-mentioned requirements and the vibration transmissibility of the system as low as possible. The model will provide an operating

condition of the single strut in VIS (stroke, load, etc.) which will be used in the detailed multi-body model of the single strut.

Multi-body model of the single strut will be used to define the area of interest for the MR strut, see Fig. 45. Suitable time response and dynamic force range depend on the specific application; therefore, the area of interest has to be determined for the strut application in the VIS. Multi-body model of the strut will be verified by experiment.

The MR strut will be designed in two versions:

Experimental:	verification of the multi-body model of the strut
Final:	use in the VIS of the launch vehicle

Strut design will be adapted to their use. The experimental MR strut will serve as a zero prototype. That means the knowledge gained during testing will serves in the design of the final strut. Design process will used many models and calculations for optimal dimensioning of the strut. Inputs outputs and interconnection of the models and other procedures during the design process is shown in Fig. 47.

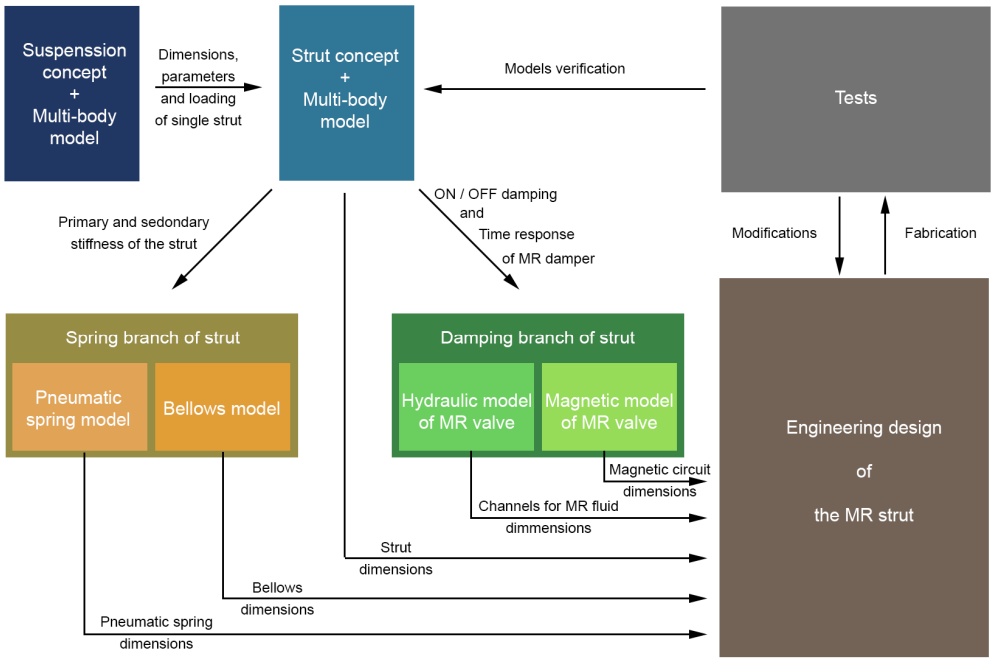

Fig. 46 Scheme of MR strut design process

Both versions of the struts will use metal bellows. The pressure thrust stiffness from the bellows geometry must be determined. The literature review helped to find the most suitable approach using FEA and it also defined the elements.

5 DESIGN OF MR STRUT

5.1 Conceptual design

5.1.1 Vibration isolation system

The literature review identified the most suitable mechanism of VIS is the Stewart platform. Considering that the system will incorporate the mechanical stabilizer, the number of struts is 8.

Mechanism of VIS is placed between two cones. The control electronics of the launch vehicle can be hidden in a lower part of VIS and it is mechanically separate from the payload environment by a membrane. Lower cone has to be high at least *400 mm* due to the height of control electronics.

The upper part of VIS serves for the payload connection. The force distribution along the diameter should be as uniform as possible. This feature of VIS should improve upper cone, which structure reduces the force peaks in the strut connections.

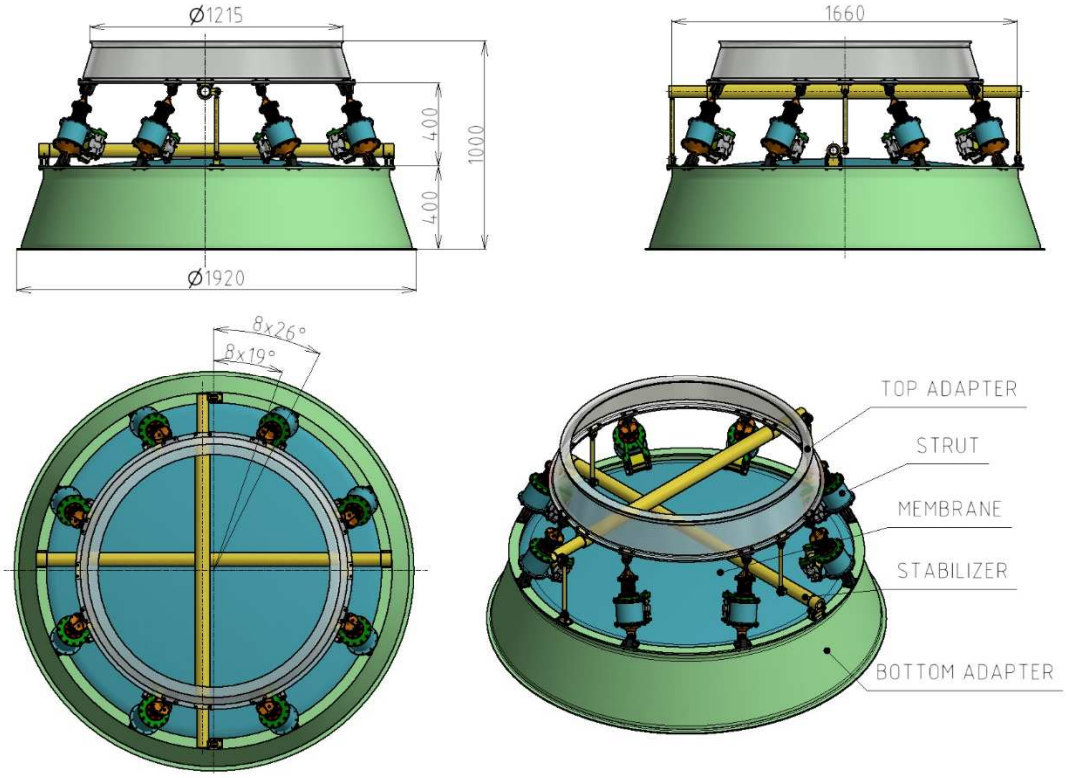

Fig. 47 Conceptual design of VIS for launch vehicle

Feasibility study of this concept was provided within the project for ESA, on which our research group cooperated under the leadership of company Honeywell in 2014 – 2016. The conceptual design corresponds to FLPP 3 (level of design quality), it is important to the Stewart platform dimension determination.

5.1.2 MR Strut

The literature review described some struts used previously for the purpose of vibration isolation for space application. The strut of ELVIS was chosen as the most suitable source of inspiration for the new MR strut. The pneumatic spring will ensure the dominant part of the primary stiffness of the MR strut. This spring is suitable especially for the possibility of the pressure regulation and for the equal pressure under and above the piston in static load created by payload in gravitation field *1 g*.

Axial stiffness of metal bellows will contribute the primary stiffness of the strut. Moreover, these flexible parts will serve as the case of the damping medium – MR fluid. Thus, the conventional piston rod seals will not use, because of higher friction and a risk of leakage in comparison of metal bellows sealed by static seals.

Hydraulic stabilizer chambers are not respected from the ELVIS strut design, because the stabilizer of VIS described in this study will be mechanical. This concept of stabilization is more advantageous with regard to damping of the stabilizer.

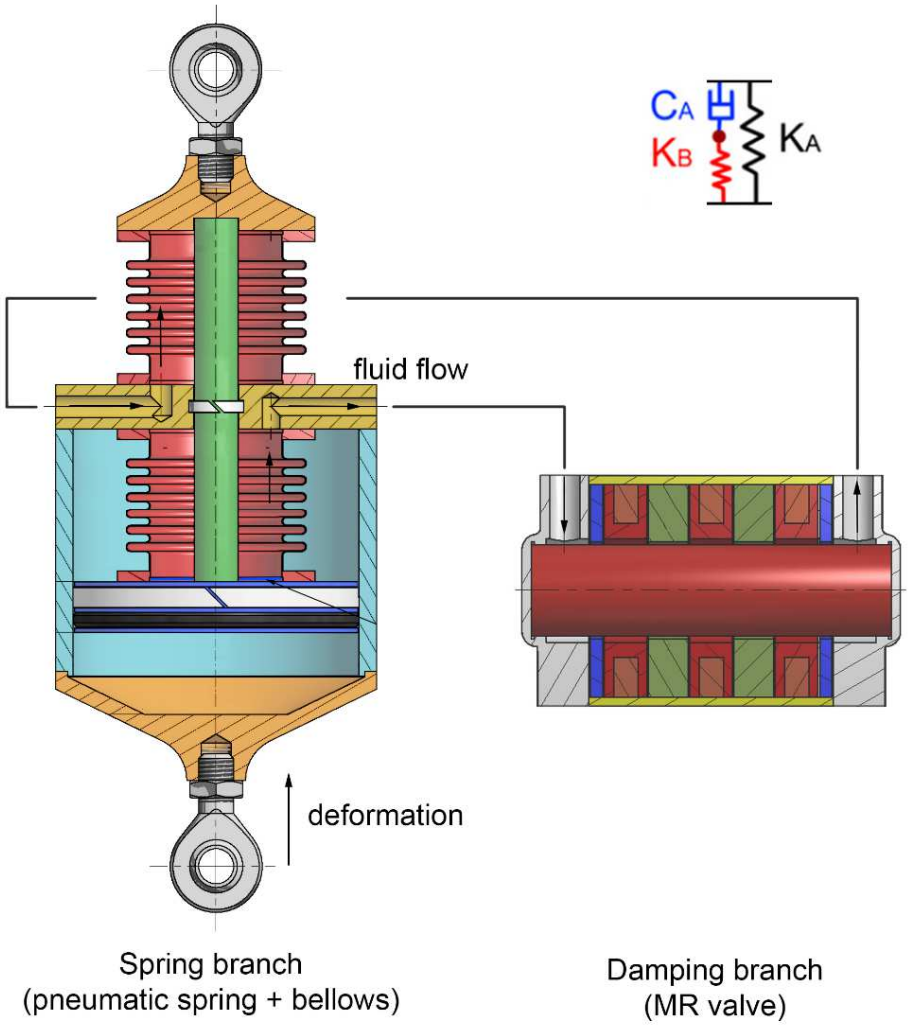

Fig. 48 Conceptual design of the MR strut

5.2 Dimensions and parameters determination of VIS and strut 5.1

Force affecting on each strut can be determined by the system of motion laws solution. One of the possible methods is to create a model in the multi-body system, which solves the system of equation of motion based on the geometry and other parameters which are inserted into the model, this method was used for example in [69]. Bodies with much higher stiffness than the primary stiffness of the strut will be considered as rigid, that means the cones, payload etc. The cones elasticity will not have a negligible effect on the transmissibility of VIS as well as the real payload consist of several parts which are connected together elastically. However, an elasticity of cones and flexible payload could make the design unnecessarily complicated.

The payload behaviour on the Stewart platform was simulated by the model in multi-body system ADAMS. A complex model of vibration isolation system was operated only in passive mode and with linear elements, that means the stiffness and damping of the strut were constant. More sophisticated simulation such as semi-active control was provided in detail model of the strut, especially for lower time requirements. Also, the verification by measurement can be provided much easier with a model of the single strut. However, boundary conditions were determined in the model of VIS.

5.2.1 Multi-body model of VIS 5.2.1

Multi-body model of VIS consists of two rigid bodies, which are interconnected by 8 struts and a mechanical stabilizer. Lower (green) body - base represents the launch vehicle, thus the source of vibration with acceleration $\ddot{x}_0$. Upper (yellow) body represents a payload and the response on the excitation is measured by the acceleration of payload $\ddot{x}$.

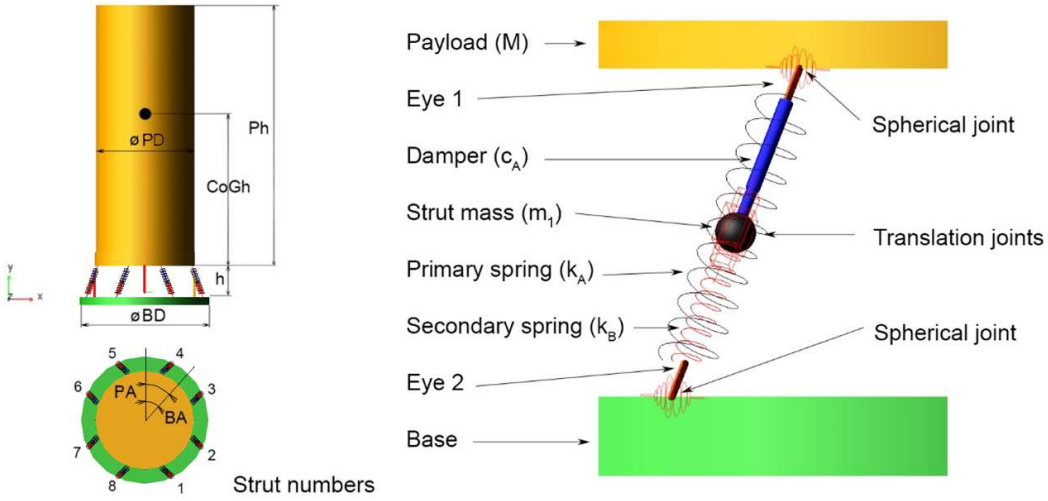

Fig. 49 Scheme of VIS multi-body model

Each of the struts consists of two branches, which are connected in parallel. Spring branch consists of only one part – spring with a stiffness k_A which is marked as the primary stiffness of the strut. Damping branch is consisting of the damper with

constant damping c_A the spring connected in series with stiffness k_B which is marked as the secondary stiffness of the strut. To connect two elements which can produce a force, a body with nonzero mass m_1 is necessary. In this case, the body is between the spring k_B and damper c_A and represents the strut mass, more precisely the mass of parts which are moving during the damping. Both of the branches are connected by eyes, which are constrained by one direction movement relative to m_1 body and by spherical join with the payload or the base.

Preliminarily tests have shown that the combination of natural frequency in lateral and axial direction cannot be achieved only by struts. Therefore, the stabilizer was added into the model, first as the torsion spring with stiffness k_{ms} between the base and the payload, see the left side of Fig. 50. Then, the torsion spring k_{tp} was loaded by a lever mechanism, see the right side of Fig. 50 to allow the lever and the torsion bar dimensioning.

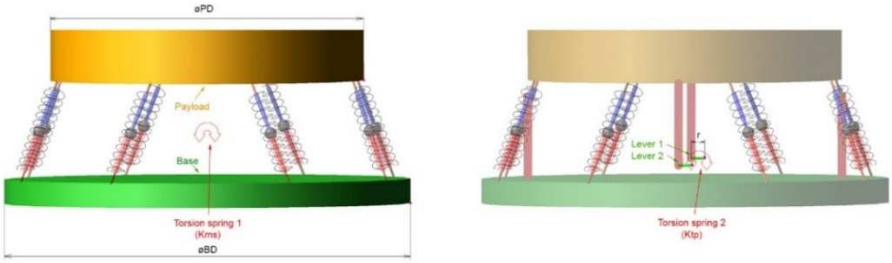

Fig. 50 Mechanical stabilizer in multi-body model

The model was created as parametric because of the possibility of easily change of strut position, inclination, etc. An effect of some parameters listed in tab. 2 is often affected by another parameter. For example, the stiffness k_B increase in combination with low damping c_A cause the transmissibility increase. While the same increase of the stiffness k_B in combination with high damping c_A may cause the transmissibility decrease. However, Fig. 51 shows the result of the simulation, where just one parameter was changed and other ones were kept on the values listed in the tab. 2. The results were obtained in the interface between payload and the VIS, that means the lowest point of the payload.

tab. 2 The Stewart platform parameters

Parameter	Symbol	Value	Unit
Payload mass	M	1 500	[kg]
Payload diameter	PD	1 280	[mm]
Base diameter	BD	1 660	[mm]
Angle between struts along the payload perimeter	PA	19	[deg]
Angle between struts along the payload perimeter	BA	26	[deg]
Platform height	h	400	[mm]
Primary stiffness of the strut	k_A	1230	[N/mm]
Damping of the strut	c_A	26	[Ns/mm]
Secondary stiffness of the strut	k_B	61 500	[N/mm]
Ratio k_B/k_A	N	50	[-]
Torsion stiffness of stabilizer	k_{MS}	$1.072 \cdot 10^7$	[Nm/rad]

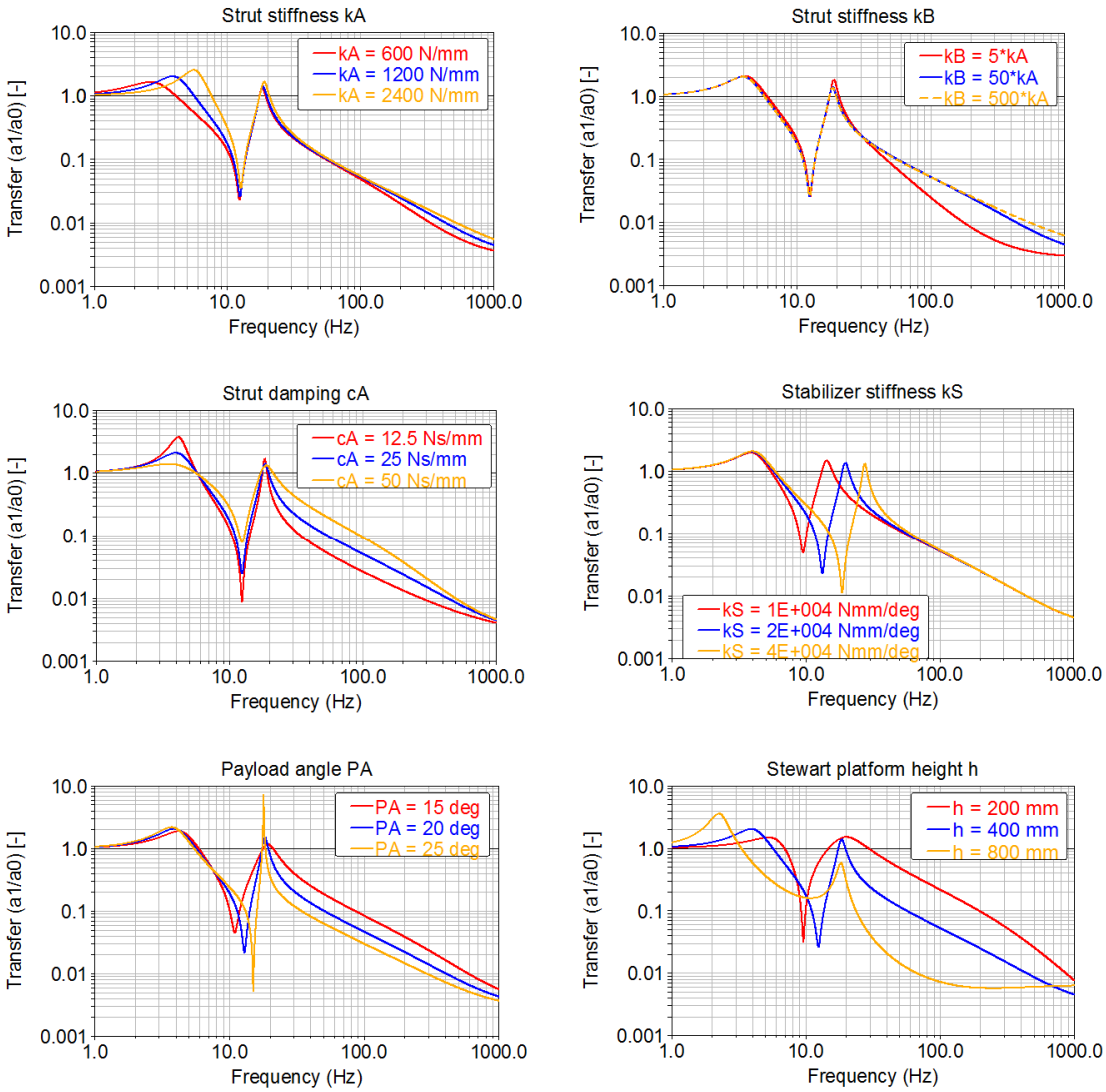

Fig. 51 The parameter influence on the transmissibility (measured at the VIS/payload interface)

Determination of optimal combination of parameters is complicating the process, it was provided in the cooperation with company Honeywell. The final combination of the VIS parameters in the tab. 2 was chosen by visual observation of the transfer ratios. The purpose was created with maximum damping of MR damper, this value is considered as constant damping c_A. Which approximately corresponds to the state with maximal current in the coil and the shear stress in the gap of damper does not overcome the yield stress of MR fluid – the fluid flow only through the bypass. Springs are also considered as linear, friction caused by guidance and seals of real of the struts were neglected. VIS with parameters listed in tab. 2 was excited by the constant acceleration of amplitude *1 g*, in lateral *X* and axial *Y* direction. The results in form of the transfer ratios are shown in Fig. 52.

The VIS with final parameter response

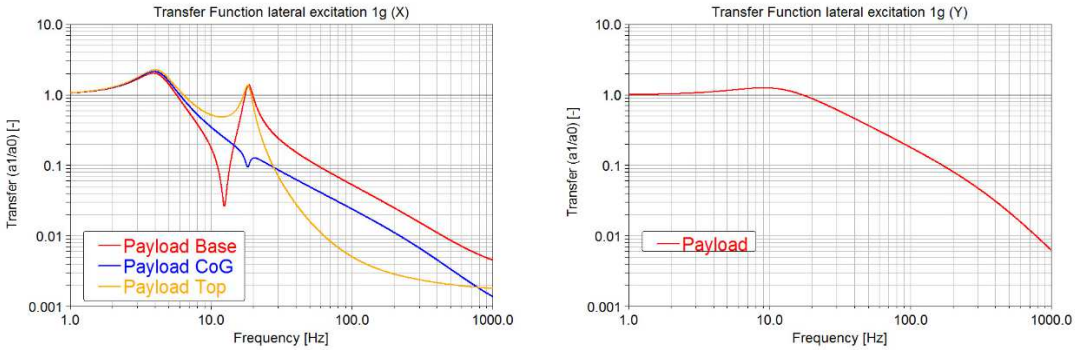

Fig. 52 Transmissibility function of the VIS + the payload system

The force and displacement in time (in frequency) is shown in Fig. 53. The time and frequency have the same value because time increase by one second means the excitation frequency increase by one hertz. The almost symmetrical layout of the struts in VIS causes almost the same load of every single strut. Therefore, only one strut force – in strut number *1* was plotted (see strut numbers in Fig. 49). The maximum strut deformation is given by the superposition of quasi-static and dynamic excitation and it is around *17 mm*. So, a stroke of the strut with this value of (constant) stiffness should be *20 mm*.

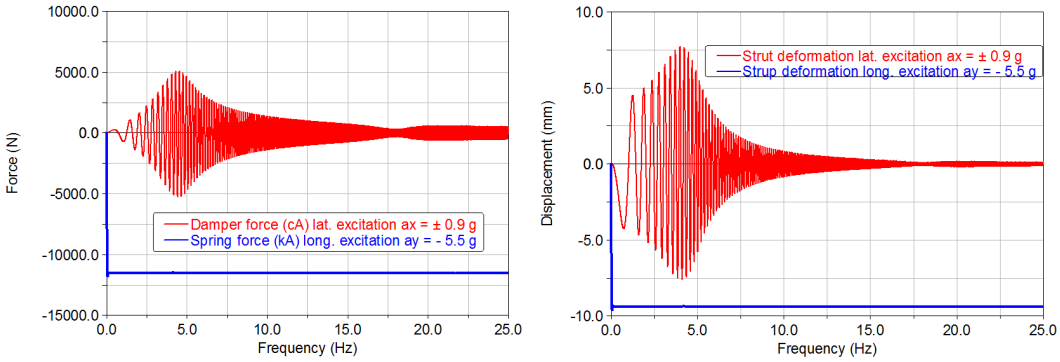

Fig. 53 Strut force and deformation during dynamic (lat.) and quasi-static (ax.) load

The payload displacement during dynamic (lateral) and quasi-static (axial) excitation is within the permissible range defined in chap. 4. The transmissibility functions comparison shows that the maximum is in the top position of the payload. The other points of the payload are not shown in Fig. 54. Payload displacement during quasi-static load in axial direction exceeds the limit a little. However, progressive force-deformation dependency of pneumatic spring should decrease this maximum of payload displacement under the *10 mm* which is the limit.

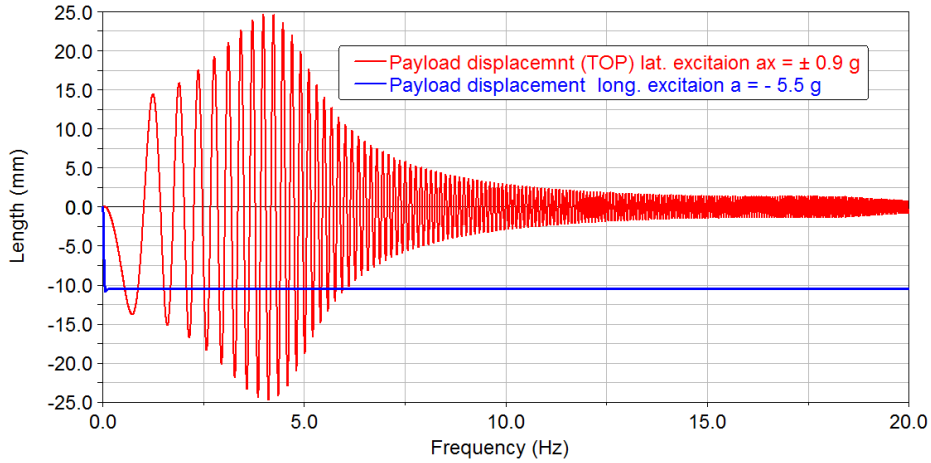

Fig. 54 Payload displacement during dynamic (lat.) and quasi-static (ax.) load

Load of the strut for its dimensioning

Maximum strut force is able to determine only in the case when the excitation is well known. But the vibration environment in the launch vehicle can be predicted just roughly. Therefore, the maximum strut force was obtained as the sum of force caused by the quasi-static acceleration in axial direction *5.5 g* and maximum damping force during harmonic excitation of acceleration in a lateral direction with amplitude *0.9 g*. Consequently, the sum was multiple by safety factor *2*.

tab. 3 Limit forces of the MR strut

Parameter	Symbol	Value	Unit
Quasi-static force in the strut (5.5g)	$F_{5.5g}$	11.9	[kN]
Damping force	F_C	5.06	[kN]
Total strut force	F_{SDE}	33.92	[kN]

5.2.2 Multi-body model of single

The boundary conditions of the single strut model are based on the axial excitation of the VIS multi-body model. 8 struts with an inclination relative to the base plate are replaced by a single strut in the axial direction. Thus, the payload mass part which is supported by every single strut is approximately 1/8 of the total payload mass. Effect of the strut inclination causes the decrease of relative mass of a single strut. However, with respect to performance, the dynamometer at our laboratory, the payload mass for experimental strut was chosen *100 kg*. The stiffness and damping of the experimental strut were chosen was chosen so that the transmissibility was similar to the VIS + payload system, see right side of Fig. 52.

Multi-body model of single strut consists of three bodies: base (where the excitation is applied) payload, (where the response is measured) and m_1, which represents the mass of moving parts of the damper. This body is connected with payload by damper c_A and with the base by spring k_1.

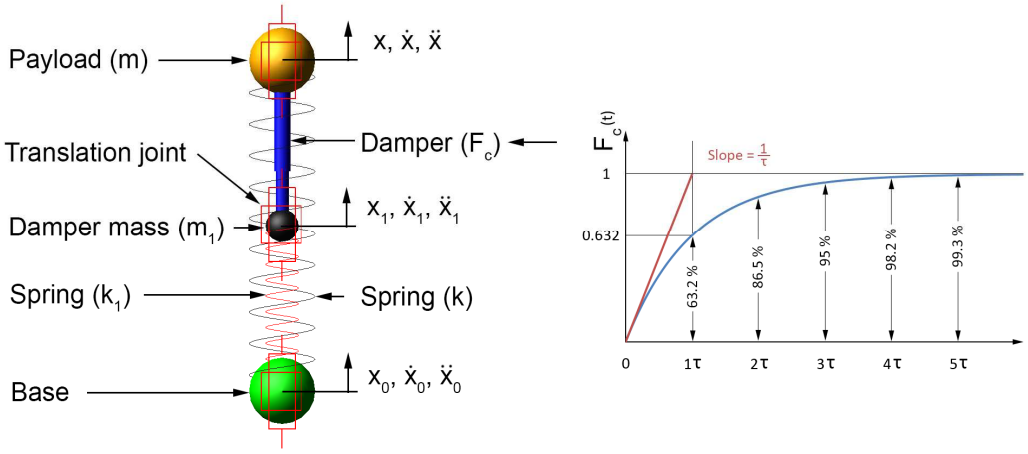

Fig. 55 Scheme of single strut model

Parameters of the single strut model were determined by the VIS simulations:

tab. 4 Required parameters of the experimental strut

Parameter	Symbol	Value	Unit
Experimental payload mass	m	100	[kg]
Primary stiffness of experimental strut	k	400	[N/mm]
Damping of the strut (activated state)	C_{ON}	12.5	[Ns/mm]
Time response of the damper	t	2	[ms]
Dynamic force range of the damper ($D= C_{ON}/C_{OFF}$)	D	10	[-]
Secondary stiffness of experimental strut	k_1	50*k	[N/mm]

Effect of last three parameters on the transmissibility in semi-active control mode is described below. Only one parameter was changed during the simulations and the other parameters are kept on the values listed in the tab. 4. The base is excited by the axial acceleration of amplitude *1 g*. Frequency increases linearly from *0* to *100 Hz*, simulation time was *100 s* and number of steps *400 000*.

Time response

A time delay of damping force increase was inserted into the model to observe the behaviour of the mass during the semi-active control of the strut. The force increasing is similar to the response of the first order system, see in the right side of Fig. 55. Dynamic force range of the damper can be modified. The dynamic force range is defined as the ratio between maximal and minimal damping force. Dynamic force range increase provided in this study means the minimum damping drop while the maximum damping is kept. Damping force can be control by the semi-active algorithm. The position of the damper between the payload and the body m_1 caused slight changes of equations (5), for the ON/OFF Skyhook algorithm:

$$\begin{aligned} \dot{x} \cdot (\dot{x} - \dot{x}_1) \geq 0 \ &\rightarrow Fc = Fc_{max} \\ \dot{x} \cdot (\dot{x} - \dot{x}_1) < 0 \ &\rightarrow Fc = Fc_{min} \end{aligned} \qquad (7)$$

The model behaviour is presented during the excitation with constant acceleration with a frequency which is close to the natural frequency of the system, in this case approximately *10 Hz*. Damping force requirements are shown in Fig. 56 (black dashed line). Damping force of the damper with time response: *1 ms* is red; *10 ms* is blue. It is obvious that the slower damper does not meet the requirements of the algorithm and the damping force is not used in its limit values.

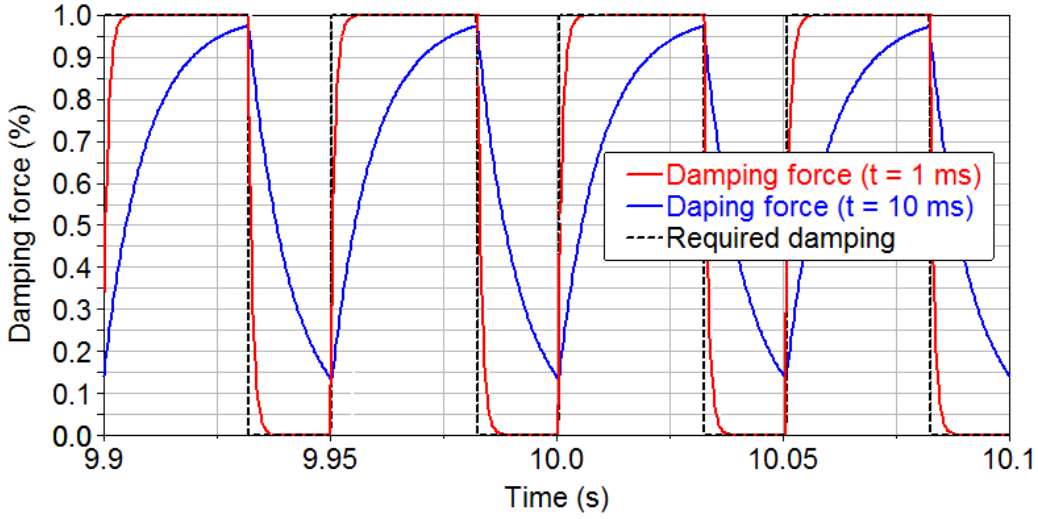

Fig. 56 Damping force ratio during harmonic excitation at frequency 10 Hz

Damping force of the faster damper has the sharper change that the damper with time response *10 ms*.

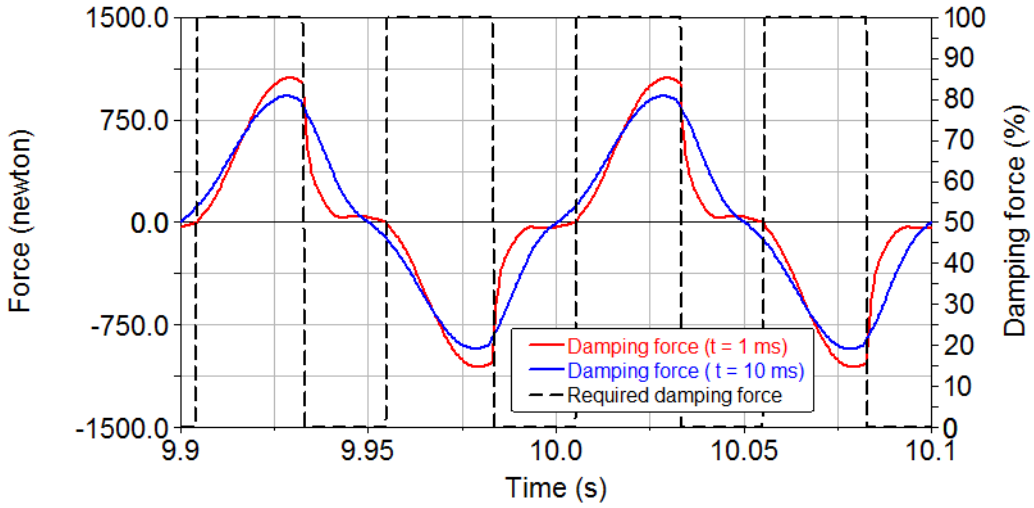

Fig. 57 Damping force during semi-active control, excitation frequency: 10 Hz

Time response of the damper affects the sprung mass (payload) acceleration. The shape of the curve for a damper with time response *1 ms* is similar to the theoretical model, see the curve of acceleration in Fig. 6. However, there are two differences, the first is that the acceleration drop is not absolutely steep, because of the time response

1 ms. The second difference is that the acceleration does not decrease onto zero value, because Liu considered no damping of inactivated (OFF) state in his study, while simulation in this thesis considers that damping force in OFF state is 10 times lower than the force of activated (ON) state. Thus, the dynamic force range is *D = 10*.

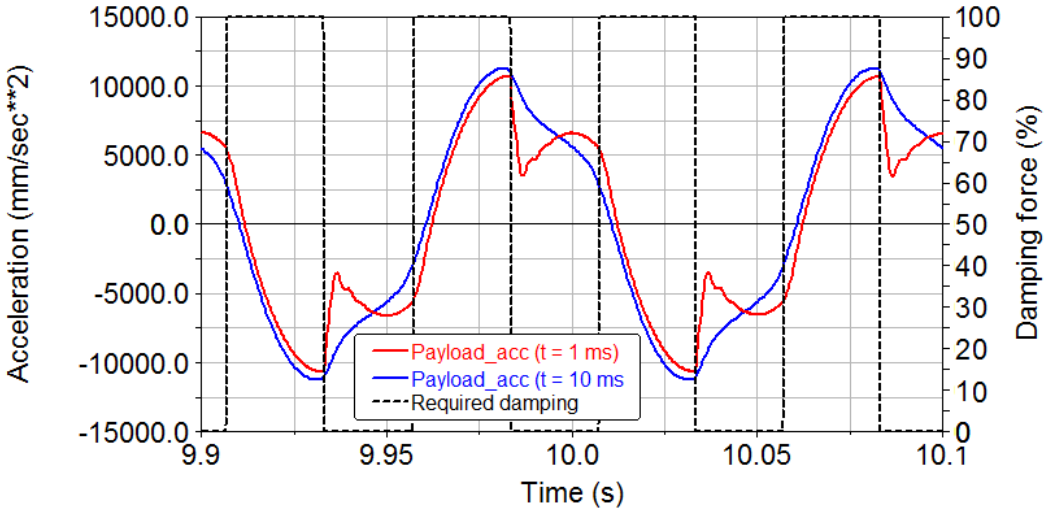

Fig. 58 Acceleration of sprung mass during semi-active control, excitation frequency: 10 Hz

Acceleration signals of the payload and the base were transfer into the frequency spectra using Fast Fourier Transformation (FFT) and the amplitudes of both signals were divided for the same frequencies. This calculation results in “transmissibility function”. However, considering that thy system is not linear, the designation as the function is not clear. Therefore, “the transfer ratio” will be used:

$$T(f) = \frac{\ddot{x}(f)}{\ddot{x}_0(f)} \tag{5}$$

The dependency of time response on the transfer ratio is shown in Fig. 59.

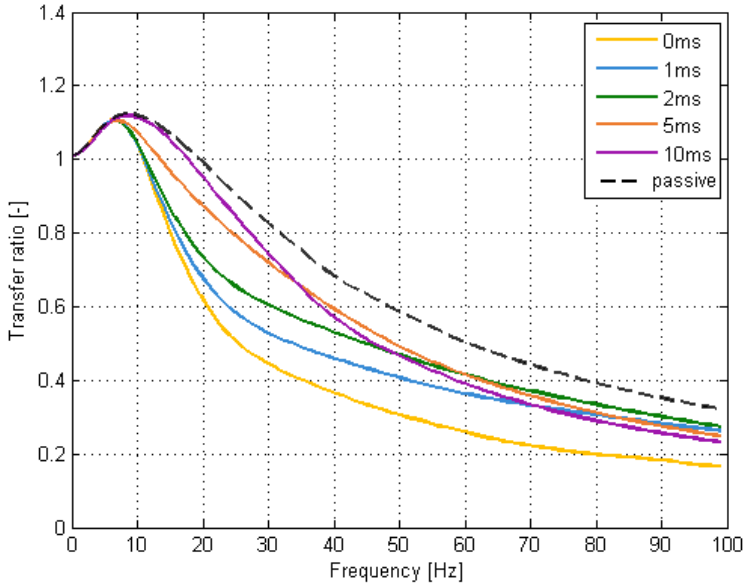

Fig. 59 Influence of time response on the transfer ratio

Simulation confirmed the hypothesis that the time response increase results in the higher amount of vibration transfer onto the sprung mass by the semi-active controlled strut. The system behaviour at the frequencies higher than in this case from 5*0 Hz* is distorted by the fact that the excitation was harmonic. Thus, the damping of the damper with slow time response for example *10 ms* has stabilized on a specific value which results in lower transfer ratio than the ratio achieved by semi-actively controlled damper with faster response, for example, *2 ms*. However, this "advantage" of slower damper would probably not be confirmed in the case of real excitation, for random vibration. A significant benefit of semi-active control was observed for the dampers with the time response lower than *5 ms*. A system with the damper with time response *10 ms* has similar transfer ratio in the vicinity of resonance in compare of passive mode. Therefore, the time response of the MR strut should be lower than *5 ms*.

Dynamic force range

Simulations deals with the dynamic force range were provided with the constant damping in ON state, listed in tab. 4. The value of dynamic range affects just the damping in OFF state. Also, the theoretical situation that the damping force in OFF state is zero was included in the simulation to assess a limit above which the dynamic range increasing is useless. Results in Fig. 60 show that the transfer ratio of the system equipped with damper with dynamic force range *D = 50* is similar than the transfer ratio of the system with the damper with dynamic force range infinitely high. Dynamic force range increase causes a significant decrease of the transfer ratio at isolation area, but also a slight increase in the vicinity of the resonance. This handicap of semi-active control can be mitigated by the proportional control of the damping force. That means to use an algorithm which switches between more than two levels of damping as the ON/OFF Skyhook.

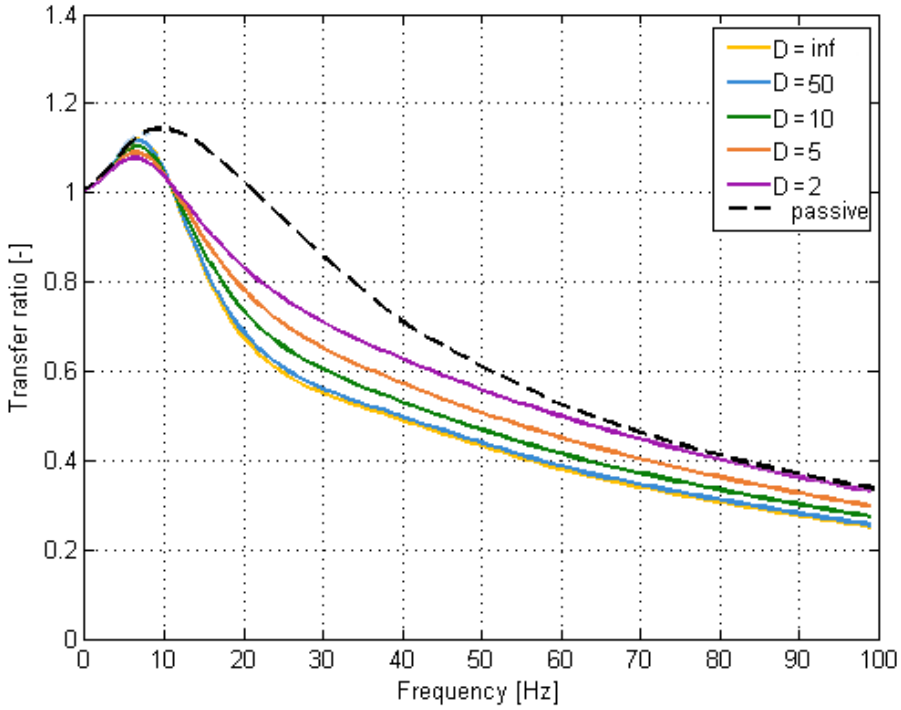

Fig. 60 Influence of dynamic force range on the transfer ratio

Dynamic range higher than *5* proves to be suitable for this system as suitable, because, the transfer ratio was significantly lower than the transfer ratio achieved by passive damping. However, the dynamic force increased over the value *10* has minimal benefit onto the transfer ratio. Therefore, the dynamic range of the MR strut should be between *5* and *10*.

Secondary stiffness k_1

The dependency of the time response and dynamic force range on the transfer of the system with a rigidly connected damper is described in [70]. However, the damper in the strut is connected elastically. Therefore it is necessary to determine the effect secondary stiffness on the transfer ratio when the semi-active ON/OFF Skyhook controls the damping force. The influence of the secondary stiffness on the transfer ratio is valid for the parameters listed in the tab. 4 and plotted in Fig. 61.

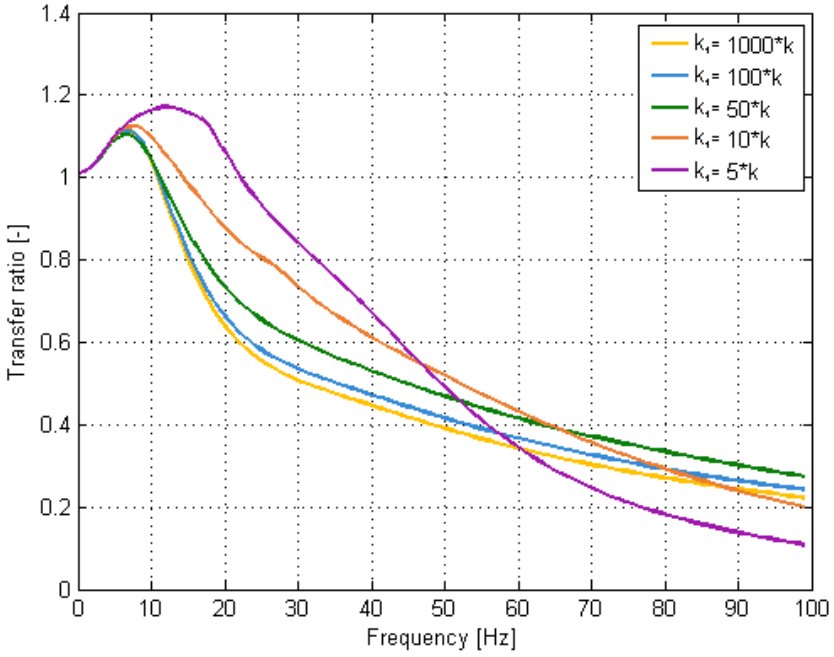

Fig. 61 Influence of dynamic force range on the transfer ratio

The flexibility of the damper connection affects the transfer ratio negatively in the vicinity of resonance, but its benefit (shown for a passive system in Fig. 3) is evident also in the case of damper which is semi-actively control. Therefore, the semi-active control decreases the transfer function up to some frequency (depends on the time response of the damper) and the transfer ratio at a higher frequency will be decreased using the elastically connected damper effect.

Different time response causes different influence of the flexible connection of the damper on the transfer function, see Fig. 62. The faster damper in the system the lower sensibility of the system on the flexible connection of the damper. That means the increase of maximum transfer ratio is not so significant and the intersection of transfer ratio curves for $k_1=5*k$ and $k_1=500*k$ is at different frequencies for the fast damper compares with a slower one.

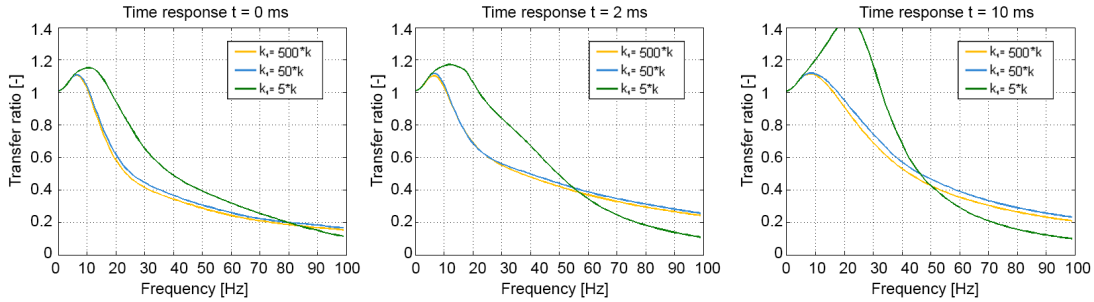

Fig. 62 Influence of flexibility of the semi-actively controlled damper connection on the transfer ratio

5.3 Experimental MR strut design

The functionality verification of MR strut is necessary before the final design of MR strut for space application. Therefore, the experimental strut was manufactured and tested. Moreover, some vibration experiments with the experimental strut were used for verification of multi-body model described in chap. 5.2.2. The experimental strut consists of two coil springs, bellows unit, and an external magnetorheological valve. This strut was inserted into the system (demonstrator) which is illustrated in Fig. 63. Excitation is provided by the hydraulic actuator; sprung mass is realized by a set of weights. The sprung mass and actuator are connected by the experimental strut. Therefore, the transmissibility of the experimental strut can be determined by measurement of acceleration bellow (actuator) $\ddot{x}_0$ and above (sprung mass) $\ddot{x}$ the strut.

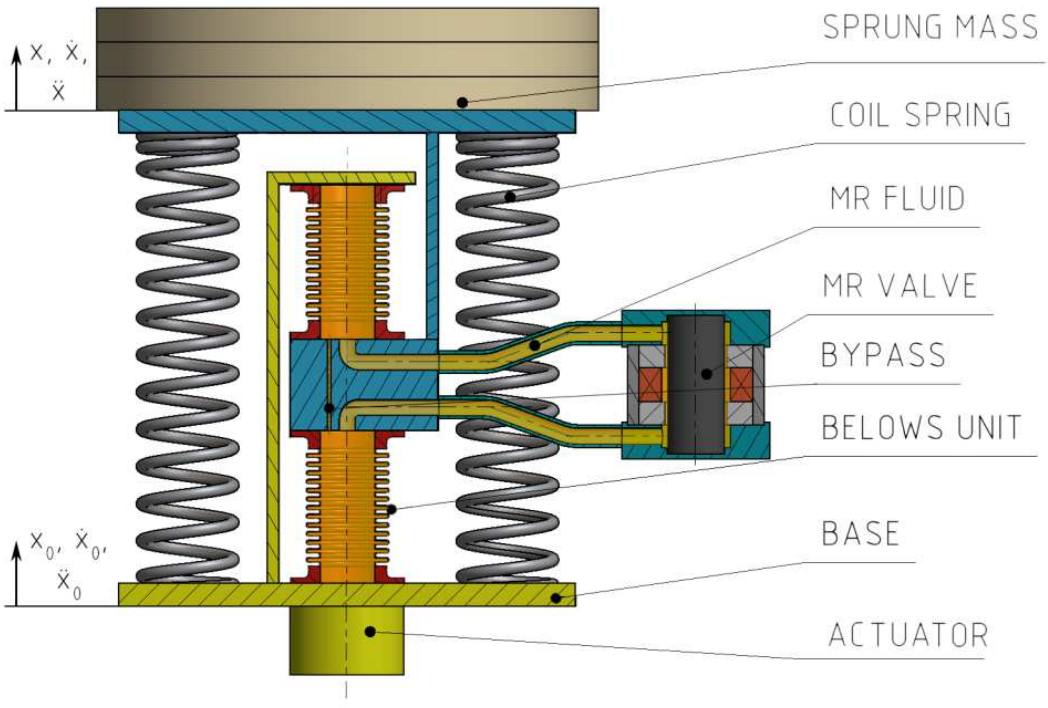

Fig. 63 Experimental strut in the demonstrator

Bellows unit forces MR fluid to flow through the MR valve. Lids of the new damper (pos. 1) in Fig. 64 are connected by the metal sheet (pos. 2). Considering that the central part (pos. 3) is fixed, movement of the upper lid down cause compression of the upper bellows, while lower bellows (pos. 4) is lengthened. Length change of bellows caused the MR fluid flow via two channels. The first one is through the hole marked A1 then through the fitting (pos. 5) and the pipes to the external MR valve and then back to the bellows unit through the hole A2. The second channel is, directly through the bypass hole B which is drilled in two plugs (pos. 6). The stopper (pos. 7) prevents the metal bellows from excessive deformation. Moreover, the stopper fills the space in the bellows, thus decrease the amount of MR fluid in the bellows, which leads to cost but mainly weight reduction.

The bellows unit can be screwed to the weights and the actuator via threaded holes in the frame (pos. 8) and in the lid (pos. 1). This connecting hole in the lid can also be used for filling the fluid. It is sealed with the screw (pos. 9) and the O-ring (pos. 10) and it is tightened to conical countersink. This is an unconventional method of sealing; therefore, a leakage test was performed prior to manufacturing of the lids.

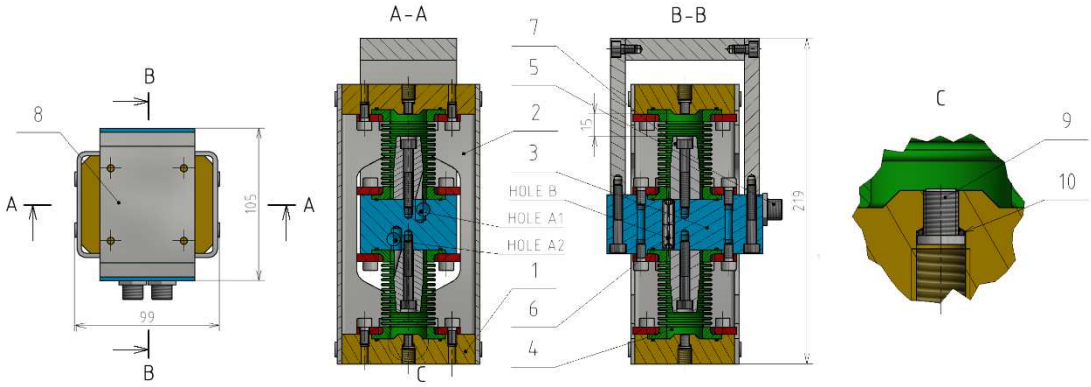

Fig. 64 Bellows unit

The central part (pos. 3) is screwed to the sprung mass via a frame (pos. 8). Another connection hole is in the lower lid (pos. 1). This thread serves to connect the bellows unit to the actuator.

Magnetorheological valve was designed using analytical models described in studies [49, 68[68]. Dr. Kubík was the lead designer of the MR valve. It consists of 3 coils, magnetic flux flows via the coil core (pos. 5) in Fig. 65, pole pieces (pos. 2 and 3) and the outer tube (pos. 4). Together, these components form 4 gaps, where the MR effect can be created. The total length of the gaps is *34 mm*. The MR fluid flows from (and back) the bellows unit due to pipe-lines screwed to the lids (pos. 8).

Parts of the MR valve are colour-coded in Fig. 65 depends on material: grey colour indicates steel (S235JR), red - aluminium (EN AW-6060), blue - plastic (POM), orange-copper (Cu), black – rubber (NBR), yellow - MR fluid (LORD 132 DG) and the green parts are made of ferrite (N95). The magnetic circuit is mainly made of ferrite, this sintered material was chosen because of low electric conductivity, which prevents the eddy currents forming and decreases time response of the damper [72]. However, ferrite is fragile and hard to the machine; therefore, the outer tube is made of steel.

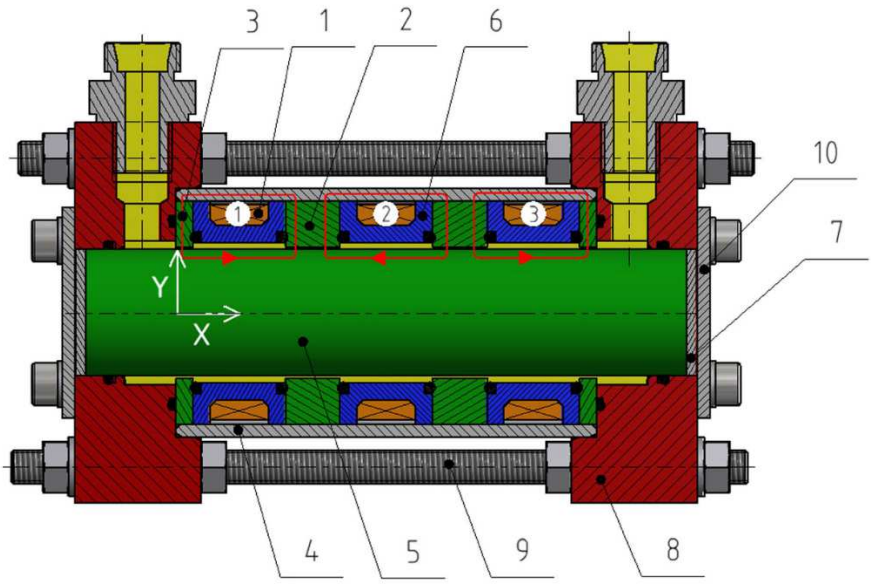

Fig. 65 MR valve

5.3.1 Demonstrator of the experimental MR strut

Parts of bellows unit, MR valve, weights, etc. were manufactured and assembled in accordance with the scheme in Fig. 63. The bellows unit is in Fig. 66 shown without the sheets, which connected the lids and without the frame, because of greater clarity. MR valve is equipped with the pressure sensor *HBM 154210274* and the valve which is used to connect the expansion tank, which is necessary to easy change of the pressure inside the experimental strut.

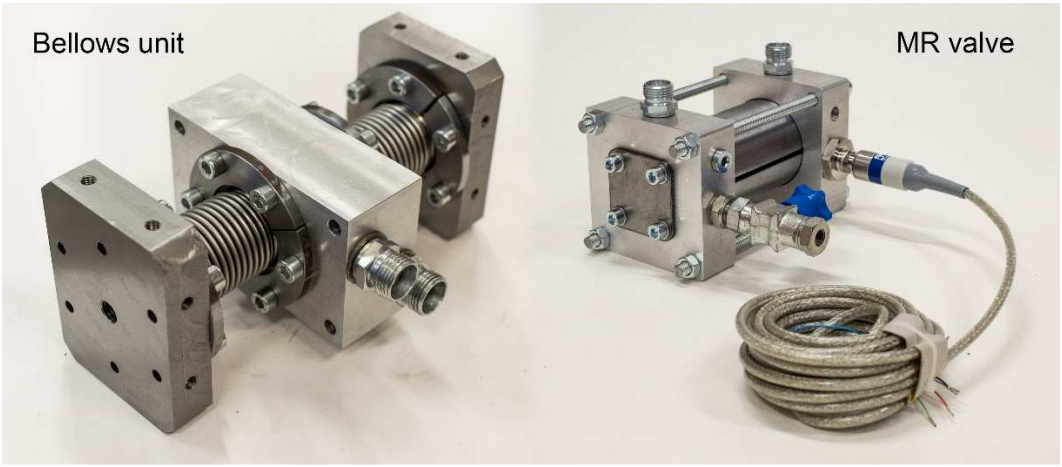

Fig. 66 Important parts of the experimental MR strut

Both components of MR strut shown in Fig. 66 were separately filled with the MR fluid and then interconnected by pipe made of steel. After that, the MR strut was deaerated. The steel pipes were used because of higher volumetric stiffness in compare with the rubber hoses, which were planned to use originally.

Fig. 67 Demonstrator for the experimental strut vibration isolation properties verification

Excitation is realized by a hydraulic dynamometer (actuator), which displacement was set that its acceleration was constant *1 g* in a whole range of tested frequencies. The acceleration was measured by accelerometer *B&K 4507B* screwed to the base, see detail at the bottom right of Fig. 67. The same sensor was placed at the sprung mass. The ratio of these two signals gives a transmissibility of the experimental strut. Position sensor *VLP 15 SA 150* was inserted between the base and the sprung mass. The relative velocity between these two bodies was calculated by derivation of the position signal.

5.3.2 Experimental verification of the strut parameters

Force-velocity dependency determination requires a force measurement. Therefore, the load cell *INTERFACE 1730ACK-50kN* was inserted between the frame and the sprung mass, see Fig. 68. Velocity was determined by the position sensor signal derivation.

Fig. 68 Demonstrator configuration for the F-v dependency measurement

The strut was compressed by the actuator with linear sweep sine function with amplitude *5 mm*, frequency grew from *0.1* to *8 Hz*. Zero position of the actuator was set that, the force measured by load cell is zero. Only the points measured in zero position of the actuator was used to the Force-velocity dependency determination. Thanks to that, any spring forces were eliminated and the force-velocity dependency does not exhibit a hysteresis. The scheme for this method is shown in Fig. 69.

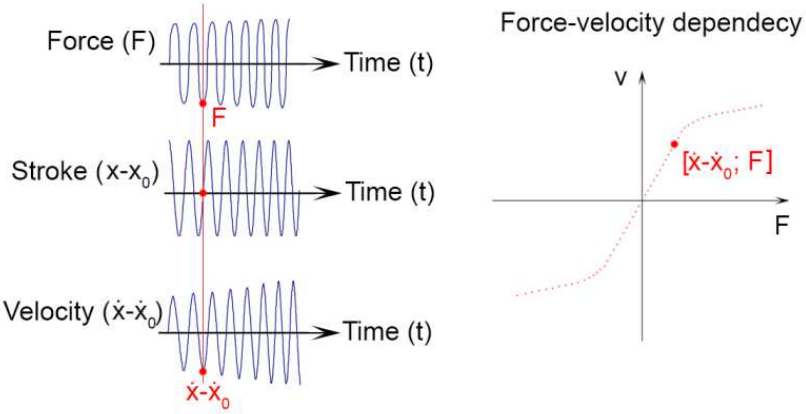

Fig. 69 Method of F-v dependency determination

The gradient of the force-velocity dependency at low relative velocities $\dot{x} - \dot{x}_0$ is influenced by bypass orifice diameter, which was chosen *1.45 mm* for these measurements. Damping was measured for several various current in the coil. The magnetic flux density in the coil core was near to saturation of ferrite material in the case when the current in the coil *I = 1 A* was used. Thus, increasing of the current over this value does not significantly increase damping force.

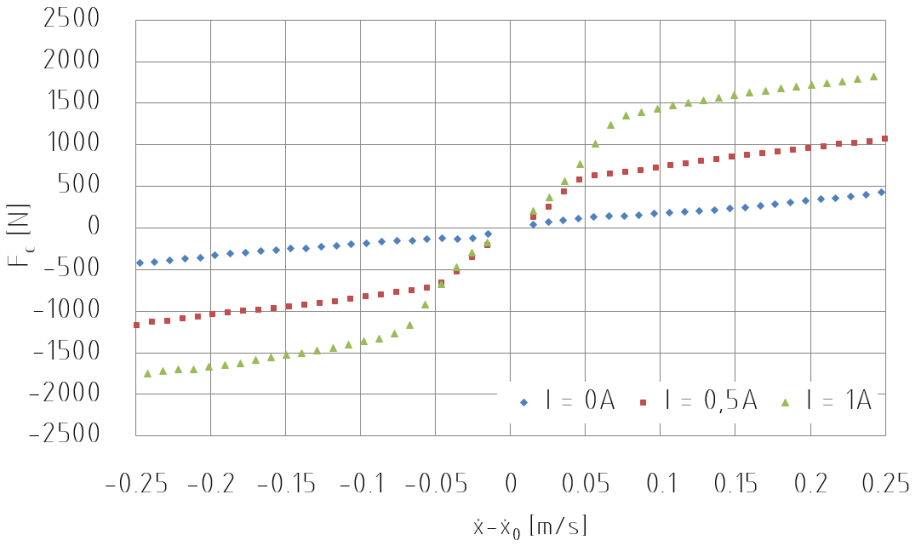

Fig. 70 The F-v-I dependency of the MR valve

Dynamic force range was determined using equation (6), in this case, a ratio of damping forces with maximum and minimum current in the coil: *D(v) = F (I = 1 A) / F (I = 0 A)*. Dynamic force range depends on the relative velocity $\dot{x} - \dot{x}_0$, see Fig. 71. Maximum of MR valve dynamic force range is around velocity *0.08 m/s*, thus near the knee of force-velocity dependency with current in the coil *I = 1A*. Dynamic force range at low piston velocities could increase with non-using of the bypass [49]. However, test with MR damper without the bypass shows a significant increase of the system transmissibility, see chap. 5.3.4; therefore, this version was abandoned.

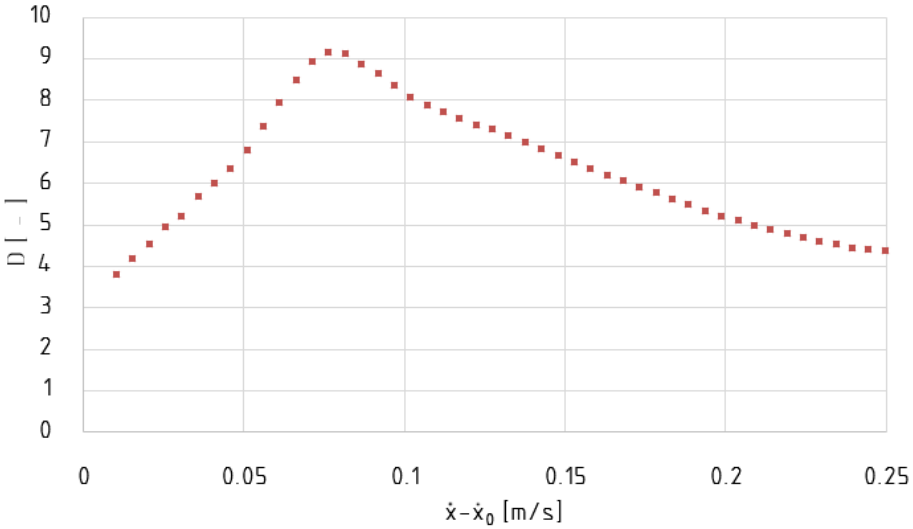

Fig. 71 Dynamic force range of the MR valve

Time response of the experimental strut at the demonstrator. Current controller patented by Dr. Strecker was used for rapid change of current in the coil. Switching between maximum $I = 1\ A$ and minimum $I = 0\ A$ current was ensured by Arduino board. An important requirement for this measurement is that all measured signals have to be synchronous; therefore, only one data analyzer *DEWE 50* was used for the signals.

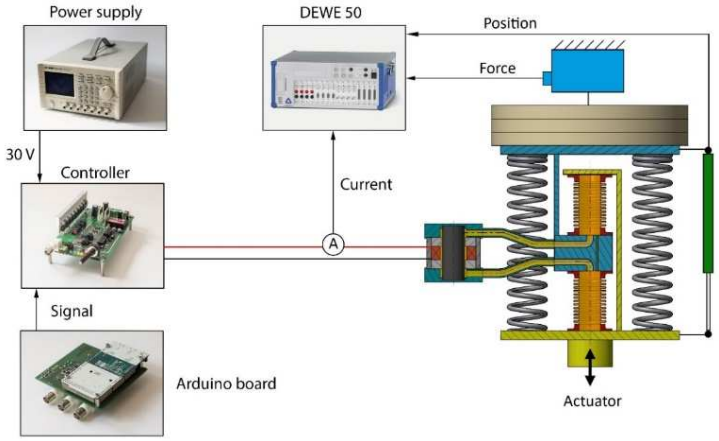

Fig. 72 Scheme of experimental MR strut time response measurement

The position sensor is located between the sprung mass and actuator; thus, it measures the deformation of the strut and not just the damper deformation as shown in Fig. 48. However, the absence of piston in the bellows unit does not allow to measure strut deformation without the deformation caused by secondary spring of the strut - pressure thrust stiffness of bellows k_B. This fact slightly increased time response which was measured.

Time response of the MR valve was measured with triangular signal excitation with amplitude *5 mm*. The triangular course of the stroke was used because of constant deformation velocity during each stroke. The frequency of the actuator movement was set from *1* to *4 Hz* to achieve velocity around the force-velocity knee. The strut force in time, as well as the input signal and the actuator position, are plotted in Fig. 73.

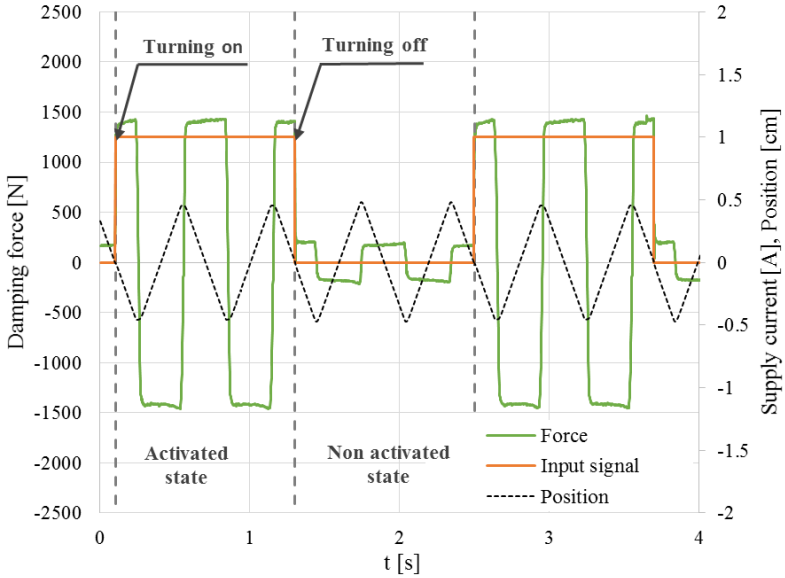

Fig. 73 Signals obtained during time response measurement

Detail of the strut force rise with actuator frequency *4 Hz* is shown in Fig. 74, from which the primary time response (63.2%) of MR strut in this configuration is around *4 ms*. An interesting effect, which was observed during all measurement is that the force did not increase during the short time just after the current switch. One of the possible explanations is that this delay is the time response of MR fluid [52].

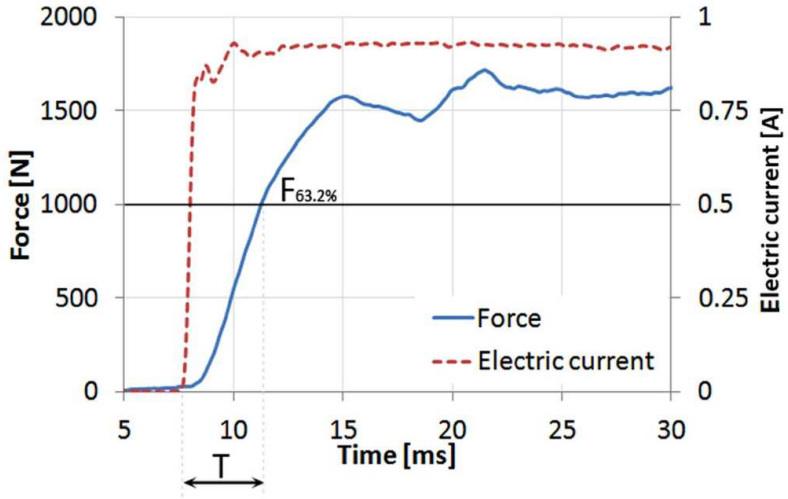

Fig. 74 Time response of experimental MR strut (Switching ON, $\dot{x} - \dot{x}_0$ = 100 mm/s)

Time response of MR strut was not constant. It depends on whether the damper switches from ON to OFF state or vice versa. Time response of switching ON is affected by the relative velocity $\dot{x} - \dot{x}_0$, see Fig. 75.

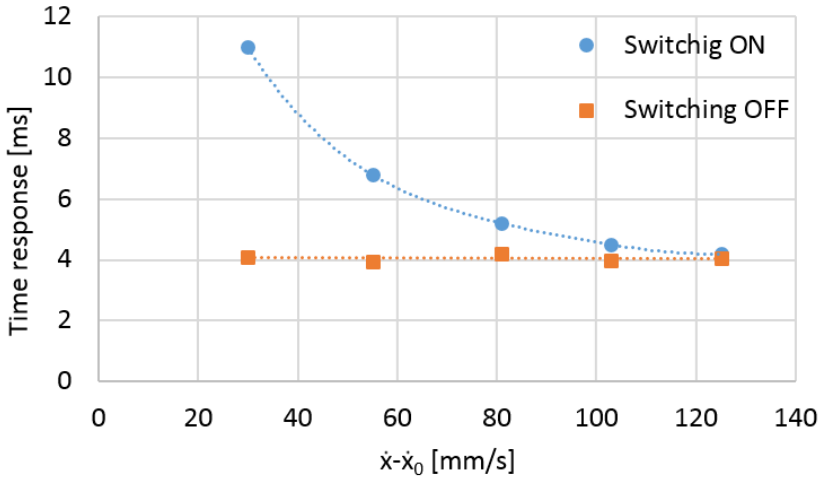

Fig. 75 Time response of the experimental MR strut for various relative velocities $\dot{x} - \dot{x}_0$

The measured values are, however, influenced by secondary stiffness k1. When the current to MR valve is turned on, the force which is needed for movement of the virtual rods of damper increases in very short time and till the moment when this force is crossed, the damper behaves as a stiff rod. The increase of force which is needed for unlocking the damper is caused by compression of stiffness k1, which means that this spring must be pressed by a certain distance. The time needed for compressing the spring influences the overall time response.

This effect is probably the cause of that the time response increase has a similar impact to the transmissibility as a decrease of the ratio between the primary and secondary stiffness of the strut, which was observed during simulations with a multi-body model of the single strut.

The primary stiffness of experimental MR strut *k* was measured at the same configuration of demonstrator as the force-velocity measurement were provided. However, the excitation differs a lot as well as the damping of the MR valve, because there was an effort to eliminate the damping forces. Therefore the part with the bypass orifice (pos. 3 in Fig. 64) was removed from the bellows unit. Thus, the bypass diameter grows from *Ø1.45 mm* to *Ø8 mm*. The frequency of the actuator movement was set as very low - *0.1 Hz* and the amplitude was *5 mm*.

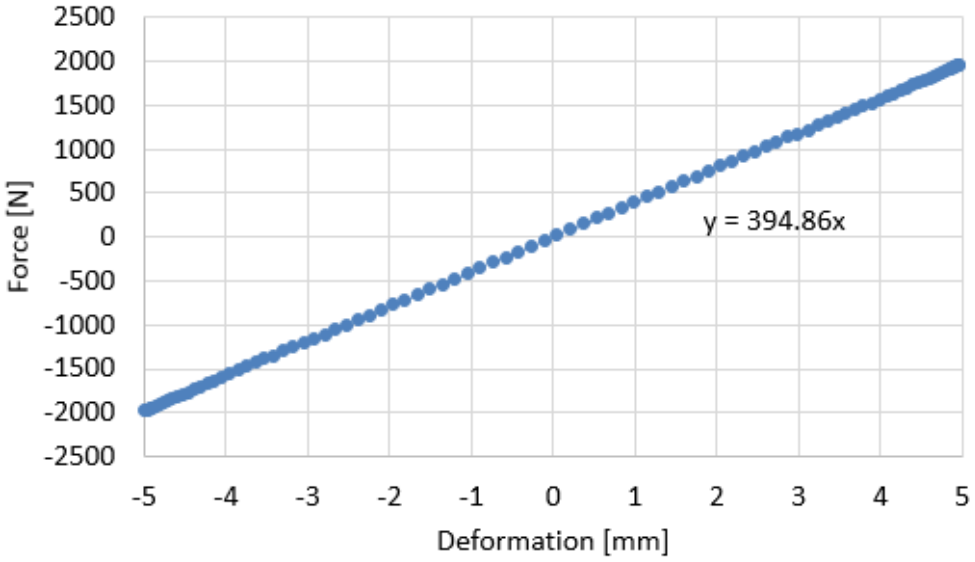

Fig. 76 The primary stiffness of the experimental strut

The secondary stiffness of experimental MR strut was because of the bellows model verification measured in two steps. The first step was to measure the pressure thrust of the bellows and the second step was to measure the pressure thrust stiffness of the MR valve and the pipelines. Comparison of these two measurements confirmed the assumption that the MR valve pressure stiffness is in an order higher than the pressure thrust stiffness of the bellows. Therefore, the simplification that the pressure thrust stiffness of bellows is identical to the secondary stiffness of the experimental MR strut has been introduced.

The Pressure thrust stiffness of bellows was conducted at hydraulic workshop press using sensors described above. The measured bellows with serial number *324125*, available in the product list of Witzenmann company [71] was filled by shock absorber oil *Paramo TL* 15 [73] sealed using the flanges and deaerated. The pressure sensor measured internal pressure to check that the maximal allowable pressure of the bellows is not exceeded.

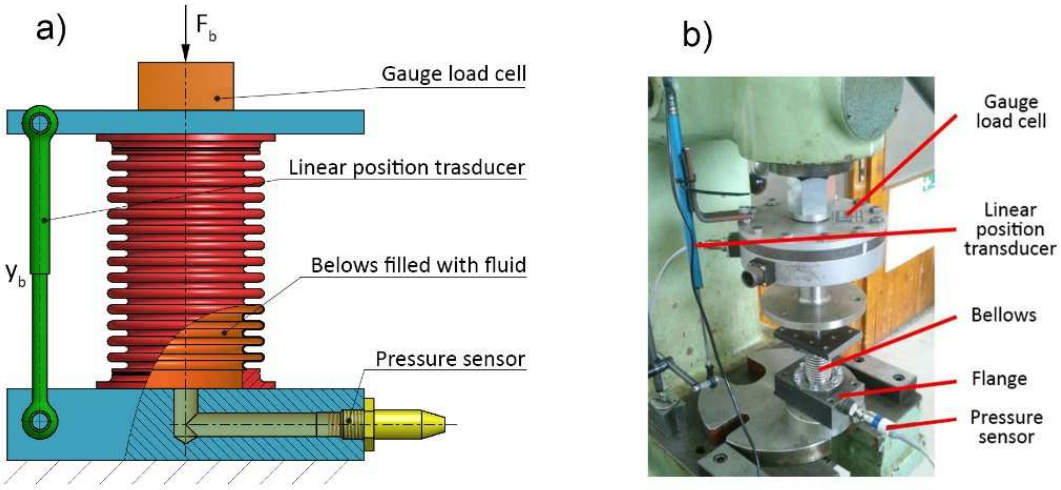

Fig. 77 Measurement of the pressure thrust stiffness of bellows

Force-deformation dependency was measured for two similar bellows and the measured data was linearly approximated by a line. Force increasing was not significant at the beginning of the compression. Visual check of the experiment revealed that the flanges are not parallel absolutely; thus, approximately *0.7 mm* of stroke was necessary to compensate the non-parallelism. These points were considered for the pressure thrust stiffness determination, in Fig. 78 these points are shown as less saturated. The values of both bellows pressure thrust stiffness were measured as very similar. The axial stiffness of the bellows resists the compression of the filled bellows. Thus the value of secondary stiffness of the strut is given by the sum of pressure thrust stiffness of both bellows, see Fig. 78, minus the sum of axial stiffness of both bellows; see Fig. 79.

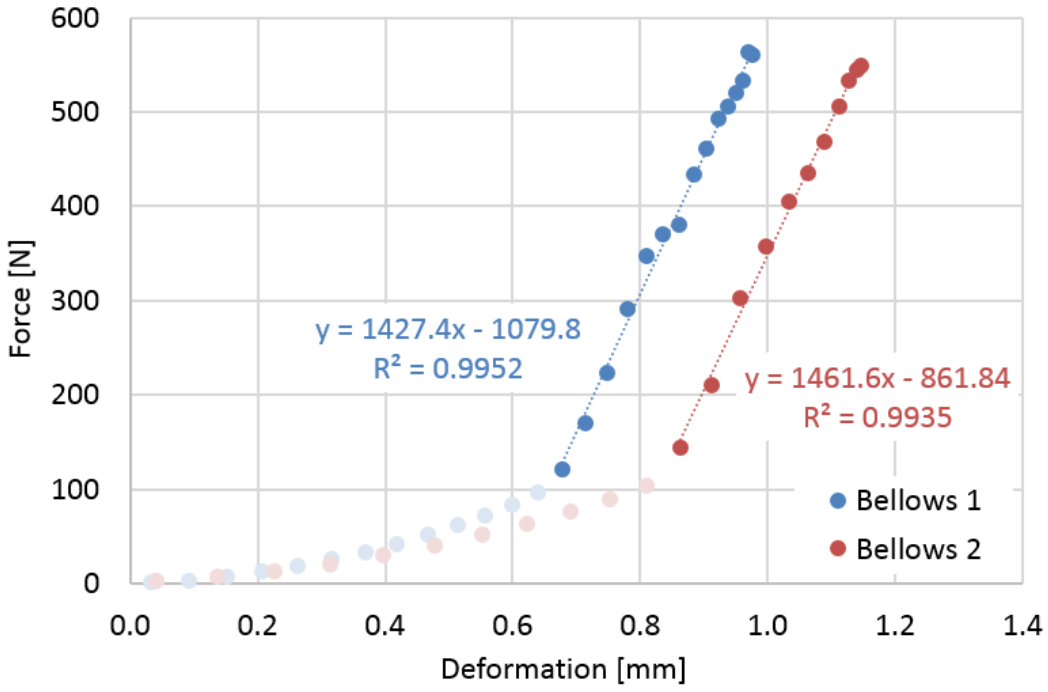

Fig. 78 Force-deformation dependency of the bellows filled with oil (pressure thrust stiffness)

The Axial stiffness of bellows was obtained by a slight modification of the experiment. This modification rests on the flanges removal; therefore, the oil drains and subsequently the air inside the bellows can drain too. After this only axial stiffness of bellows resits its deformation.

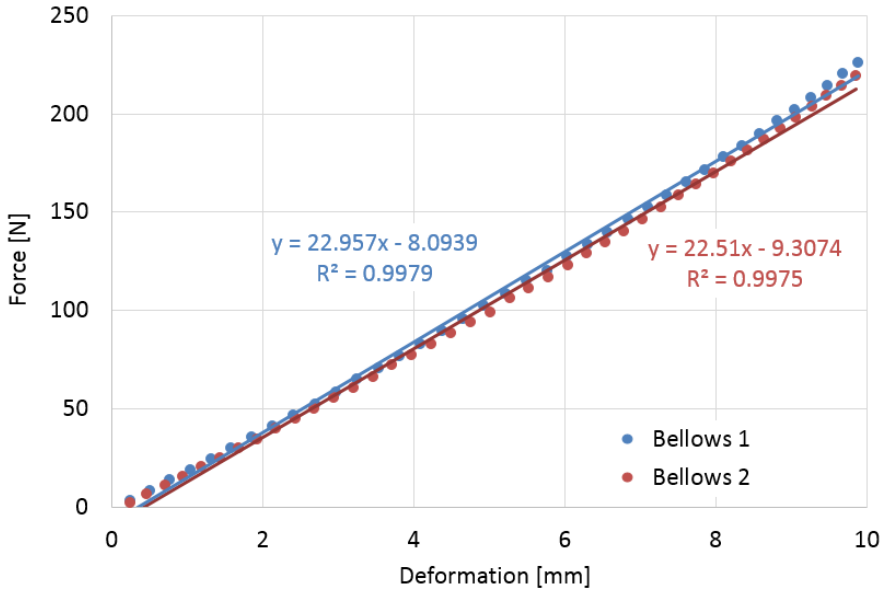

Fig. 79 Force-deformation dependency of empty bellows (axial stiffness)

The experimentally determined parameters of the strut in the tab. 5 were inserted into the model described in chap. 5.2.2 and the transfer ratio was simulated for three current in the coil of the MR valve. The simulation results are shown together with the measured results in Fig. 81.

tab. 5 Measured parameters of the demonstrator

Parameter	Symbol	Value	Unit
Sprung mass	m	95.6	[kg]
Primary stiffness	k	395	[N/mm]
Secondary stiffness	k_1	2844	[N/mm]
Damping in ON state (I = 1 A)	C_{ON}	non-linear	[Ns/mm]
Damping in OFF state (I = 0 A)	C_{OFF}	non-linear	[Ns/mm]
Time response	T	4	[ms]
Dynamic force range (maximum)	D	9	[-]

5.3.3 Transfer ratio of the demonstrator

Vibration isolation strut cannot be evaluated only by parameters, which are measured separately. Its behaviour must be verified in a complex vibration isolation system. That means to determine the transfer ratio - the magnitude of vibrations transmitted from the vibration source to the sprung mass. Therefore, the strut was inserted into the complex system (demonstrator) and the transfer ratio was measured by the following methods. The setup of measurement was similar to Fig. 68 but, the rod was removed.

Transfer ratio was determined by conversion of two accelerometers signals to the frequency spectrum. After that, the amplitude of the sprung mass acceleration $\ddot{x}_0$ was divided by the amplitude of actuator acceleration $\ddot{x}$ for given frequency. An important comment is that the settings of FFT analysis was the same for the both signal conversion: window type *Blackman, 2048 lines*, overlap *75%*, DC cut off *2 Hz*, cut-off frequency *1000 Hz*.

The excitation signal was a sweep sine function with a constant amplitude of the acceleration $\ddot{x}_0 = 1g = 9.81\ m \cdot s^{-2}$ in the frequency range *3 – 150 Hz*. The test takes *120 s*, the frequency rise was logarithmic. Sampling frequency was set to *2 kHz*.

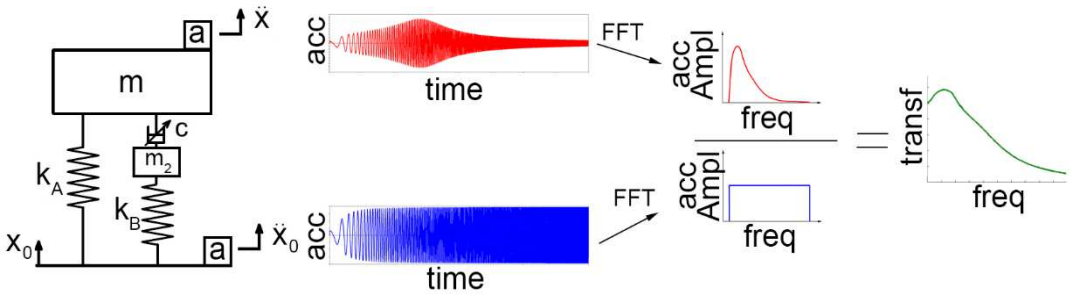

Fig. 80 Method of the transfer ratio determination

Passive mode of MR valve has been used for the most of tests. In Fig. 81 there are three of them for the currents *0 A*, *0.5 A* and *1 A* together with the simulation results (dashed lines).

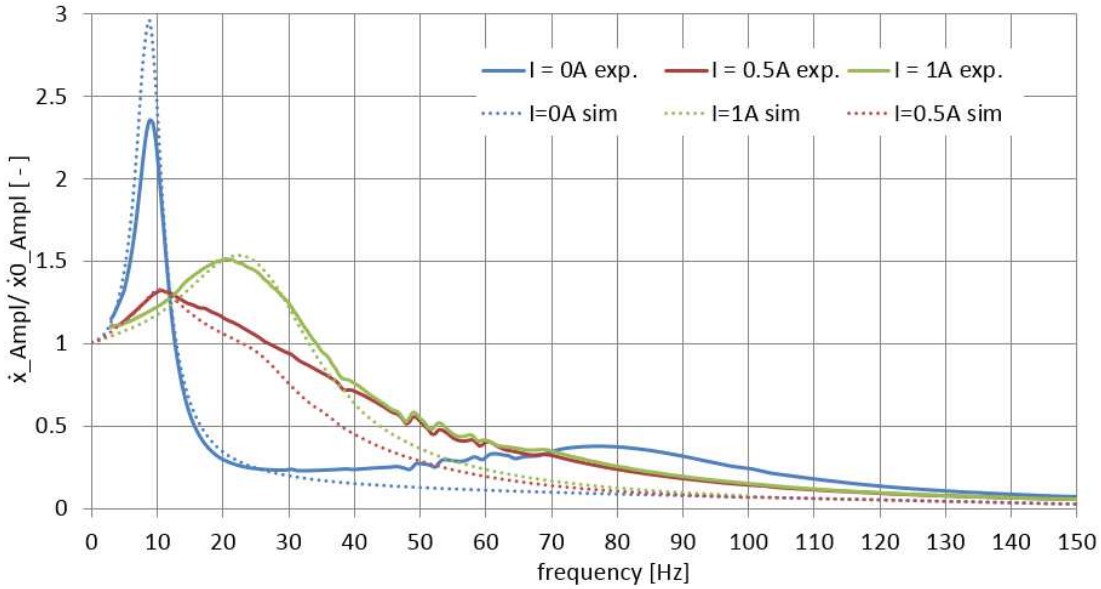

Fig. 81 Transfer ratio of a demonstrator with MR valve in passive mode

Simulated and measured data are not completely identical they differ primarily by a maximum of transfer ration with no current in the coil and the isolation properties at frequencies higher than *30 Hz*. This may be caused by passive losses of the real system (for example friction in linear bearings) which are not included in the model. However, there is one more difference, namely high damped peak around *80 Hz*, which disappears hand in hand with the current increase.

One of the possible causes of this transfer ratio increase is a so-called mass effect [29, 30[30]. That means the peak around *80 Hz* may be caused by oscillation of the fluid due to the elasticity of metal bellows (pressure thrust stiffness). This hypothesis was tested by additional measurements with various bellows or fluid, see chap. 5.3.4.

Semi-active control of the experimental strut have been investigated with the same excitation and the result was obtained by the same methods as in the case of passive mode. ON/OFF skyhook described by equation (7) was chosen as the control algorithm. However, the equation had to be modified for the real application: algorithm did not switch the damping force but the electric current in the coils of MR valve; an additional rule of the control was added to an acceleration noise elimination. The current in the coils valve coils was zero when the conditions (8) were not met.

$$(\dot{x} - \dot{x}_0) > 0.01 \wedge \dot{x} > 0.007 \quad \vee \quad (\dot{x} - \dot{x}_0) < -0.01 \wedge \dot{x} < -0.007 \tag{8}$$

$$\begin{cases} 1 & \dot{x} \cdot (\dot{x} - \dot{x}_1) \geq 0 \rightarrow I = 1\ A \\ 0 & \dot{x} \cdot (\dot{x} - \dot{x}_1) < 0 \rightarrow I = 0\ A \end{cases} \tag{9}$$

0 I = 0 A

Value of relative velocity *0.01 m/s* and *0.007 m/s* for the sprung mass velocity were obtained from several preliminary tests. Lower values of the velocities cause random switching of the current. Influence of the rule (8) is evident in Fig. 82, the relative velocity exceeds the value *0.01 m/s* sporadically for the excitation frequency *18 Hz* and higher. Therefore, there is a significant decrease in transfer ratio around the *18 Hz*.

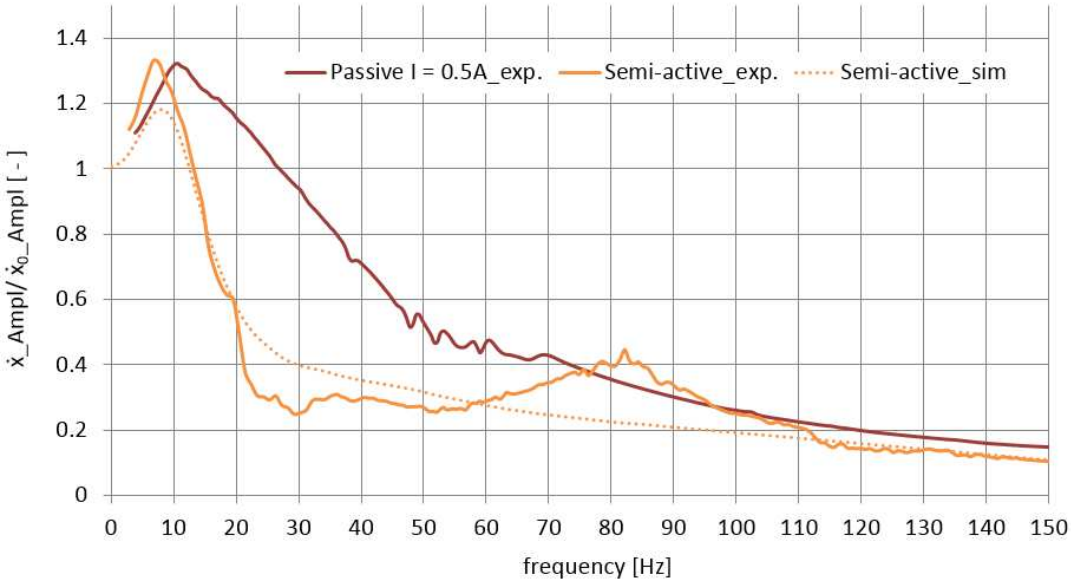

Fig. 82 Transfer ratio of a demonstrator with semi-active control of MR valve

The electric current in the MR valve coils was zero for the frequencies higher than *20 Hz* the resonance peak with a maximum around *80 Hz* appears in the semi-active controlled mode.

5.3.4 Conclusions of the experimental MR strut tests

Mass effect - a phenomenon described above may cause that the transfer ratio has a second resonance peak, in the case of Fig. 82 in the range between *50 – 110 Hz.* Hypothesis, that the peak is caused by a part of strut mass oscillation on a part of the strut stiffness was confirmed by re-measuring the transfer ratio with significantly stiffer bellows and a fluid with different density.

One of the possible causes of the peak is a movement of fluid mass m_f in the axial direction. The primary stiffness of strut *k* prevents this movement. However, in this case not only the axial deformation of bellows leads to the fluid flow. Internal volume changes of bellows may cause the flow too. Resistance against this deformation is given by the sum of both bellows pressure thrust stiffness k_1

Bellows can change its shape by two different ways: length, volume. Total deformation is given by the combination of both ways. Resistance against this can be calculated as the sum of two spring's stiffness in series and called total stiffness:

$$\frac{1}{k_t} = \frac{1}{k} + \frac{1}{k_1} \tag{10}$$

Then, the natural frequency of the fluid mass m_f is:

$$f = \frac{\sqrt{\frac{k_t}{m_f}}}{2 \cdot \pi} \tag{11}$$

The volume of the fluid in MR valve and the bellows unit was determined by the 3D model as *V = 0.23 l;* then, volume multiply by density ρ gives a fluid mass:

$$m_f = \rho \cdot V \tag{12}$$

Calculations and measurement were provided for 3 various configurations of the experimental MR strut, always with zero current in the coils of MR valve.

1) Single-layer bellows filled with MRF 132 DG

tab. 6 Parameters of the strut configuration

Parameter	Symbol	Value	Unit
The primary stiffness of the strut	k	395	[N/mm]
The secondary stiffness of the strut	k_1	2 844	[N/mm]
Density of the fluid	ρ	2.88	[kg/l]

Total stiffness:

$$\frac{1}{k_t} = \frac{1}{k} + \frac{1}{k_1} = \frac{1}{395\ 290} + \frac{1}{2\ 843\ 600}$$

$$k_r = 347\ 047\ N/m$$

Fluid mass:

$$m = \rho \cdot V = 0.23 \cdot 2.88$$
$$m = 0.6624\ kg$$

Natural frequency:

$$f = \frac{\sqrt{\frac{k_r}{m}}}{2 \cdot \pi} = \frac{\sqrt{\frac{347\ 047}{0.6624}}}{2 \cdot \pi} = 115.2\ Hz$$

2) Single-layer bellows filled with shock absorber oil

tab. 7 Parameters of the strut configuration

Parameter	Symbol	Value	Unit
The primary stiffness of the strut	k	395	[N/mm]
The secondary stiffness of the strut	k_1	2 844	[N/mm]
Density of the fluid	ρ	0.87	[kg/l]

Total stiffness:

$$\frac{1}{k_r} = \frac{1}{k} + \frac{1}{k_1} = \frac{1}{395\ 290} + \frac{1}{2\ 843\ 600}$$
$$k_r = 347\ 047\ N/m$$

Fluid mass:

$$m = \rho \cdot V = 0.23 \cdot 0.87$$
$$m = 0.2\ kg$$

Natural frequency:

$$f = \frac{\sqrt{\frac{k_r}{m}}}{2 \cdot \pi} = \frac{\sqrt{\frac{347\ 047}{0.2}}}{2 \cdot \pi} = 209.6\ Hz$$

3) Multi-layer bellows filled with MRF 122 EG

tab. 8 Parameters of the strut configuration

Parameter	Symbol	Value	Unit
The primary stiffness of the strut	k	495	[N/mm]
The secondary stiffness of the strut	k_1	11 113	[N/mm]
Density of the fluid	ρ	0.87	[kg/l]

Total stiffness:

$$\frac{1}{k_r} = \frac{1}{k_A} + \frac{1}{k_B} = \frac{1}{495\ 480} + \frac{1}{11\ 113\ 000}$$
$$k_r = 474\ 332\ N/m$$

Fluid mass:

$$m = \rho \cdot V = 0.23 \cdot 2.42$$
$$m = 0.5566\ kg$$

Natural frequency:

$$f = \frac{\sqrt{\frac{k_r}{m}}}{2 \cdot \pi} = \frac{\sqrt{\frac{474\,332}{0.5566}}}{2 \cdot \pi} = 146.9\ Hz$$

Measured transfer ratio for the strut configuration listed above are shown in Fig. 83.

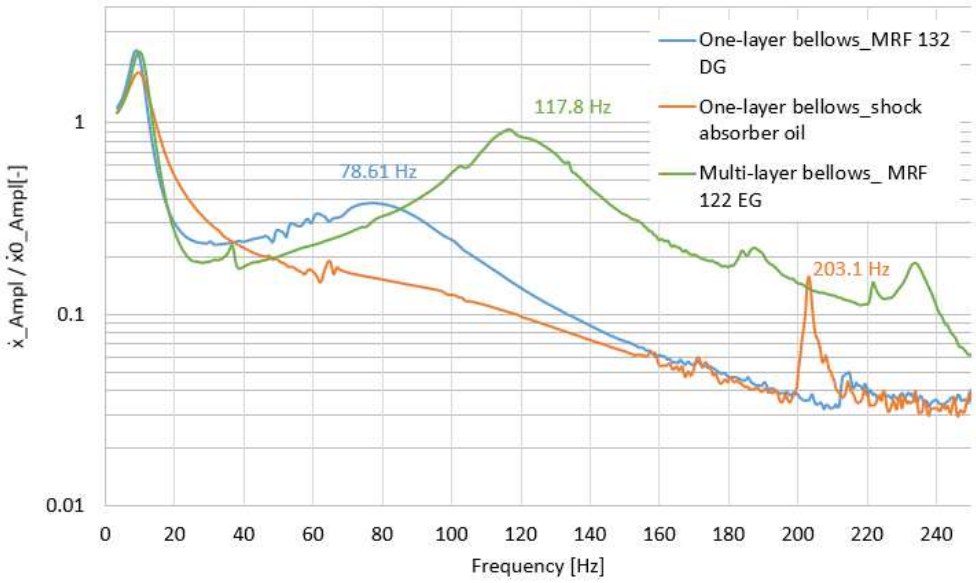

Fig. 83 Mass effect

tab. 9 Measured and calculated the modal frequency of the mass effect

Configuration	Counting [Hz]	Measurement [Hz]	Deviation [%]
Multi-layer, MRF 122 EG	146.9	117.8	25
Single-layer, MRF 132 DG	115.2	78.6	47
Single-layer, oil	209.6	203.1	3

Table 9 compares measured and calculated frequencies of modal shape, which may be caused by mass effect. This possible cause is supported by two facts: Firstly, an increase of damping causes disappearing of the phenomenon. Which is probably caused by the MRF yield stress increase in the gap and the fluid flow just by the bypass. This path exhibits much higher damping and the resonance peak is not reflected in the transfer ratio.

Secondly, a decrease of the fluid density results in a significant increase of the resonance frequency. However, the natural frequency calculated from a fluid mass (12) differs from the measured resonance frequency. It is possible, that the dynamic of the fluid is dominant in this phenomenon. That means not only the mass but, kinetic energy should be taken into account. The issue of this phenomenon goes beyond this thesis.

Minimization of the fluid mass in the final design of the strut will be required because of high resonance frequency and consequently a low maximal transfer as shown Fig. 83.

The closed bypass was initially considered as an advantageous version for semi-active control, especially because of high dynamic force range at low relative velocities. However, ON state of MR valve exhibits a much higher transfer ratio than expected, see, Fig. 84. Therefore, the strut version without bypass was rejected.

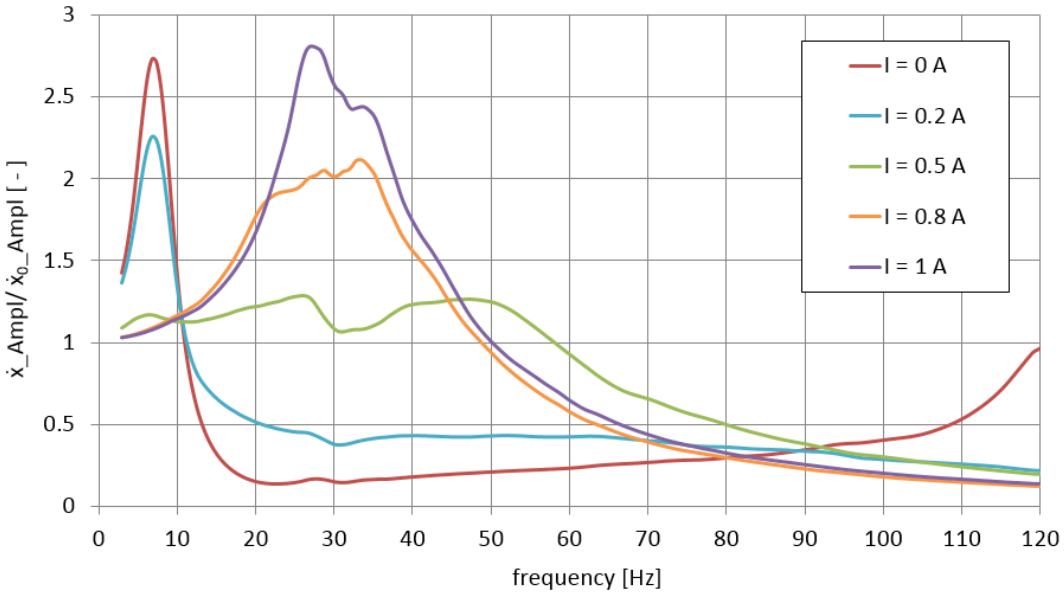

Fig. 84 Transfer ratio of a demonstrator with MR strut without bypass

This final design of strut will contain the bypass, which is described in chap. 5.4.3 (hydraulic part).

Ferrite cracks were found after the tests with semi-active control. Wider rings (pos. 2) *t = 13 mm* has usually just chipped edges but the thinner *t = 4 mm* ring cracked totally (pos. 3). Therefore, its reuse was excluded.

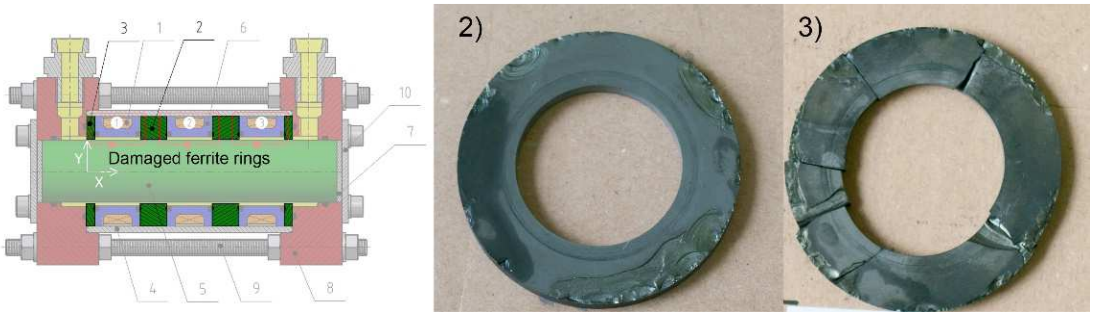

Fig. 85 Ferrite rings of MR valve after heavy loading

This accident initiated the search for another material, which guarantees a similar time response of MR valve, but which it is more resistant to mechanical loads. Moreover, it will be advantageous if the new material has higher saturation than the ferrite. Usually, materials with high electric resistivity (short time response) have low saturation, see Fig. 86. The high magnetic saturation exhibits materials Vacoflux 27 and 50. The second one has 4 times higher electrical resistivity than pure iron. Ferrite, with the saturation at around 0.5 T and almost infinity electrical resistance, is out of this diagram. The electrical resistivity of material can be increased by suitable shape.

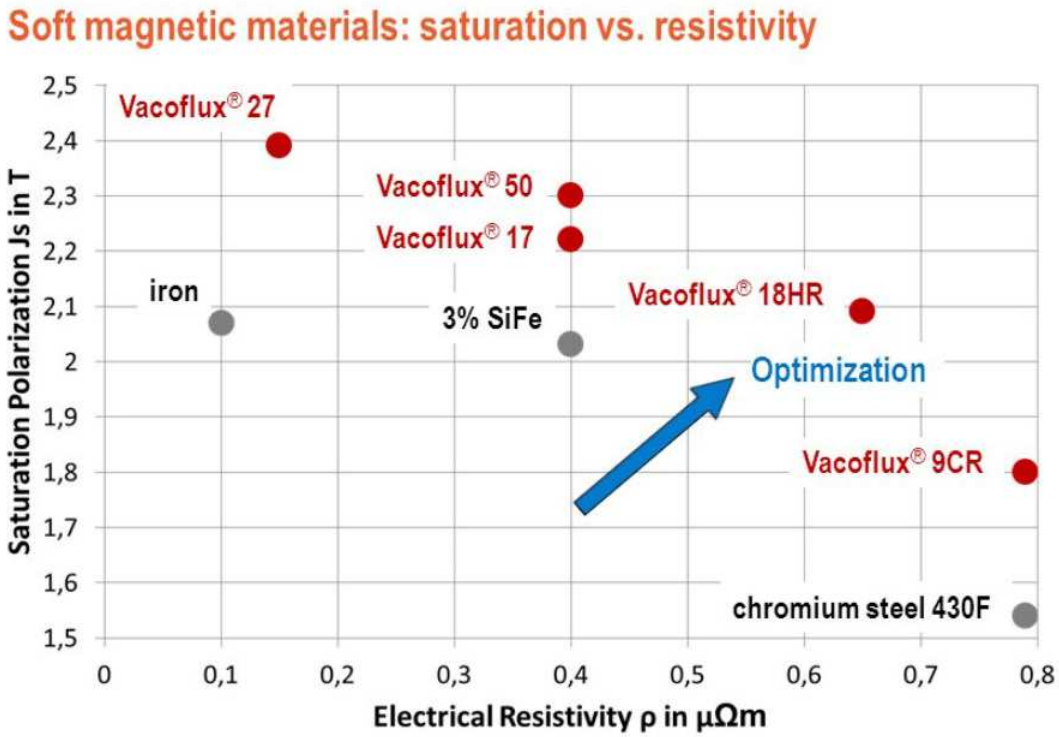

Fig. 86 Diagram electrical resistivity-saturation of several materials [74]

Therefore, research inspired by shape approach leading to the eddy currents elimination described in chap. 2.5.2 was started. Magnetic coil core made of a material with high saturation provided by isolation layers perpendicular to the eddy current flux could simultaneously meet both requirements of the effective magnetic circuit: high saturation and short time response. Production technologies which were tested: glueing (a), grooving by wire cutting EDM (b) 3D print using technology SLM (c) in Fig. 87.

Fig. 87 Shape approach of magnetic circuit time response decrease

Results of this research are currently prepared for an article. Therefore, they will not be presented in this thesis. The 3D print was chosen as the most convenient method for this thesis purpose. This method was patented in [75].

The magnetic circuit of the final strut will make of Vacoflux 50, by 3D print using method SLM. Magnetic circuit time response decrease by shape approach is described in chap. 5.4.3 (magnetic part).

5.4 Design of the MR strut for VIS of the launch vehicle

5.4

The MR strut design is a complex task consists of structural, hydraulic, magnetic etc. analysis. Each analysis was used to design dimensions of several parts. However, some analysis deals with the same parts. The analyses were carried out separately, but in several iterations because of the analysis interaction to a specific part. One of the components which affects other parts dimensions is metal bellows. Therefore, its design was provided preferably.

5.4.1 Metal bellows design

5.4.1

The bellows were loaded by pressure pulsation from the inside (MR fluid) and outside (gas of pneumatic spring). Moreover, it is load by axial deformation. The bellows were designed with respect to axial deformation and internal pressure caused by MR fluid. The pneumatic spring pressure was neglected in the phase of design. This configuration of a pair of bellows can be considered as a fluid vibration isolator according to Fig. 88.

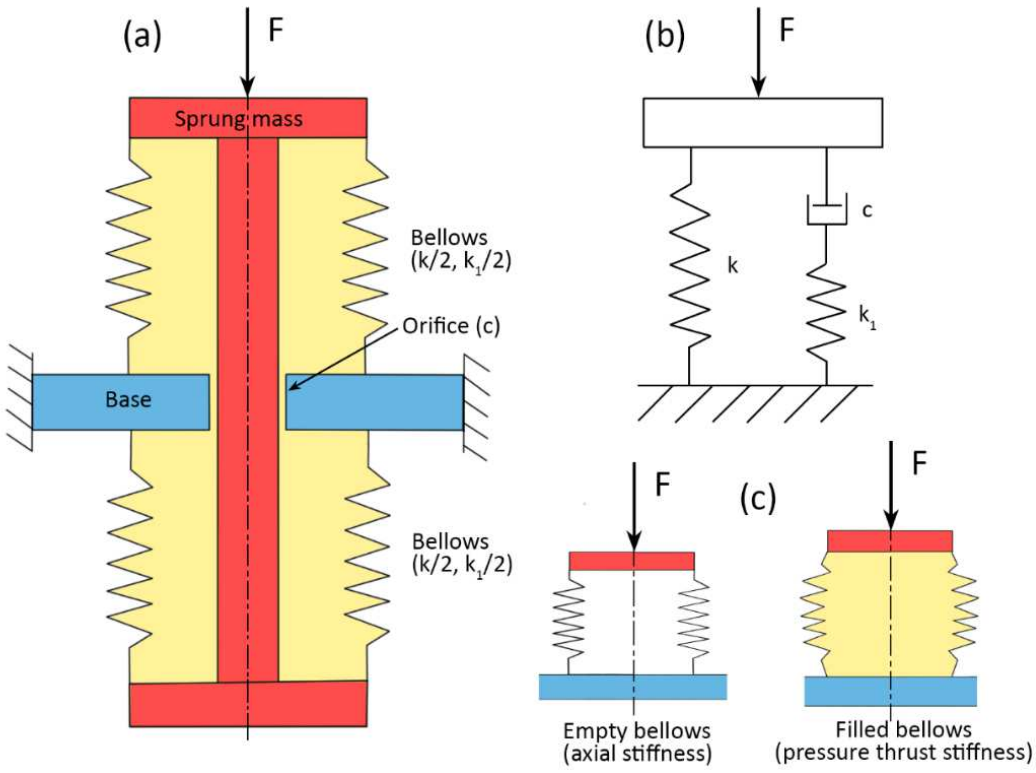

Fig. 88 Metal bellows as a part of the vibration isolator

The bellows are filled with a damping medium (MR fluid). The flow of the fluid through the orifice causes a damping c, see Fig. 88 a). The isolator works in two modes depends on the damping force: relatively small damping forces cause primarily axial deformation of the bellows, which is prevented by the axial stiffness of bellows *k*, shown in see Fig. 88 b). However, high damping forces (emerging for example by high piston velocity or by application of a magnetic field in orifice) cause an increase of damping medium pressure which results in a shape change of the bellows,

see Fig. 88 c). Shape change affects the length of bellows. Resistance against the deformation of bellows caused by shape change is called pressure thrust stiffness k_1. It can be determined by compression of bellows filled by a fluid and the axial force and axial deformation measurement.

Axial stiffness is commonly available in products list of bellows in contrast with the pressure thrust stiffness. Therefore, the FEM model was created to determination both stiffness based on the bellows geometry. Axial stiffness result is necessary for the model verification.

The model consists of two parts: wall (steel) and the fluid inside (oil). During the determination of axial stiffness, the fluid mesh is not considered in the model. The model was created in *ANSYS* software package as a plane model in *2D* using the rotational symmetry. The shell elements could not be used as in Thakkar thesis [41], because of the fluid and the wall interacting. But, there is also mentioned the second approach – with solid elements with a note that the results of both methods do not differ significantly. Thus, the *SOLID 182* elements were used for the wall and *HSFLD 241* elements for fluid.

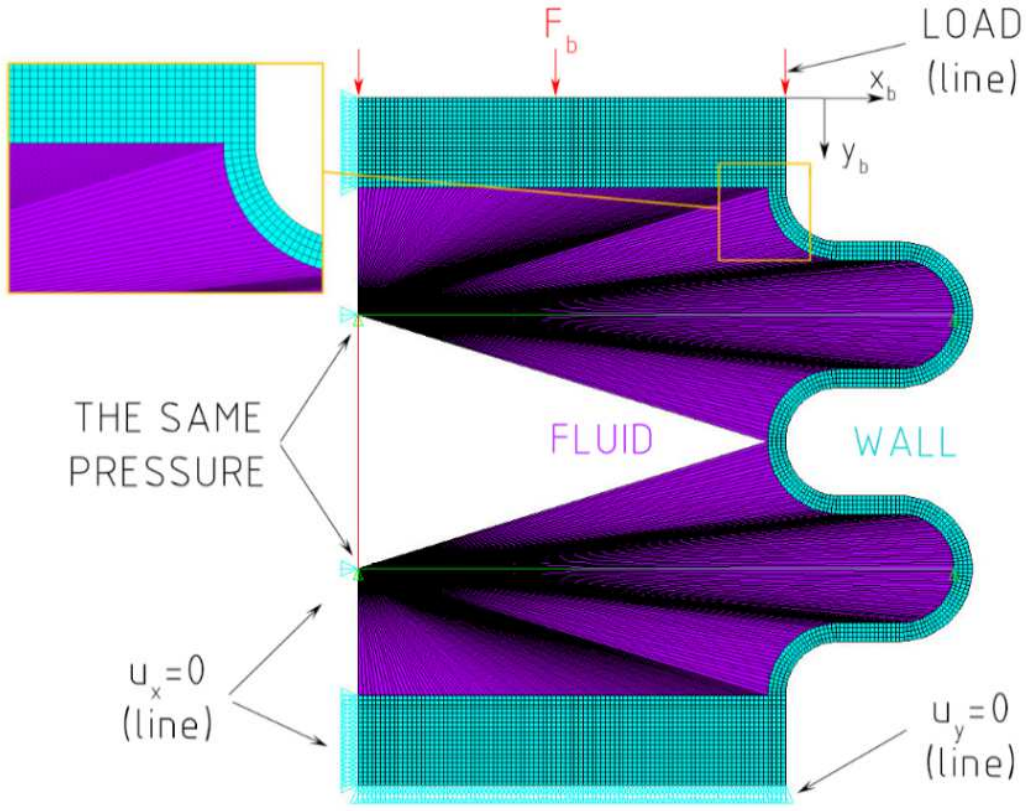

Fig. 89 FEM model of bellows

Load force is applied by the pressure on the top line, which corresponds to the force F_b. The displacement of the top line y_b is used for the stiffness calculation. The bottom line cannot move in vertical direction *Y*. Nodes located on Y axis cannot move in the horizontal direction *X*. There are several points (depends on a number of corrugations) with the same pressure in the mesh of fluid. It ensures identical pressure in the fluid, as shown in Fig. 89. The material used in the model are summarized in the tab. 10.

tab. 10 The materials used in FEM model

The material of bellows			
Stainless steel		1.4571	
Modulus of elasticity	E	200 000	MPa
Poisson ratio	μ	0.28	
Yield stress after forming	Re	500	MPa
The material of the filling			
Shock absorber oil		Paramo TL 15	
Volume modulus of elasticity	K	2 200	MPa
Density	ρ	885	kg/m^3

The FEM model was verified by measurement of bellows which was used in the experimental strut. The bellows *324125* is listed in the datasheet of Witzenmann [71]. Its dimensions are in the tab. 11.

The parameters are listed in the tab. 11 and shown on the right side of Fig. 90. The wall thickness is considered one of the most important parameters in axial and pressure thrust determination. The thickness of the sheet which is the bellows made of is *0.25 mm* by the product list. However, forming of bellows reduces the thickness of some parts of the bellows wall [40]. Value of wall thickness *0.22 mm* used in the model was obtained by a lot of experiment provided by the bellows manufacturer. The manufacturer also sends us the results of axial stiffness analytical counting.

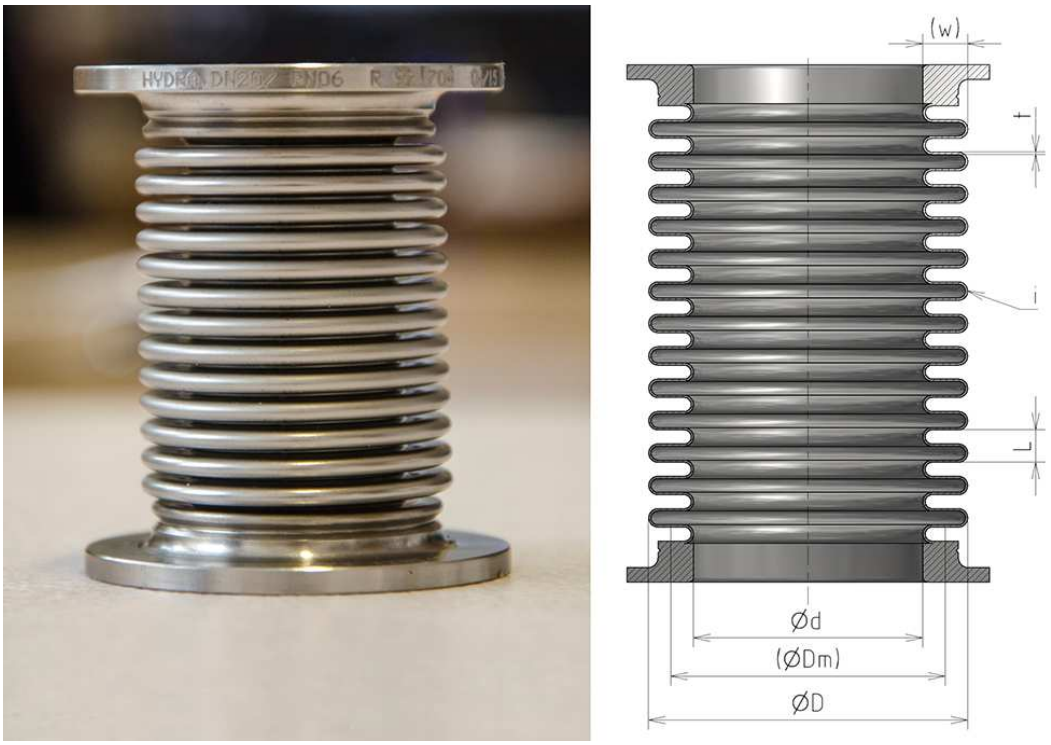

Fig. 90 The bellows used in the experimental MR strut

tab. 11 Dimensions of the bellows used in the experimental strut

Parameter	Symbol	Value	Unit
Outer diameter	D	36.5	[mm]
Inner diameter	d	23.6	[mm]
Mean diameter	Dm=(d+D)/2	30.05	[mm]
Corrugation width	w=(D-d)/2	6.45	[mm]
Corrugation length	L	3.2	[mm]
Wall thickness	t	0.22	[mm]
Number of corrugations	i	13	[-]

The same force $F_b = 300\ N$ was used to compare the behaviour of empty bellows, see Fig. 91 a) with the same bellows filled by the oil b). The membrane stress is plotted in this figure. The filling affected the bellows stiffness but also the shape of corrugations (waves) deformation.

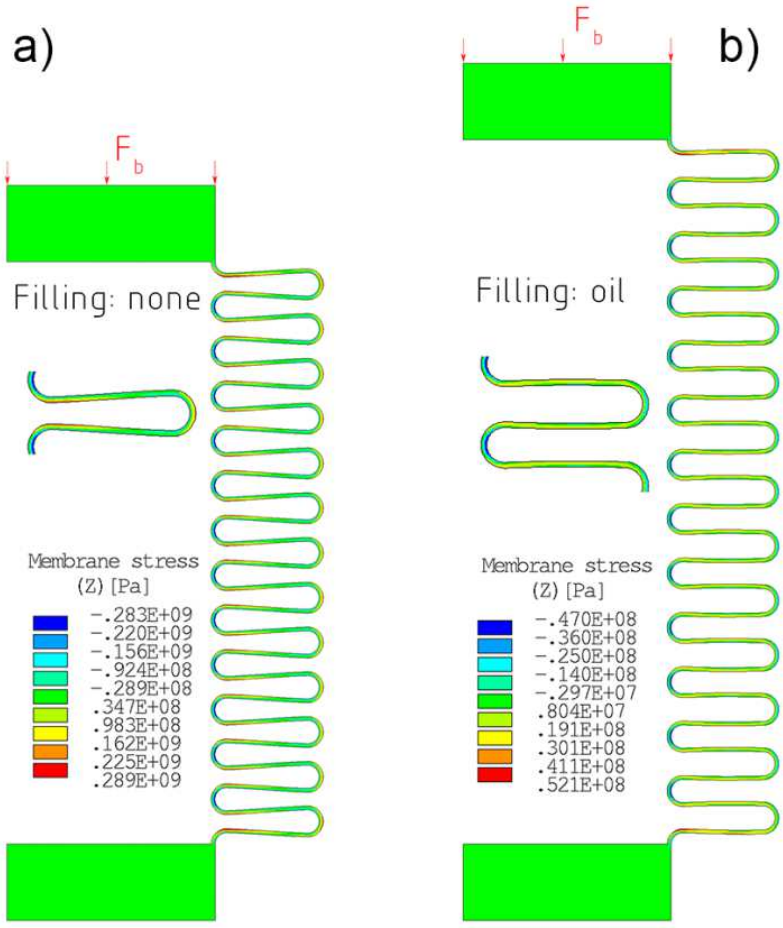

Fig. 91 Comparison of membrane stress in the wall of bellows which is empty a) or filled by oil b)

The compression loading was compared with the tensile loading. The results were almost identical; however, only the compression was considered to the stiffness determination to achieve the same method compare with the experiment. The points obtained by tensile loading are less saturated in Fig. 92.

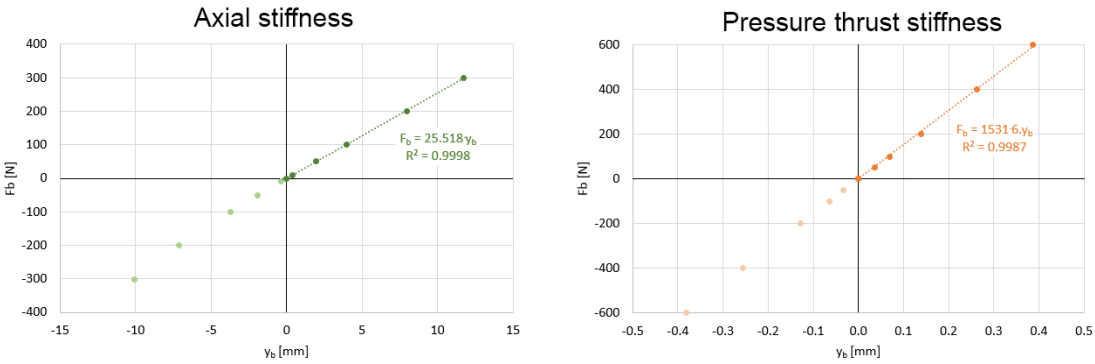

Fig. 92 Axial and pressure thrust stiffness of bellows 324125 (FEA)

The FEM result of axial stiffness was compared with the measurement, counting carried out by the manufacturer and also with the value which is listed in the product list. The pressure thrust stiffness was compared just with the measurement described in chap. 5.3.2.

tab. 12 Bellows stiffness comparison determined by various methods

Procedure	Stiffness	Symbol	Value [N/mm]	Deviation [%]
Product list [71]	Axial	k_L	22.3	12.6
Manufacturer calc.	Axial	k_C	29.5	15.6
FEM model	Axial	k_F	25.52	ref. value
Measurement	Axial	k_M	22.7	11
FEM model	Press. th.	k_{1F}	1531.6	ref. value
Measurement	Press. th.	k_{1M}	1444.5	5.7

Sensitivity analysis of each parameter listed in the tab. 11 to the axial and pressure thrust stiffness was carried out after the mode verification. The analysis uses the geometry of the bellows *324125*, just one dimension differs the tab. 11 to *90*, *95*, *105* a *110 %* of its initial value for each set of simulations. The parameters affect axial Fig. 93 a) and pressure thrust stiffness Fig. 93 b).

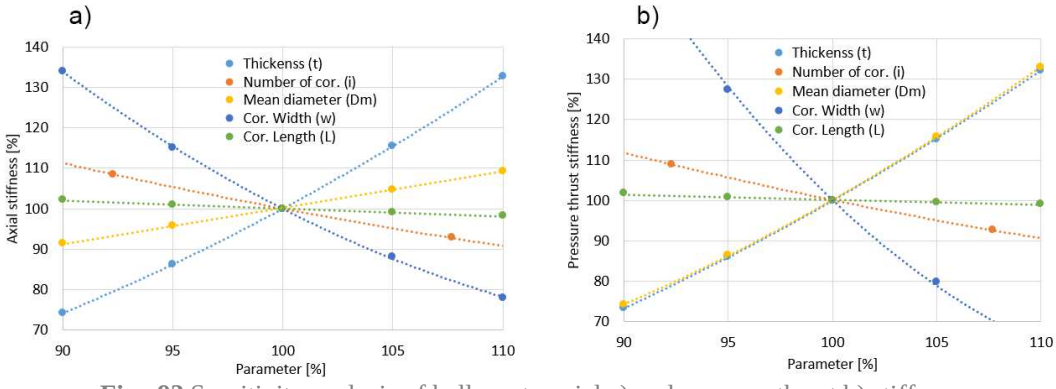

Fig. 93 Sensitivity analysis of bellows to axial a) and pressure thrust b) stiffness

Comparison of both diagrams in Fig. 93 shows that some parameters have the same impact on both stiffnesses: *t, i, L;* while, two of them: D_m, *w* affected axial and pressure thrust stiffness differently, see Fig. 94. The conclusion of the sensitivity analysis is that the ratio between the pressure thrust and axial stiffness can be slightly

modified by the geometry of the bellows. That may affect the ratio *N* between primary and secondary stiffness of the strut.

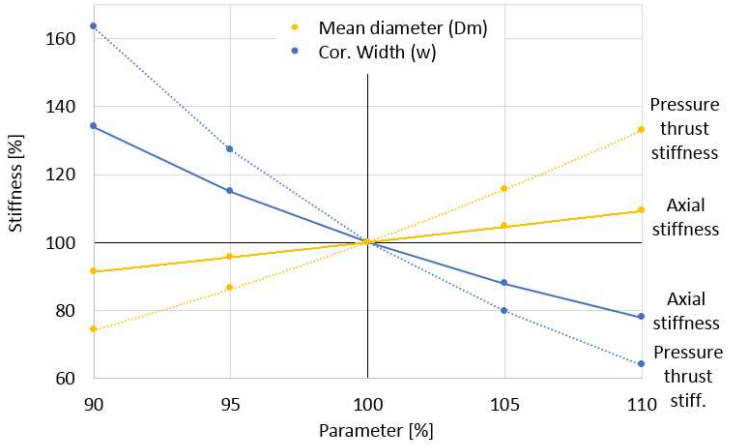

Fig. 94 Parameters with different impact to axial and pressure thrust stiffness

Multi-layer bellows (part number *324325*) which were used for the mass effect measurements were also analysed by FEM. However, complicated interaction between the multi-layer bellows wall results in simplification (13), which determines the stiffness of multi-layer bellows k_{il} by multiplication of the stiffness of single-layer bellows k_L with the number of layers *i*. This hypothesis was established based on a comparison of values of multi-layered bellows listed in the product list. When the dimensions of multi-layered (for example 5 layers) bellows are similar to the dimensions of single-layered, the stiffness is always (for the example approximately fifth time) higher than the single-layer bellows stiffness.

$$k_{Li} = k_L \cdot i \tag{13}$$

Sensitivity analysis showed that the wall thickness has the same effect on the axial and pressure thrust stiffness. Therefore, the pressure thrust stiffness estimation by the equation (13) could be considered as valid. This method was verified by measurement, the result of FEA and measurement are compared in the tab. 13.

tab. 13 Verification of multi-layer bellows stiffness estimation

Procedure	Stiffness	Symbol	Value [N/mm]	Deviation [%]
Product list [71]	Axial	k_{L3}	66.2	13.6
FEM model	Axial	k_{F3}	25.52*3=76.6	ref. value
Measurement	Axial	k_{M3}	83.75	9.3
FEM model	Press. th.	k_{1F3}	1532*3=4596	ref. value
Measurement	Press. th.	k_{1M3}	5557	20.9

The deviation between the estimated and measured values is approximately *20*. Choose of bellows of the MR strut for the VIS of the launch vehicle was discussed with the bellows manufacturer which provides a value of wall thickness usable for the calculation, see tab 14.

tab. 14 Parameters the bellows used in the MR strut for VIS of the launch vehicle

Parameter	Symbol	Value	Unit
Outer diameter	D	66	[mm]
Inner diameter	d	47.4	[mm]
Mean diameter	Dm=(d+D)/2	56.7	[mm]
Corrugation width	w=(D-d)/2	9.3	[mm]
Corrugation length	L	6.7	[mm]
Wall thickness after forming	t	0.27	[mm]
Number of corrugations	i	11	[-]
Number of layers	n	5	[-]
Axial stiffness	k_b	298	[N/mm]
Pressure thrust stiffness	k_{1b}	23470	[N/mm]

Axial and pressure thrust stiffness was determined using the methodology described above. Ratio *N* between the primary and secondary stiffness was chosen as *N = 50*. Selected bellows and proposed axial stiffness of strut gives stiffness ratio:

$$N = \frac{k_B}{k_A} = \frac{k_{1b} * 2}{k_A} = \frac{23\,470 * 2}{1\,230} = 38.2 \tag{14}$$

Considering that the FEA estimation of pressure thrust stiffness was *20%* lower than the measurement, the real ratio N should be higher. Anyway, change of *N* from 50 to 38 will not have a significant impact on VIS behaviour, see chap. 5.2.1 and 5.2.2. However, the geometry modification of the chosen bellows that means custom made of the bellows should increase the ratio *N* to the required value.

5.4.2 Pneumatic spring design

Pneumatic spring is designed for a load of strut built in VIS with payload mass *1500 kg*. This load causes the equal pressure above and under piston of the pneumatic strut. The angle between the strut axis and base plane *SA*, in Fig. 95 was determined during quasi-static load *1g* by the multi-body model of VIS.

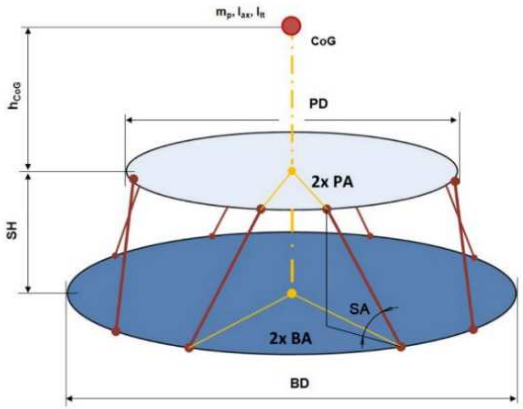

Fig. 95 Strut angles in VIS

Both chambers dimensions necessary for the design are shown in Fig. 96 and listed in tab 15 and 16.

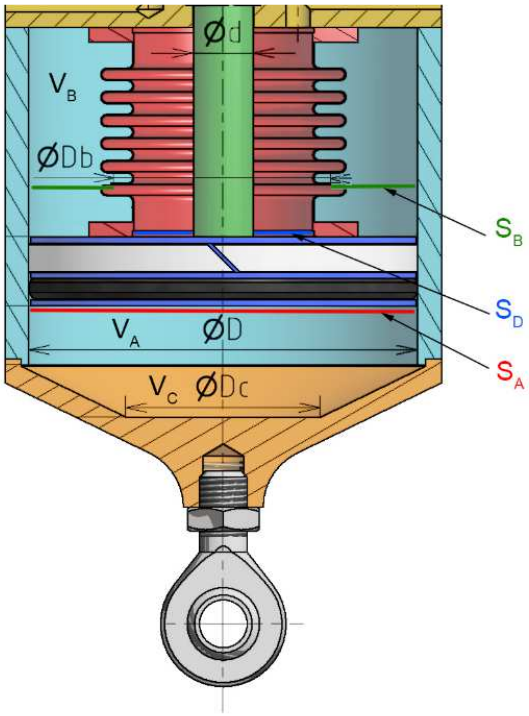

Fig. 96 Pneumatic spring scheme

The gravitational force of payload *m=1500kg* and *1g* load to single strut axis:

$$F_1 = \frac{m \cdot g}{i \cdot \sin(\alpha)} = \frac{1500 \cdot 9.81}{8 \cdot \sin(62)} = 2083N \tag{15}$$

Static pressure in pneumatic spring (no bellows compression, *1g* load):

$$p_S = \frac{F_1}{S_A - S_B} = \frac{2083}{10386 - 7862} = 0.825\ MPa \tag{16}$$

Static pressure increase allows adjusting steady state that means payload mass which causes equal pressure in both chambers of pneumatic spring with *1g* loading.

Maximum pressure in pneumatic spring (maximal compression, *VA = 0*):

$$p_{Smax} = p_1 \cdot \left(\frac{V_A + V_C}{V_C}\right)^{\kappa} = 0.737 \cdot \left(\frac{253683 + 97880}{97880}\right)^{1,4} = 4.94\ MPa \tag{17}$$

tab. 15 Dimensions of pneumatic spring

Dimension/Parameter	Symbol	Value	Unit
Pneumatic spring piston diameter	D	110	[mm]
Mean diameter of bellows	Db	57.6	[mm]
Cone diameter	Dc	65	[mm]
Bellows length	hb	88	[mm]
Cylinder length	h	15	[mm]

Cone length	hc	15	[mm]

tab. 16 Volumes and areas importat to pneumatic spring calculations

Dimension/Parameter	Symbol	Value	Unit
Area of pneumatic chamber under piston	SA	10 386	[mm^2]
Area of pneumatic chamber above piston	SB	7 862	[mm^2]
Area of damping chamber	SD	2 210	[mm^2]
Volume of gas under piston (cylinder)	VA	247 158	[mm^3]
Volume of gas under piston (cone)	VC	91 354	[mm^3]
Volume of gas above piston	VB	691 849	[mm^3]

The non-linear dependence of force F_p and deformation Y (perpendicular direction to the piston movement) is described by the equation:

$$F_p(Y) = p.\left(S_A.\left(\frac{V_A}{V_A - S_A \cdot Y}\right)^{\kappa} - S_B.\left(\frac{V_B}{V_B + S_B \cdot Y}\right)^{\kappa}\right) \tag{18}$$

Stiffness point estimate in steady state $Y = 0$ can be obtained by derivation of equation (18):

$$Kp(Y) = \frac{d}{dY}Fp(Y) = \frac{{S_A}^2 \cdot V_A \cdot \kappa \left(\frac{V_A}{V_A - S_A \cdot Y}\right)^{\kappa-1}}{(V_A - S_A \cdot Y)^2} - \frac{{S_B}^2 \cdot V_B \cdot \kappa \left(\frac{V_B}{V_B - S_B \cdot Y}\right)^{\kappa-1}}{(V_B - S_B \cdot Y)^2} \tag{19}$$

$$Kp(0) = 632{,}7N/mm$$

Strut spring force consists of the pneumatic spring force and the bellows force, the second one is given by the equation:

$$Fb(Y) = k_b \cdot Y \tag{20}$$

The strut force-deformation dependency is plotted in Fig. 97. The strut stiffness is non-linear due to the pneumatic spring. The strut stiffness in steady state is:

$$k_A = K_p(0) + 2 \cdot k_b = 632.7 + \ 2 \cdot 298 = 1228.7 \tag{21}$$

This value is almost identical to the value used in the model. However, the strut force-deformation dependency has a progressive course of in compression part of the diagram and an almost linear course in tension. This feature is useful with respect to the flight direction (quasi-static acceleration). Progressive course of the strut force-deformation dependency allows decreasing of the maximal stroke of strut form *±20 mm* listed in onto *±15 mm*. This stroke reduction helps to decrease the weight of the strut.

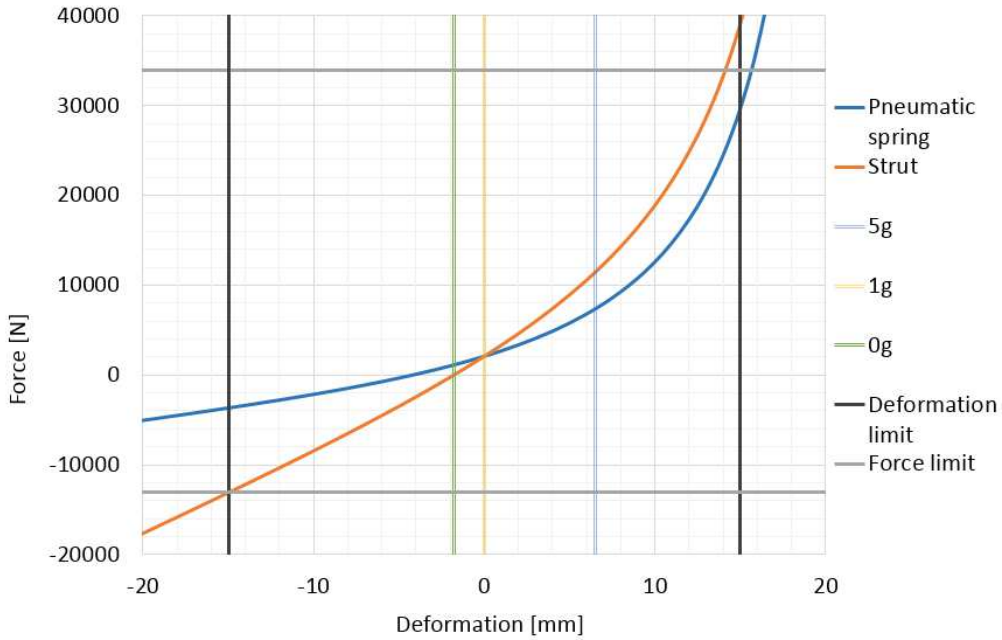

Fig. 97 Force-deformation dependency of the strut and its pneumatic spring

5.4.3 MR valve design

MR valve design consisted of two models which are interconnected by several parameters, especially dimensions of the MR valve. The first one (hydraulic) is an analytical model of MR valve pressure drop causes by MR fluid flow through it. The second one (magnetic) is a FEM of the magnetic circuit which determines the yield stress of MR fluid in the gap.

Inputs for the pressure drop calculation caused by the MR fluid flow through the MR valve are: yield stress of MR fluid in the gap (ON state), hydraulic diameter of bellows and required force-velocity dependency. The output of the model are dimensions of channels where the fluid flow.

Dimensions designed by the hydraulic model are subsequently used as inputs of a magnetic circuit model together with another input: the intensity of the magnetic field in the gap. The FEM of the magnetic circuit allows to the dimensioned coil, pole pieces, coil core etc. Moreover, the model was used for transient analysis that means to determine time dependency of magnetic field intensity in the gap after a step change of input current in the coil. This is necessary for the MR valve time response estimation.

tab. 17 Boundary conditions of MR valve design

Dimension/Parameter	Symbol	Value	Unit
Piston rod diameter	d	20	[mm]
Mean diameter of bellows	Db	57.6	[mm]
Effective area of "piston" $A_p = \frac{\pi(D_b{}^2 - d^2)}{4}$	A_p	2291.6	[mm^2]
The yield stress of MRF	Ty	32	kPa
Required intensity of the magnetic field	H	250	kA/m
Saturation of Vacoflux 50	B_{max}	2.3	T

Hydraulic part

An analytical model of MR fluid flow through gap or bypass, see Fig. 98 was created using the equation mentioned in [49]. The model determines pressure drop during the fluid flow, thus also damping force-velocity dependency.

The MR fluid flows via two paths: through the gap where the magnetic field can change of the fluid yield stress or through bypass orifice. Total flow rate Q has to be split into two parts $Q1$, $Q2$. The ratio between $Q1$ and $Q2$ depends on the intensity of the magnetic field in the gap and on the dimensions of channels. In the model, there is a rule that when the shear stress τ in the MR fluid is lower than the yield stress of MR fluid τ_f, then the $Q1$ is zero. Mathematically:

$$\begin{aligned} \tau \leq \tau_f \;&\rightarrow\; Q1 = 0 \;\rightarrow\; Q = Q2 \\ \tau > \tau_f \;&\rightarrow\; Q1 \neq 0 \;\rightarrow\; Q = Q1 + Q2 \end{aligned} \tag{22}$$

Shear stress during the fluid flow through the gap:

$$\tau = \frac{\Delta p \cdot h}{2 \cdot L} \tag{23}$$

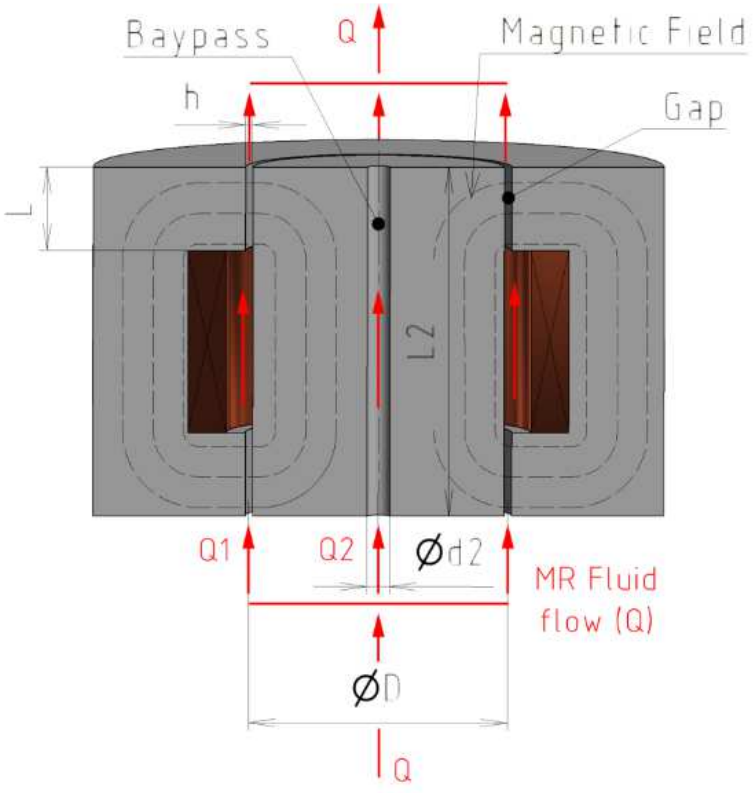

Fig. 98 MR valve hydraulic scheme

Influence of individual parameters from the tab. 18 to the MR valve force-velocity dependency is shown in Fig. 99. The slope of the curve before the knee can be modified by the dimensions of the bypass orifice, thus *d2*, *L2*. The knee position is influenced by the gap dimensions *h* and *L* and the MR fluid yield stress τ_y.

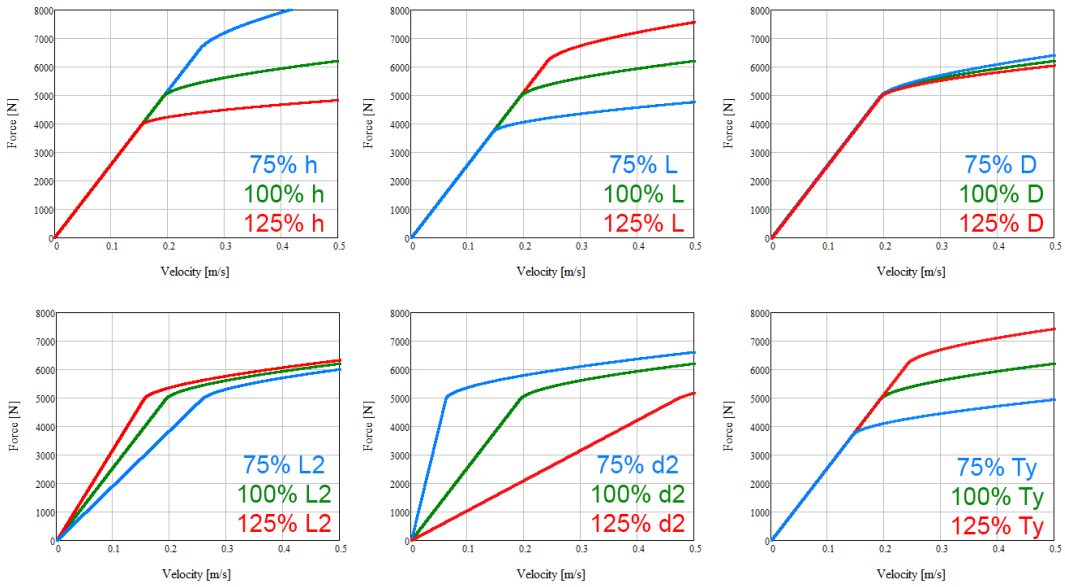

Fig. 99 Influence of MR valve parameters to force-velocity dependency

tab. 18 A combination of MR valve dimension meeting required F-v dependency

Dimension/Parameter	Symbol	Value	Unit
Gap thickness	h	0.65	[mm]
Gap length	L	22	[mm]
Gap mean diameter	D	42.65	[mm]
Bypass length	L2	40	[mm]
Bypass diameter	d2	1.95	[mm]

Dimensions mentioned in the tab. 18 ensures force-velocity dependencies in Fig. 100. The blue curve represents ON state, the orange one is for OFF state.

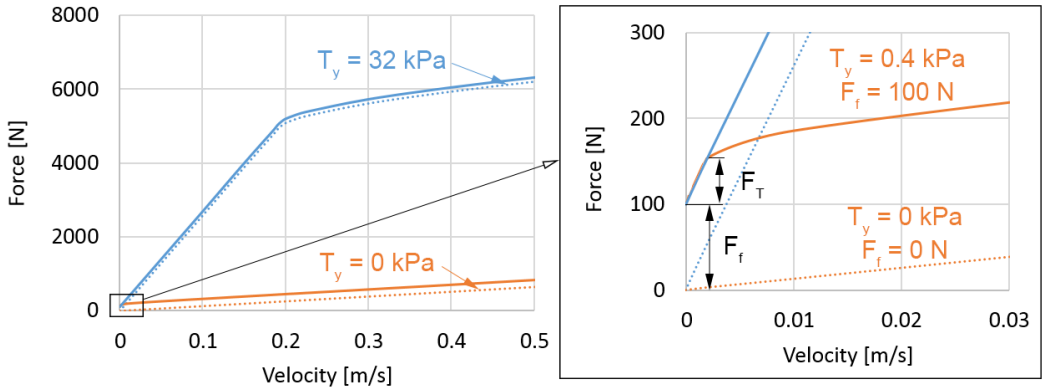

Fig. 100 The simulated F-v dependency of MR valve

The dynamic range of the strut with this MR damper will decrease by the friction of seals [76]. In the case of the MR strut, it will be the seal of pneumatic spring and guiding, which was estimated at *100 N*. Moreover, magnetic remanence of magnetic circuit material will cause a little yield stress even in the case of OFF state. The magnetic flux density in the gap of the magnetic circuit made of Vacoflux 50 was

measured *15 mT* (measured on air – no MR fluid in the gap), this magnetic flux density causes *0.4 kPa* yield stress of *MRF 122 EG* [77]. Comparison of theoretical and predicted dynamic force range of MR strut for VIS of the launch vehicle is in Fig. 101.

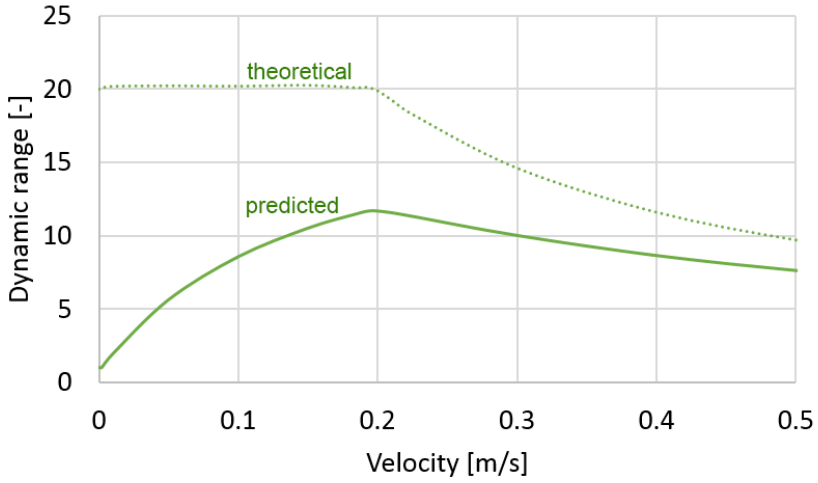

Fig. 101 MR strut dynamic force range

Magnetic part

An important aspect for magnetic simulation is accurate knowledge of magnetic properties of the material used in the model. B-H curves of the magnetic circuit and MR fluid was determined experimentally. Measured data was inserted into the model using interpolation. The other materials used in the model was taken from libraries of the model software package – *ANSYS ELECTRONICS 2017* or from the product list. Magnetic properties of the materials which were used in the model are summarized in the tab 19.

tab. 19 Magnetic properties of materials used in the model

Part	Material	Relative permeability [-]	Bulk conductivity [S/m]
Coil core, Pole piece	Vacoflux 50	B-H curve	2 490 000
MR fluid	MRF 122 EG	B-H curve	0
Coil	Cooper	0.999991	58 000 000
Coil skeleton, Grooves filling	Polyamide	1	0
The mode environment	vacuum	1	0

The electric conductivity of MR fluid depends on the concentration of iron particles, the intensity of the magnetic field, etc. However, the conductivity varies only in the order of S/m [78]; therefore, the electrical conductivity of MR fluid in the model considered zero.

Preliminary design of magnetic circuit was provided by a magnetostatic model with rotational symmetry. The intensity of magnetic field in the gap *250 kA/m* has to be achieved while no part of the magnetic circuit would be saturated, that means $B = 2.3\ T$. These requirements were achieved with model geometry shown in Fig. 102 which as excited by a coil with 190 turns, which was supplied by an electric current *I*

= *2 A*. Space reserved for the coil winding was dimensioned based on current density $J = 15\ A/mm^2$, which is recommended for the conductors loaded occasionally. Conductor diameter:

$$d = \sqrt{\frac{4 \cdot I}{\pi \cdot J}} = \sqrt{\frac{4 \cdot 2}{\pi \cdot 15}} = 0.41 \rightarrow 0.5\ mm \tag{24}$$

Space intended for coil winding of chosen diameter of wires *0.5 mm* and width of the coil *15 mm* was designed to allow reel the coil in *7* rows. So the space for the coil has the shape of an annulus between the diameters *48* and *55 mm*.

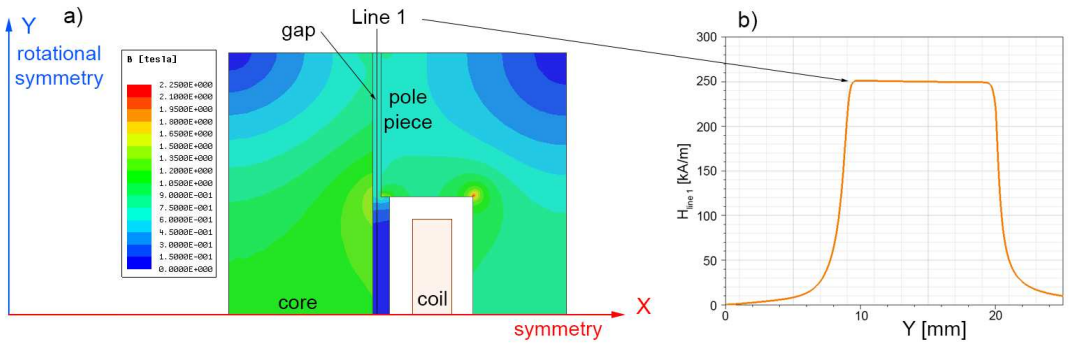

Fig. 102 Magnetic flux density of magnetic circuit a) and intensity of the magnetic field in the gap b)

Magnetic flux density *B* have been kept around half value of *B* which means saturation of the material, because of planned weakening by grooves. The final shape of magnetic circuit take into account that the magnetic flux tends to flow around the coil as close as possible, so, the upper corners of magnetic circuit indicates very low *B*. Thus, chamfer or radius at these corners causes weight reduction and almost none increase of magnetic resistivity.

Grooves of the magnetic circuit were designed in the 3D model in two directions, see Fig. 103: axial, which divides the circuit into circular sectors. Radial grooves are parallel to the magnetic field flow. Fig. 103 shows the basic dimensions of the magnetic circuit.

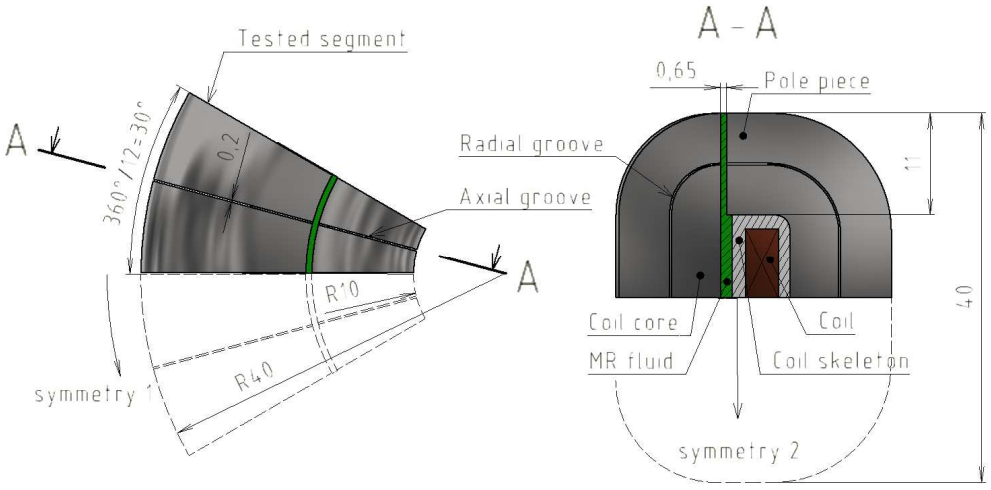

Fig. 103 Grooved magnetic circuit called as 24x2

Rotational symmetry (symmetry 1 in Fig. 103) was used, because of time-consuming simulations. Preliminarily results showed that the lowest number of grooves which gives satisfactory time response is 12, thereby circular sectors of the angle of 30° were created. The magnetic circuit is symmetrical around the horizontal plane (symmetry 2 in Fig. 103); therefore just half of the magnetic circuit was modelled. The example in Fig. 103 illustrates the circuit with 24 axial and 1 radial grooves, thereby 24x2 rods are created.

The magnetic circuit is in model excited by an electric current $I = 2A$ in the coil, see Fig. 104. The resistor is connected to the power supply in series and substitutes the electromagnetic coil resistivity. Transient state of electric current decrease from $I = 2$ *A* onto $I = 0$ is examined. A period necessary to the power supply current output change was set as *0.3 ms* based on the previous measurement. The intensity of magnetic field in the gap (curve 1 in Fig. 104) was observed after the current drop, Magnetic field density was observed at planes 2 and 3 and finally, the current density was observed in plane 3.

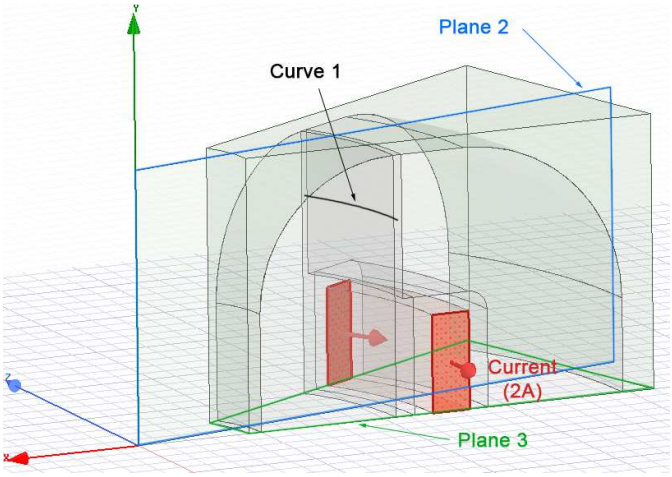

Fig. 104 Model of the magnetic circuit

Firstly, the influence of a number of axial grooves to the time response was tested. Each simulation consists of 20 results of average intensity in the gap in time *0, 0.05, 0.1… 1 ms* after the current drop, see Fig. 105.

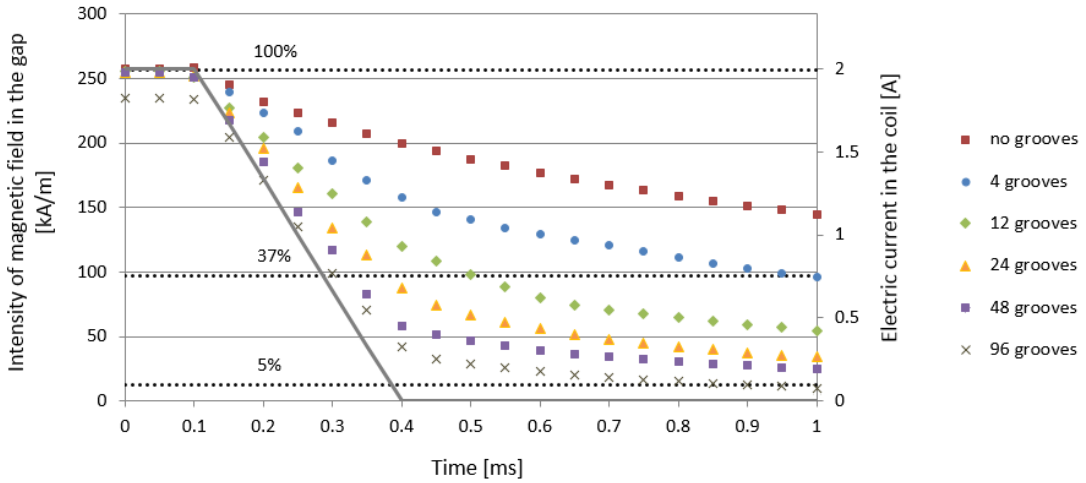

Fig. 105 Influence of axial grooves number to the time response

Grey curve shows a current drop, horizontal lines illustrates the ratio of the maximal intensity of the magnetic field in the gap. In the case of a drop, it is 37% for the primary time response and 5% pro the secondary time response. Other points of the diagram in Fig. 105 illustrates the simulation results for a various number of axial grooves in the magnetic circuit. The higher the number of grooves the shorter the time response of the magnetic circuit. However, a large number of grooves causes saturation of the magnetic circuit in the coil core which results in lower intensity in the gap, see an example of *96* grooves in Fig. 105. The groove is simulated as an area with no electrical conductivity in the model. Eddy currents flow was compared for two chosen magnetic circuits: 0 grooves (left) and 12 grooves (right) by current density in plane 3 at time *t = 0.3* and *1 ms*, see Fig. 106. The simulation of no grooved version of a magnetic circuit that the eddy currents are formed near the edges of the magnetic circuit and it is expanding into the inner sections of the material over time.

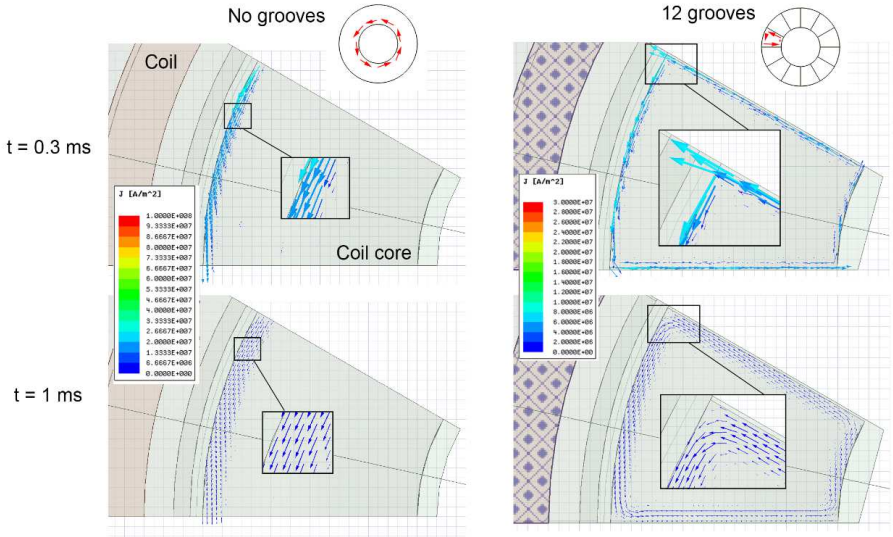

Fig. 106 Eddy currents in plane 3 at 0.3 and 1 ms after the current drop

Shortening of time response was achieved also by the radial grooves. Under certain conditions the axial and radial groove has the same influence to time response, see *24x0* and *12x2* in Fig. 107.

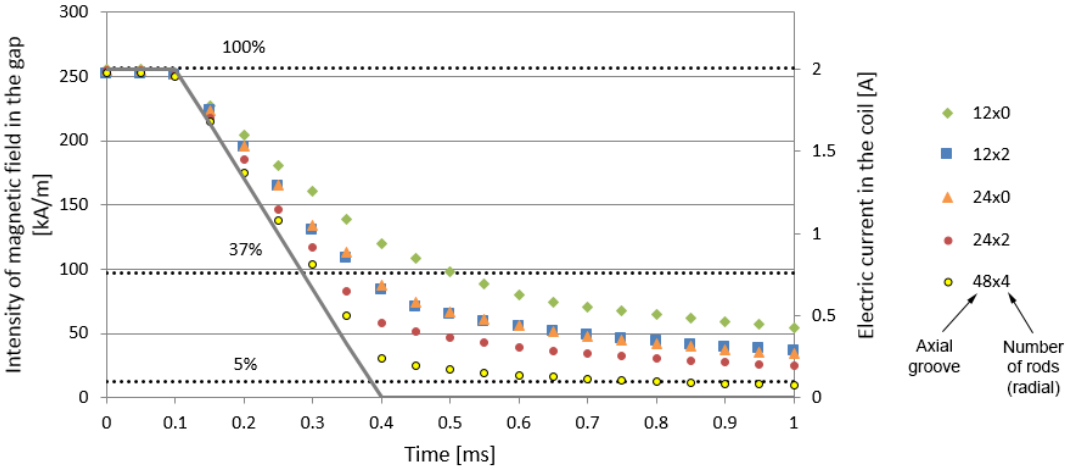

Fig. 107 Influence of grooves number to the time response

Substitution of the axial groove by the radial helps decreases the risk of saturation, which was observed in *96x0* version. Version *48x4* (Fig. 107) is characterized by shorter time response and higher intensity in the gap than the *96x0* version (Fig. 105).

Grooves in axial and radial direction create rods of the magnetic circuit which cross section differs depending on the distance from the axis *Y*, see version 1 on the left side of Fig. 108. Thus, the magnetic field density is not constant in each rod, which is inappropriate due to the unnecessarily high weight of the magnetic circuit. Therefore, the shape of grooves and was modified, see Fig. 108. This figure compares magnetic flux density in three different magnetic circuits with the same excitation, constant current in the coil $I = 2A$ (simulation results for time $t = 0.05\ ms$).

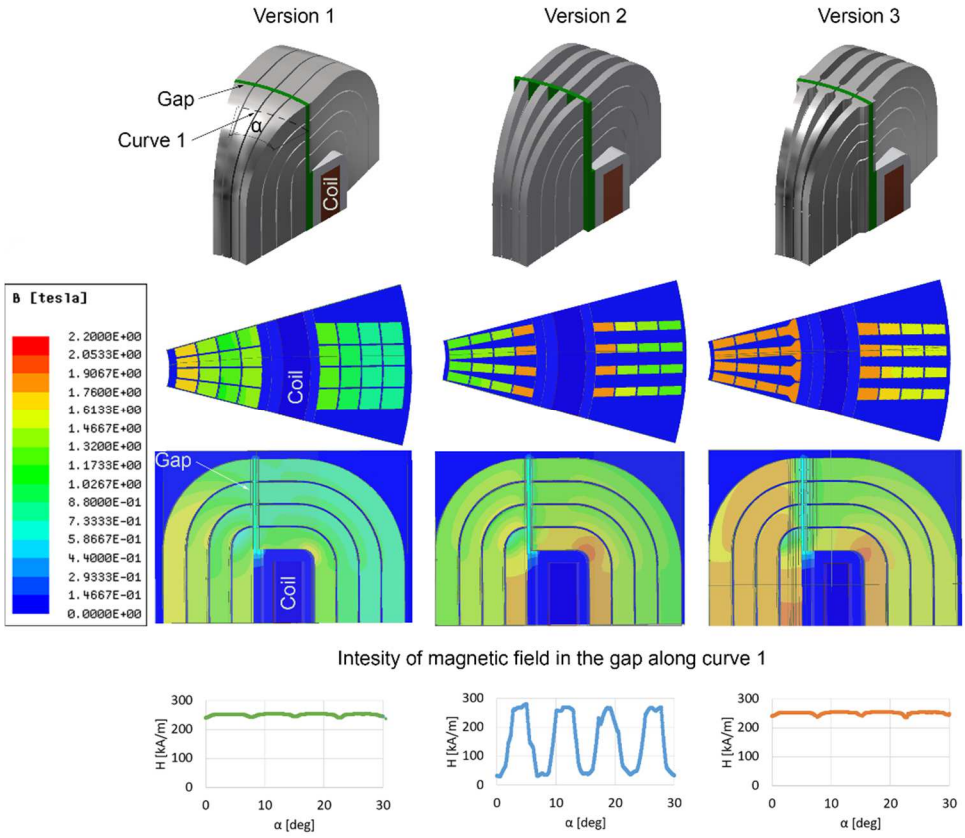

Fig. 108 Saturation of several versions of magnetic circuit excited by I = 2A (t = 0.05 ms)

Version 1 is provided by parallel grooves. The magnetic flux density is the highest at the low diameter of coil core, because of a low cross-section of the rod. Therefore, the cross-section of magnetic circuit rods is the same, which result in a lower mass of the magnetic circuit. The intensity of the magnetic field in rods around the coil is significantly higher than the intensity in other rods because of the shortest path of magnetic flux. Furthermore, the same cross-section of the rods causes high differences between maximal and minimal intensity on the gap, see graphs at the bottom of Fig. 108. That means damping force decrease. Therefore, version 2 is unacceptable.

Positive features of both mentioned version combine version 3. The grooves are wider at higher diameters, which leads to the weight minimization. Problem with uneven magnetic flux density in the gap is solved by a local extension of the rod near the gap.

Version 3 was chosen for the magnetic circuit in the MR strut. Primary time response is approximately *0.2 ms*. However, the time response of power supply is dominant in this value. Secondary time response is approximately *0.7 ms*. Time response of MR fluid (*0.5 ms*) must be added because it is not simulated in the transient model; thus, the time response of the MR valve is estimated at *1.2 ms*. This time response should ensure high-performance vibration elimination of semi-active control, see chap. 5.2.2.

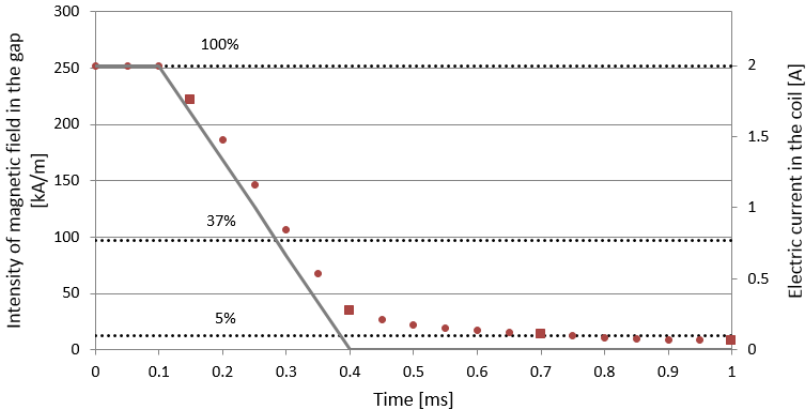

Fig. 109 Intensity of magnetic field in the gap of MR valve

Several points in Fig. 109 are marked by square; the magnetic flux density and the current density is plotted for these times in Fig. 110. Power supply disconnect causes a decrease of magnetic flux density in the magnetic circuit. However, eddy currents induce a secondary magnetic field; therefore, the magnetic flux density drop process is slowed down. Magnetic flux density in the final geometry dropped in coil core from *2* to *0.5 T* per *1 ms*. The most intensive flow of eddy currents was observed in time of *0.4 ms*. Migration of eddy currents deeper to the material is an evident in lower section of Fig. 110, which shows current density in one of the magnetic circuit rods.

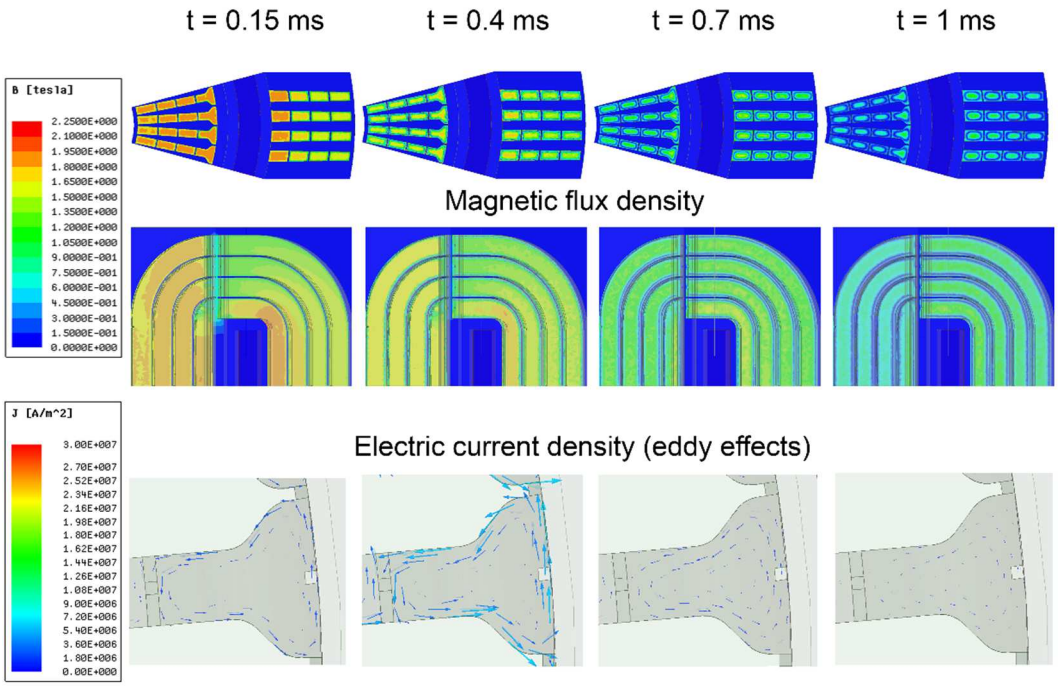

Fig. 110 Saturation of several versions of the mag. circuit (I = 2A, t = 0.05 ms)

Comparison of initial version a) with the final version b) of the magnetic field is in Fig. 111. The final version is grooved. When the grooves would be unfilled, the fluid could flow through them, so the bypass would be very high and the damping force of the MR valve would be very low. Therefore, the grooves will be filled with filled plastic.

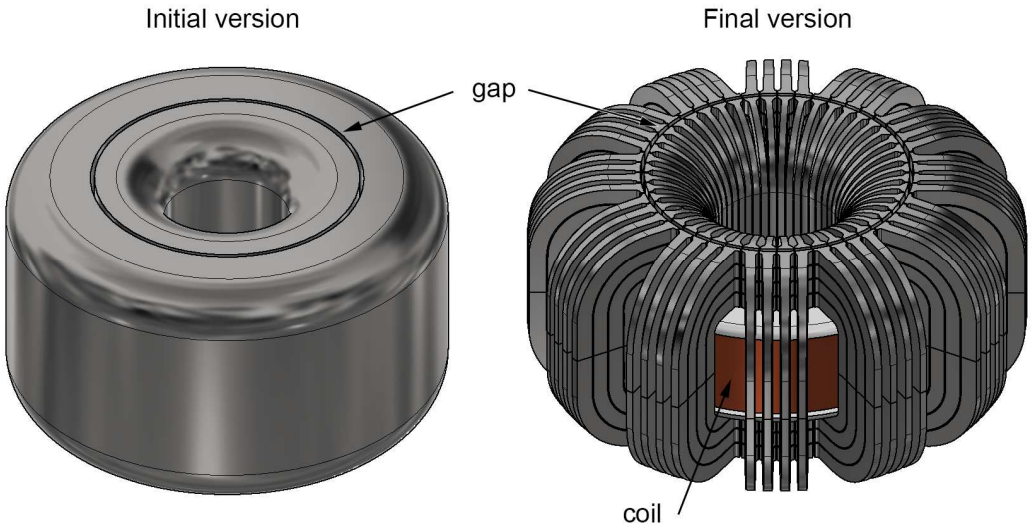

Fig. 111 Initial and final version of the magnetic circuit

Both versions parameters are shown in the tab. 20. The weight of the final version is almost half than the initial version. Moreover, the time response of the final (grooved) version is significantly lower (*20 times*) in comparison with the initial (solid) version. However, the grooves decreased the average intensity of intensity of a magnetic field by *5%*. Even though the outer diameter of the magnetic circuit was increased.

tab. 20 Comparison of an initial and final version of the magnetic circuit

Version	Weight [kg]	Outer diameter [mm]	Primary time response [ms]	Secondary time response [ms]	Intensity of mag. field in the gap [kA/m]
Initial	1.184	69	3.84	15 (approx.)	264
Final	0.632	80	0.22	0.65	251
Difference	-46.6%	+15.9%	-94.3%		-4.6%

5.4.4 Engineering design

The final structural design honours the division into two branches: damping (marked by shades of red in Fig. 112) and spring (shades of yellow). MR fluid is by the strut compression/extension forced to flow from one to another bellows through the MR valve which causes damping.

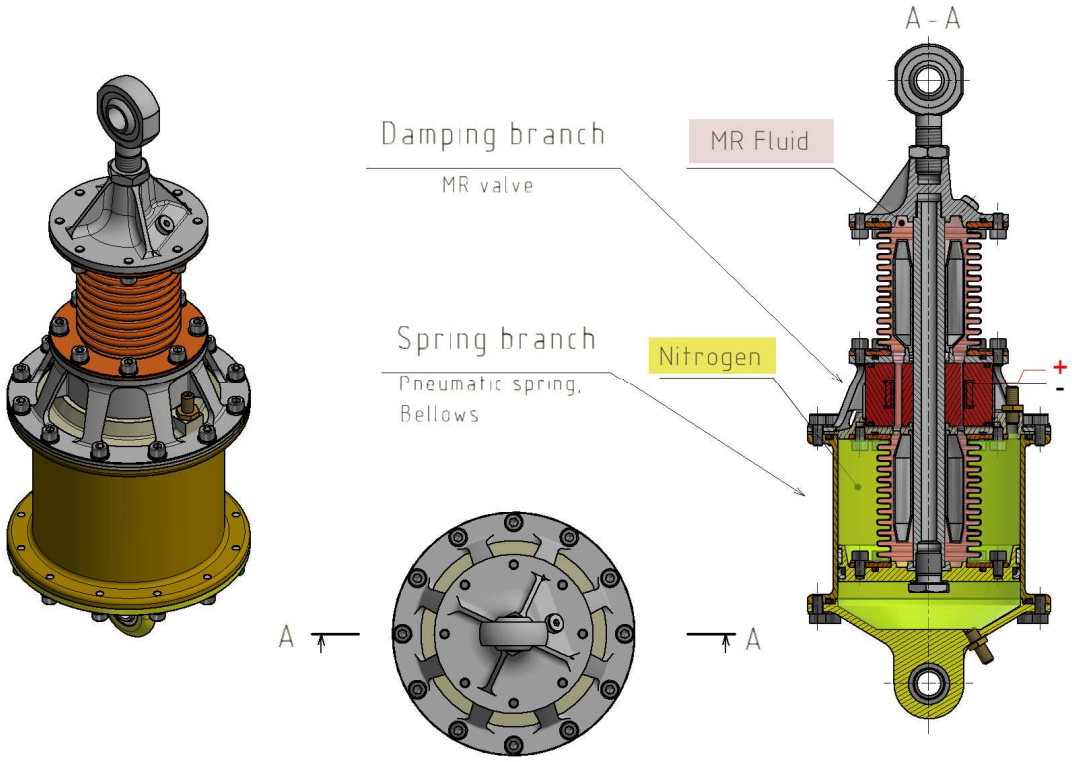

Fig. 112 MR strut branches

Dimensions of **MR valve** design is based on hydraulic and magnetic models described in chap. 5.4.3. The magnetic circuit of the MR valve consists of a coil wound on the skeleton which is surrounded by coil core and pole pieces. The pole pieces have to be dismountable, because of assembly (to insert the coil into the space in pole pieces). The pole pieces consist of 12 segments around the perimeter, which are divided onto 4x4 rods. Thus, a magnetic circuit consists of 196 rods.

The rods are interconnected by bridges, see the detail B in Fig. 113. These bridges are designed just because of manipulation after production. Influence of interconnection of rods by the bridges on time response of MR valve was tested in the magnetic model. The time response increase was negligible: *< 1%*.

Each part of the magnetic circuit will be made by 3D print using method SLM. After the print, the grooves will be filled by plastic *LUKOPREN N 1522*, which provides better interconnection of each rod but above it, the MR fluid flows only through the gap and bypass. Shoulders created on the plastic casting serve positioning of MR valve, especially the coil core and the pole pieces. The plastic cast is higher than the magnetic circuit by *0.5 mm* in all dimensions. This allowance is designed because of machining to achieve precise geometry of MR valve.

The bypass was considered circular in the hydraulic model. However, it was transferred to an ellipse with the same cross section because of the possibility to place into a groove of MR valve. Wall of the bypass is made of Vacoflux which has higher resistivity against abrasive wear in comparison with Lukopren. The coil connected with the power supply by conductors put through the wire hole, see Fig. 113 and then through a groove in MR valve body (pos. 2 in Fig. 114).

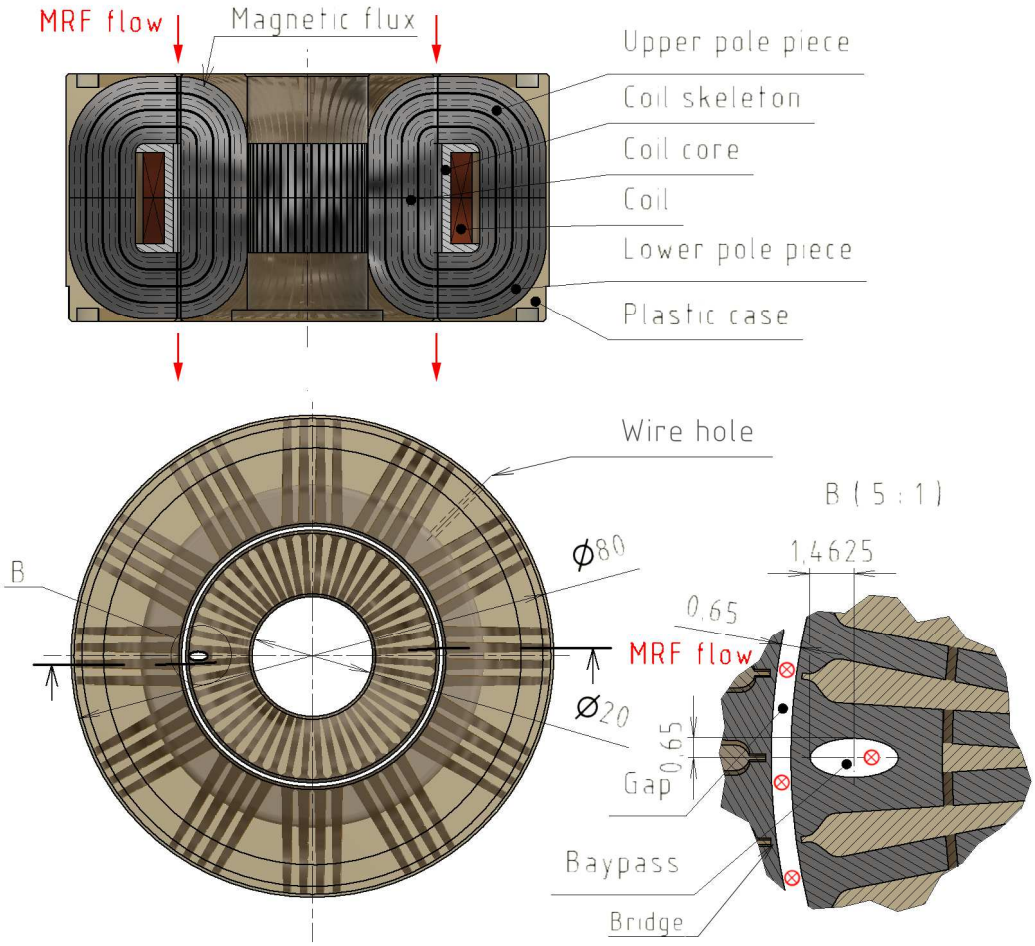

Fig. 113 Design of MR valve

The distance between connection eyes of the **MR strut** is *380 mm* in an equilibrium position. However, the length can be adjusted in the range of approximately ±*2 mm* by the screw of the eye (pos. 19) and fixed by a nut (pos. 27). When the lower eye (pos. 20) is consider fixed, force loading of the upper eye causes an adapter (pos. 6) movement which is transferred to the piston of pneumatic spring (pos. 7) by a piston rod (pos. 8). Movement of the piston changes the pressure in the pneumatic spring chambers but also causes the bellows deformation (pos. 9). One of the bellows is compressed the other one is stretched, opposite faces of bellows are interconnected by the piston rod. That causes MR fluid flow through the MR valve (pos. 1), which is clamped between MR valve body (pos. 2) and flange (pos. 5) by screws M6 (pos. 22).

MR fluid is filled by a plug (pos. 21), which is used also for deaeration of MR strut. The Nitrogen is fed into the pneumatic spring through valves. One of them is in the flange and uses for upper chamber of pneumatic spring. The second one is screwed into the lid (pos. 4) and it is designed for the lower chamber filling.

The piston and piston rod of the MR strut is guided by PTFE guidelines (pos. 13 and 11) one of them has diameter *20 mm* and it touches the piston rod and the other one has diameter *115 mm* and it touches cylinder of pneumatic spring (pos. 3). In the piston, there is only one dynamic seal of the strut, which prevents gas flow around the piston.

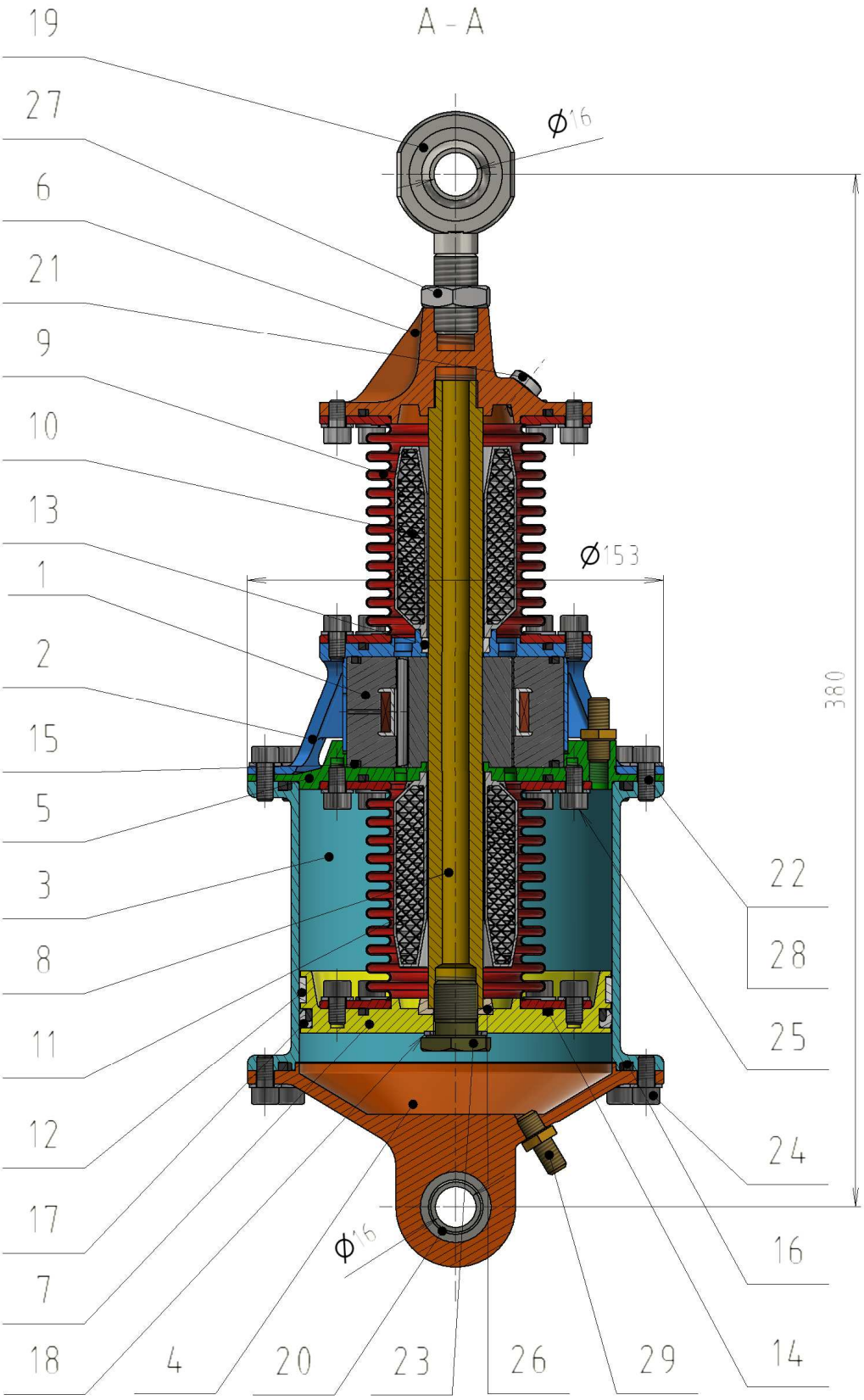

Fig. 114 Design of MR strut for VIS of the launch vehicle

Internal seals in the strut, for example in threads of the piston rod is not designed to leakage impossibility. Therefore, the threats of piston rod is coated by sealant before thickening. These threats of piston rod fit in other parts: screw (pos. 23) or adapter which is as well as piston rod made of titanium, because of high stress in the threads. The screw connected piston rod and the piston, which is made of magnesium. Because of lower allowed compressive stress of magnesium, there is a washer (pos. 26) made of titanium between the piston and piston rod.

The total mass of MR strut was minimized by the sophisticated design of each part of the MR strut. Used material and weight of each component of MR strut is the tab. 21.

tab. 21 Comparison of an initial and final version of the magnetic circuit

Pos.	Name of part	Material	Weight [g]	Quantity
1	MR valve	Vacoflux / Lukopren / cooper /	693	1
2	MR valve body	AZ80A-T5 (magnesium alloy)	169	1
3	Cylinder	AZ80A-T5	337	1
4	Lid	AZ80A-T5	225	1
5	Flange	AZ80A-T5	159	1
6	Adapter	Ti6Al4V (titanium alloy)	279	1
7	Piston	AZ80A-T5	176	1
8	Piston rod	Ti6Al4V	230	1
9	Bellows	1.4571 (stainless steel)	447	2
10	Upper stopper	AZ80A-T5	49	1
11	Lower stopper	AZ80A-T5	48	1
12	Piston guideline	PTFE	2	1
13	Piston rod guideline	PTFE	11	1
14	Seal 66x2.5	NBR	1	4
15	Seal 71x2.5	NBR	2	2
16	Seal 123x3.4	NBR	4	2
17	Piston seal	NBR / PTFE	9	1
18	Bonded seal	NBR / Steel	2	1
19	Rod end M81935/1	Ti6Al4V	127	1
20	Lower eye MS14104	Ti6Al4V	16	1
21	Plug	AZ80A-T5 / NBR	2	1
22	Screw M6x16	Ti6Al4V	4	12
23	Piston rod screw	Ti6Al4V	23	1
24	Screw M6x12	Ti6Al4V	3	12
25	Screw M6x10	Ti6Al4V	3	32
26	Washer	Ti6Al4V	8	1
27	Nut	Ti6Al4V	12	1
28	Split washer 6.4	Ti6Al4V	0.4	56
29	Taxer valve	C-360 (brass alloy)	9	2

Margins of Safety *MS* of several chosen parts of MR strut was determined by the yield stress by analytically, using FEM or by comparison of limit and real force loading of the part see in tab 22. All of these analysis results were calculated with safety factor FoS = 1.25 [80]:

$$MS = \frac{Rp_{0.2}}{FoS \cdot \sigma_{red}} - 1 \tag{25}$$

tab. 22 The margin of safety for chosen parts of MR strut

Pos	Part	Type of Analysis	MS
2	MR valve body	FEM	0.22
3	Cylinder	analytically	0.81
4	Lid	analytically	0.93
6	Adapter	FEM	0.41
8	Piston rod	analytically	0.03
9	Bellows	FEM	0.33
10	Stoppers	FEM	0.08
19	Rod end	RBC bearings Product list	0.41
20	Lower eye	RBC bearings Product list	0.73
26	Washer	analytically	0.29

The total mass of MR strut can be estimated when the mass of MR fluid is known. The volume of the space, where the MR fluid is filed is approximately 186 ml, thus weight of the fluid 443 g. Therefore, **the total mass of the MR strut is 4.145 kg** in operational condition. The weight of the previously designed strut with external MR (FLPP 3) for the same loading is 8.03 kg [79]. Several parts were slightly modified (pos. 3, 4, 6, 10 etc.) but, the most significant reduction of weight was achieved by the re-design of MR valve (pos. 1), that means replace 3 coils external MR valve made of ferrites by internal single coil MR valve made of Vacoflux. The weight reduction is almost 50 %.

6 CONCLUSIONS

Design of the Magnetorheological (MR) strut for vibration isolation system (VIS) of the launch vehicle consists of many activities from a search of previous designs and learning from them, through simulations and design, to vibration tests. All of the necessary activities are summed in the presented thesis. The methodology used in the MR strut design process can hopefully be re-used in future MR strut or MR damper designs.

Vibration elimination in launch vehicle is specific in many factors: the vibration environment is quite hard and the frequency range is very wide. Any fluid fillings are allowed to be used only in case of their complete and reliable sealing. Finally, the weight of the vibration isolation system is very important factor in the assessment of the design. Previously designed VIS were summarized and divided into structural and mechanical groups. One of the mechanical VIS called ELVIS was chosen as an inspiration for this thesis and therefore, analysed to understand design background. The VIS conceptually designed in this thesis is a combination of structural and mechanical VIS especially because of the wide frequency range of the vibration environment in the launch vehicle. However, the thesis is primarily focused on the mechanical part of the VIS (Stewart platform) and specifically on the single strut of the mechanism.

The strut of the VIS in this study consists of springs and magnetorheological damper enabling semi-active control of damping force. The benefit of semi-actively control in comparison to passive damping was proved by simulations of multi-body models. The models also served for the determination of the strut parameters and investigated their impact on the vibration elimination efficiency.

The simulations with the semi-active algorithm ON/OFF skyhook have shown that the most significant factor of semi-actively controlled dampers is their time response. The lower time response the damper exhibits the lower transmissibility of vibrations can be achieved by VIS equipped by this damper. Dynamic force range increase (in this case increased by OFF state damping drop) causes a slight increase of the transmissibility in the vicinity of resonance but the significant drop of the transmissibility in the isolation area.

Transmissibility at high frequencies of excitation (isolation area) of a system with passive viscous damper can be decreased by the elastically connected damper. But simultaneously with a slight increase in the transmissibility in the vicinity of resonance. The simulations confirmed that this fact is valid also for the semi-active control. However, the influence of the flexibility of the damper connection on the vibration transmissibility is various, depending on the time response of the damper. An Ultra-fast damper (with time response around *1 ms*) suppressed the transmissibility increase much more effectively than a damper with common time response (around *10 ms*).

The requirement of perfect sealing of the MR strut for VIS of the launch vehicle was solved by the use of elastic metal bellows sealed by static seals as the only possible way of safe sealing. A damper with elastic bellows used for the damping medium case must be considered elastically connected. The stiffness of the connection is affected by the resistance of the bellows length changes against the internal pressure increase – pressure thrust stiffness.

The pressure thrust stiffness is not a commonly available parameter of the bellows. Therefore, the FEA of bellow filled with a fluid was provided and verified by measurement in this thesis. Moreover, sensitivity analysis revealed that the mean diameter of damper and width of corrugation affects axial and pressure thrust stiffness differently. Thus, the ratio between axial and pressure thrust stiffness of bellows can be adjusted by these two parameters of bellows.

Two versions of MR strut were designed in this study, one of them: the experimental strut was also manufactured and tested. This test provided valuable knowledge which was used in the final MR strut design for the VIS of the launch vehicle.

One of the most important findings was that the elastic bellows allow oscillations of MR fluid which appears as a peak in the transfer function. This phenomenon is called fluid mass effect and its future research could help to clarify the reason why the resonance frequency is not dependent only on the mass of a fluid and the stiffness of bellows.

The magnetic circuit made of ferrite was damaged during testing of the experimental strut. The ferrite rings cracked because of strong force impulse occurring during vibration elimination by semi-actively controlled MR damper. This material is not suitable for parts of the magnetic circuit which are loaded by a force. Therefore, a new way of very fast magnetic circuit designing has been investigated in this study – shape approach.

The main aim of shape approach, as well as the material approach of fast magnetic circuit design, is the eddy currents elimination. A magnetic circuit with suitably designed grooves can achieve similar time response as the circuit made of a material with very low electrical conductivity (for example the ferrite). Moreover, a material with a higher level of saturation can be used for shape approach. This results in a significant weight reduction of the magnetic circuit.

The magnetic circuit of the MR strut of VIS for the launch vehicle is made of Vacoflux 50. The magnetic circuit contains 48 grooves in the axial direction (created circular sectors) and 4 radial grooves (parallel to magnetic flux). Both types of grooves together created 192 rods of the magnetic circuit which are electrically isolated by grooves filled with plastic. This design of magnetic circuit exhibits primary time response (step from *100* to *32.7 %* of the damping force) of *0.2 ms* and secondary response (step from *100* to *5 %* of damping force) of around *0.7 ms* in the case of the electrical current drop takes *0.3* ms from *2 A* onto *0 A*. Estimated secondary time response of the MR strut with this magnetic circuit is *1.2 ms* (containing the MR fluid time response itself).

The grooved magnetic circuit is also very efficient in terms of weight. The MR strut designed with an external MR valve made of ferrite had nearly twice the mass in comparison with the grooved magnetic circuit of the MR strut. Both mentioned struts were designed for the same loading. Nevertheless, the weight penalty in comparison of less efficient but lighter passive adapters will be probably acceptable only for the transport of extremely sensitive payloads. However, the MR strut can be applied in other fields of vibration isolation, where the weight is not the decisive factor.

7 LIST OF PUBLICATIONS AND PATENTS

7.1 Papers published in journals with impact factor

MACHÁČEK, O.; KUBÍK, M.; STRECKER, Z.; ROUPEC, J.; MAZŮREK, I. Design of Frictionless Magnetorheological Damper with High Dynamic Force Range. Advances in Mecahnical Engineering.
(Under review)

KUBÍK, M.; MACHÁČEK, O.; STRECKER, Z.; ROUPEC, J.; MAZŮREK, I. Design and testing of magnetorheological valve with fast force response time and great dynamic force range. Smart Materials and Structures, 2017. 26(4), 47002. ISSN 0964-1726

STRECKER, Z.; MAZŮREK, I.; ROUPEC, J.; MACHÁČEK, O.; KUBÍK, M. Influence of Response Time of Magnetorheological Valve in Skyhook Controlled Three-Parameter Damping System. Advances in Mecahnical Engineering.
(After review)

STRECKER, Z.; MAZŮREK, I.; ROUPEC, J.; MACHÁČEK, O.; KUBÍK, M.; KLAPKA, M. Design of magnetorheological damper, with short time response. Journal of Intelligent Material Systems and Structures, 2015, vol. 26, no. 14, p. 1951-1958. ISSN: 1045- 389X.

ROUPEC, J.; BERKA, P.; MAZŮREK, I.; STRECKER, Z.; KUBÍK, M.; MACHÁČEK, O., ANDANI, M. Taheri. A novel method for measurement of MR fluid sedimentation and its experimental verification. Smart Materials & Structures, 2017, vol. 26, no. 10, p. 1-13. ISSN: 0964-1726.

KLAPKA, M.; MAZŮREK, I.; MACHÁČEK, O.; KUBÍK, M. Twilight of the EUSAMA diagnostic methodology. MECCANICA, 2016, vol. 52, no. 9, p. 2023-2034. ISSN: 0025-6455.

KLAPKA, M.; MAZŮREK, I.; KUBÍK, M.; MACHÁČEK, O. Reinvention of the EUSAMA diagnostic methodology. International Journal of Vehicle Design, 2017, vol. 4, no. 74, p. 304-318. ISSN: 0143-3369.

7.2 Papers published in journals indexed in Scopus

KUBÍK, M., O. MACHÁČEK a I. MAZŮREK, 2016. A Study of Hydraulic Resistance of Viscous Bypass Gap in Magnetorheological Damper. Acta Universitatis Agriculturae et Silviculturae Mendelianae Brunensis. 64(4), 1199-1203. DOI: 10.11118/actaun201664041199. ISSN 1211-8516.

7.3 Papers in conference proceedings indexed in WoS or Scopus

MACHÁČEK, O.; KUBÍK, M.; MAZŮREK, I.; STRECKER, Z.; ROUPEC, J. Frictionless Bellows Unit Connected with the Magnetorheological Valve. In Engineering Mechanics 2016. Praha: Institute of Thermomechanics Academy of Sciences of the Czech Republic, 2016. p. 354-357. ISBN: 978-80-87012-59- 8.

MACHÁČEK, O.; KUBÍK, M.; NOVÁK, P. A New Method of Magnetorheological Damper Quality Evaluation. In Engineering Mechanics 2017. Praha: Institute of Thermomechanics Academy of Sciences of the Czech Republic, 2017. p. 594-597. ISBN: 978-80-214-5497-2.

MACHÁČEK, O.; KUBÍK, M.; ROUPEC, J.; STRECKER, Z.; MAZŮREK, I. Micro-Fluidic System with Grooved Pole Pieces of Magnetic Circuit. In ENGINEERING MECHANICS 2018. Praha: Institute of Thermomechanics Academy of Sciences of the Czech Republic, 2018. p. 521-524. ISBN: 978-80-86246-88-8.

MACHÁČEK, O.; KUBÍK, M.; STRECKER, Z.; ROUPEC, J.; NOVÁK, P.; MAZŮREK, I. Axial and Pressure Thrust Stiffness of Metal Bellows for Vibration Isolators. In MATEC Web of Conferences. MATEC Web of Conferences. 2018. p. 1-5. ISSN: 2261-236X.

KUBÍK, M.; MACHÁČEK, O.; ROUPEC, J.; STRECKER, Z.; NOVÁK, P.; MAZŮREK, I. Transient magnetic model of magnetorheological damper and its experimental verification. In ICMME 2017. MATEC Web of Conferences. MATEC web of Conferences, 2018. p. 1-5. ISSN: 2261-236X.

KUBÍK, M.; MACHÁČEK, O.; STRECKER, Z.; ROUPEC, J.; MAZŮREK, I. Dynamic viscosity of commercially available magnetorheological fluids. In 23rd International Conference ENGINEERING MECHANICS 2017. 2017. p. 538-541. ISBN: 978-80-214-5497-2.

KUBÍK, M.; MACHÁČEK, O.; STRECKER, Z.; ROUPEC, J.; MAZŮREK, I. Hydraulic resistance of magnetorheological damper viscous bypass gap. In Engineering Mechanics 2016. Praha: Institute of Thermomechanics Academy of Sciences of the Czech Republic, 2016. p. 330-333. ISBN: 978-80-87012-59- 8. ISSN: 1805-8248.

KUBÍK, M.; MACHÁČEK, O; MAZŮREK, I. Magnetorheological Fluid Seal with Minimum Friction Torque. In Engineering Mechanics 2018. Praha: Institute of Thermomechanics Academy of Sciences of the Czech Republic, 2018. p. 445-448. ISBN: 978-80-86246-88-8.

STRECKER, Z.; ČÍPEK, P.; ROUPEC, J.; MACHÁČEK, O.; KUBÍK, M. Testing of Car Suspension With Fast MR Damper, Controlled by Modified Groundhook Algorithm. In Engineering Mechanics 2016. Prague: Institute of Thermomechanics Academy of Sciences of the Czech Republic, 2016. p. 526-529. ISBN: 978-80-87012-59- 8. ISSN: 1805-8248.

STRECKER, Z.; STRMISKA, T.; ROUPEC, J.; KUBÍK, M.; MACHÁČEK, O. Design of Fast Magnetorheological Damper Using Soft Magnetic Composites. In Engineering Mechanics 2017. Praha: Institute of Thermomechanics Academy of Sciences of the Czech Republic, 2017. p. 934-937. ISBN: 978-80-214-5497-2.

ROUPEC, J.; MAZŮREK, I.; STRECKER, Z.; KUBÍK, M.; MACHÁČEK, O. Temperature dependence of magnetorheological fluid yield stress and Bingham viscosity. In Engineering Mechanics 2016. Praha: Academy of Science of the Czech Republic, v.v.i., 2016. p. 498-501. ISBN: 978-80-87012-59- 8. ISSN: 1805-8248.

ROUPEC, J.; MAZŮREK, I.; STRECKER, Z.; KUBÍK, M.; MACHÁČEK, O. Tensile Strength of Pure Iron Samples Manufactured by Selective Laser Melting Method. In Engineering Mechanics 2017. Praha: Institute of Thermomechanics Academy of Sciences of the Czech Republic, 2017. p. 830-833. ISBN: 978-80-214-5497-2.

KLAPKA, M.; MAZŮREK, I.; MACHÁČEK, O. Analysis of Causes of False-Negative Evaluation of Eusama Methodology for Suspension Asessment. In Engineering Mechanics 2016. Prague: Institute of Thermomechanics, Academy of Sciences of the Czech Republic, 2016. p. 282-285. ISBN: 978-80-87012-59- 8.

7.4 Papers in conference proceedings

7.3

KUBÍK, M.; MACHÁČEK, O.; STRECKER, Z.; MAZŮREK, I. FEM model of magnetic circuit and its verification. In Book of Proceeding of 56th International Conference of Machine Design Departments. Nitra: Publishing Center SUA Nitra, 2015. p. 99-104. ISBN: 978-80-552-1377- 4.

7.5 Patent

7.4

KUBÍK M.; MACHÁČEK O.; STRECKER Z.; ROUPEC J.; MAZUREK I.; KOUTNY D.; PALOUŠEK D., 2017. A Core Skeleton Made of Rods of Ferromagnetic Material. 307249, 2018.

8 LITERATURE

[1] The Price of Space, 2018. News from the Galactic Centre [online]. New Zealand [cit. 2018-08-14]. Link: https://milky-way.kiwi/2018/01/25/the-price-of-space/

[2] DAVIS, L. P., J. F. WILSON and R. E. JEWELL, 1986. Hubble Space Telescope Reaction Wheel Assembly Vibration Isolation System. Alabama, Arizona: National Aeronautics and Space Administration.

[3] Ariane 6, M's old blog [online]. [cit. 2018-08-23]. Link: http://armchairengineer.blogspot.com/2014/02/ariane-6-where-does-it-come-from-and.html

[4] EILERS, D. a A. RITTWEGER. LPDR Study Executive Summery Report. Bremen, 2007. Link: http://esamultimedia.esa.int/docs/gsp/completed/C16812ExS.pdf

[5] SCIULLI, D. Dynamics and Control for Vibration Isolation Design. Blacksburg, Virginia, 1997. Dissertation. Virginia Polytechnic Institute and State University.

[6] HARRIS, C. M. and A. G. PIERSOL, 2002. Harris' shock and vibration handbook. 5th ed. New York: McGraw-Hill, ISBN 0071370811.

[7] RUEBSAMEN, D. T., 2003. Evolved launch vibration isolation system (ELVIS) demonstration unit test results. In: Proc. of the 2003 S/C and L/V dynamics Environments Workshop, The Aerospace Corporation. El Segundo: California, s.

[8] HADDEN, S., D. T. RUEBSAMEN and R. GOOLD, Three parameter, multi-axis isolators, isolation systems employing the same, and methods for producing the same. USA. US9103403B2. 2011-04-25.

[9] BRENNAN, M.J., A. CARRELLA, T.P. WATERS and V. LOPES, 2008. On the dynamic behaviour of a mass supported by a parallel combination of a spring and an elastically connected damper. Journal of Sound and Vibration. 309(3-5), 823-837. DOI: 10.1016/j.jsv.2007.07.074. ISSN 0022460x.

[10] LIU, Y., T.P. WATERS and M.J. BRENNAN, 2005. A comparison of semi-active damping control strategies for vibration isolation of harmonic disturbances. Journal of Sound and Vibration. 280(1-2), 21-39. DOI: 10.1016/j.jsv.2003.11.048. ISSN 0022460x.

[11] SUN, J. Q., M. R. JOLLY and M. A. NORRIS, 1995. Passive, Adaptive and Active Tuned Vibration Absorbers—A Survey. Journal of Mechanical Design. 117(B), 234-241. DOI: 10.1115/1.2836462. ISSN 10500472.

[12] HOUSNER, G. W., L. A. BERGMAN, T. K. CAUGHEY, et al., 1997. Structural Control: Past, Present, and Future. Journal of Engineering Mechanics. 123(9), 897-971. DOI: 10.1061/(ASCE)0733-9399(1997)123:9(897). ISSN 0733-9399.

[13] WILKE, P, C JOHNSON, P GROSSERODE and D SCIULLI, 2000. Whole-spacecraft vibration isolation for broadband attenuation. In: 2000 IEEE Aerospace Conference. NEW YORK, USA: IEEE, 315-321.

[14] WHITE, J., E. FOWLER a K. NOBLE, 2015. SoftRide® Shock and Vibration Isolation Systems. In: 2nd Workshop on Spacecraft Shock Environment and Verification. Noordwijk: ECSS, 1-10.

[15] MOROZOV, E.V., A.V. LOPATIN and V.A. NESTEROV, 2011. Buckling analysis and design of anisogrid composite lattice conical shells. Composite

Structures. 93(12), 3150-3162. DOI: 10.1016/j.compstruct.2011.06.015. ISSN 02638223.

[16] PEREZ, E. Ariane 5: User's Manual. Paris, 2011.

[17] PEREZ, E. Vega: User's Manual. Paris, 2006.

[18] PEREZ, E. Soyuz: User's Manual. Paris, 2006.

[19] PAYLOAD ADAPTER. EADS CASA [online]. Espacio: Opinio, 2013 [cit. 2016-05-23]: http://www.casaespacio.es/products/payloadadapter.

[20] LANCHO, M., A. FERNÁNDEZ and S. KIRYENKO, 2005. Shock attenuation system for spacecraft and adaptor (SASSA). In: Proceedings of the European Conference on Spacecraft Structures. Noordwijk, The Netherlands: Karen Fletcher.

[21] ANDERSON, E.H., D. J. LEO, M. D. HOLCOMB and I. CHOPRA, 1996. Ultraquiet platform for active vibration isolation. SMART STRUCTURES AND INTEGRATED SYSTEMS. 1996-5-1, 1996(2717), 436-451. DOI: 10.1117/12.239046.

[22] LEE, D.O., G. PARK a J.H. HAN, 2015. Experimental study on on-orbit and launch environment vibration isolation performance of a vibration isolator using bellows and viscous fluid. Aerospace Science and Technology. 45, 1-9. DOI: 10.1016/j.ast.2015.04.012. ISSN 12709638.

[23] CHI, W., D. CAO, D. WANG, J. TANG, Y. NIE and W. HUANG, 2015. Design and Experimental Study of a VCM-Based Stewart Parallel Mechanism Used for Active Vibration Isolation. Energies. 8(8), 8001-8019. DOI: 10.3390/en8088001. ISSN 1996-1073.

[24] HU, F. and X. JING, 2018. A 6-DOF passive vibration isolator based on Stewart structure with X-shaped legs. Nonlinear Dynamics. 91(1), 157-185. DOI: 10.1007/s11071-017-3862-x. ISSN 0924-090X.

[25] COBB, R. G., J. M. SULLIVAN, P. DAVIS, T. T. HYDE, et. Al.. Vibration isolation and suppression system for precision payloads in space. Smart Materials and Structures. 1999, 8(6), 798-812. DOI: 10.1088/0964-1726/8/6/309. ISSN 0964-1726.

[26] KAVEHPOUR, H.P. a G.H. MCKINLEY, 2004. Tribo-Rheometry: From Gap-Dependent Rheology to Tribology. Tribology Letters. 17(2), 327-335. DOI: 10.1023/B:TRIL.0000032471.06795.ea. ISSN 1023-8883.

[27] Space X [online], ©2017. HAWTHORNE, CALIFORNIA: SPACE EXPLORATION TECHNOLOGIES [cit. 2018-06-19]. http://www.spacex.com/falcon9.

[28] DAVIS, P. and D. A. OSTERBERG, Heavy load vibration isolation apparatus. USA. US5803213A. 1998-09-08.

[29] DAVIS, P., D. CUNNINGHAM and J. HARRLER. Advanced 1.5 Hz Passive Viscous Isolation System. In: Adaptive Structures Forum. Reston, Virigina: American Institute of Aeronautics and Astronautics, 1994, -. DOI: 10.2514/MASF94.

[30] BOYD, James, H, Timothy, A HINDLE, Tristram, T HYDE and David, A OSTERBERG. A viscous isolation and damping strut utilizing a fluid mass effect. WO2005095822 A1. 2005-10-06.

[31] COLEMAN, S.L.C, Vehicle suspension. USA. US1297325A. 1919-03-18.

[32] Swaybars and Accessories, 2018. Elephant Racing [online]. Elephant Racing [cit. 2018-06-20]. http://www.elephantracing.com/porsche/911/swaybars-for-911/.

[33] HINDLE, T., J. BOYD, D. OSTERBERG and T. HYDE, Viscous isolation and damping strut utilizing a fluid mass effect. US20050217954A1. 2005-10-06.

[34] PAVIC, A., T. ARMITAGE, P. REYNOLDS a J. WRIGHT. Methodology for modal testing of the Millennium Bridge, London. PROCEEDINGS OF THE INSTITUTION OF CIVIL ENGINEERS-STRUCTURES AND BUILDINGS. 2002, 152 (2). 111-121. ISSN 0965-0911.

[35] Images, 2014. Metalic Bellows [online]. Vettuvankeni Village, India [cit. 2018-06-20]. http://www.metallicbellows.org/images/DSC_0545-big.jpg.

[36] GHENI, M., H. MUSHA, N. YUSUP and K. BAKI, 2011. Flexibility Analysis of the Welded Metal Bellows of Mechanical Seal. Key Engineering Materials. 462-463, 894-899. DOI: 10.4028/462-463.894. ISSN 1662-9795.

[37] PRASANNA NAVEEN KUMAR, J., S. JOHNS KUMAR, R. K. SARATHI JEYATHILAK, M. VENKATESH, A. SIMON CHRISTOPHER and K. C. GANESH, 2017. Effect of design parameters on the static mechanical behaviour of metal bellows using design of experiment and finite element analysis. International Journal on Interactive Design and Manufacturing (IJIDeM). 11(3), 535-545. DOI: 10.1007/s12008-016-0306-7. ISSN 1955-2513.

[38] KUMAR, J. P. N., S. J. KUMAR, R. K. S. JEYATHILAK, M. VENKATESH, A. S. CHRISTOPHER and K. C. GANESH, 2017. Effect of design parameters on the static mechanical behaviour of metal bellows using design of experiment and finite element analysis. International Journal on Interactive Design and Manufacturing (IJIDeM). 11(3), 535-545. DOI: 10.1007/s12008-016-0306-7.

[39] DU, W. J., H. H. WANG and S.D. WEN, 2017. Finite element analysis of double layer metal bellows flexible hose for chemical pipeline. In: AMCCE 2017. Paris: ATLANTIS PRESS, 106-110.

[40] FARAJI, G., M. K. BESHARATI, M. MOSAVI and H. KASHANIZADEH, 2008. Experimental and finite element analysis of parameters in manufacturing of metal bellows. The International Journal of Advanced Manufacturing Technology. 38(7-8), 641-648. DOI: 10.1007/s00170-007-1122-9. ISSN 0268-3768.

[41] THAKKAR, H. R. Study of design aspects of expansion joints with metallic bellows and their performance evaluation. Sardar Patel University, 2011. Supervisor: George,P. M.

[42] Pressure Thrust, 2005. Hyspan [online]. Hyspan Precision Products [cit. 2018-06-20]. http://www.hyspan.com/pdfs/PressureThrustNotes.pdf.

[43] WAHAD, H. S., A. TUDOR, M. VLASE, N. CERBU and K. A. SUBHI, 2017. The effect of friction in coulombian damper. IOP Conference Series: Materials Science and Engineering. 174, 012021-. DOI: 10.1088/1757-899X/174/1/012021. ISSN 1757-8981.

[44] ROUPEC, J., MAZŮREK, I., STRECKER, Z. and KLAPKA, M. The behavior of the MR fuid during durability test. Journal of Physics Conference Series ERMR 2012. Vol. 412, 2013, p. 012024.

[45] WINSLOW, W. M., 1949. Induced Fibration of Suspensions. Journal of Applied Physics. 20(12), 1137-1140. DOI: 10.1063/1.1698285. ISSN 0021-8979.

[46] RABINOW, J. 1948. The magnetic fluid clutch. Electrical Engineering. 67(12), 1167-1167. DOI: 10.1109/EE.1948.6444497. ISSN 0095-9197.

[47] MAZŮREK, I., J. ROUPEC, M. KLAPKA and Z. STRECKER, 2013. Load and rheometric unit for the test of magnetorheological fluid. Meccanica. 48(3), 631-641. DOI: 10.1007/s11012-012-9620-8. ISSN 0025-6455.

[48] HANLON, M., Audi's new magnetic semi-active suspension system. Automtive [online]. 2006 [cit. 2018-06-20]. https://newatlas.com/go/5752/.

[49] YANG, G., B.F. SPENCER, J.D. CARLSON and M.K. SAIN. Large-scale MR fluid dampers: modeling and dynamic performance considerations. Engineering Structures. 2002, vol. 24(3): 309-323. DOI: 10.1016/S0141-0296(01)00097-9. ISSN 01410296.

[50] SPENCER Jr. BF, YANG G, CARLSON JD andSAIN MK. Smart dampers for seismic protection of structures: a full-scale study. In: Proceedings of 2nd World Conference on Structural Control, vol. 1, Kyoto, Japan, 1998. p. 417–26.

[51] ROSSI, A., F. ORSINI, A. SCORZA, F. BOTTA, N. BELFIORE and S. SCIUTO, 2018. A Review on Parametric Dynamic Models of Magnetorheological Dampers and Their Characterization Methods. Actuators. 7(2), 16-. DOI: 10.3390/act7020016. ISSN 2076-0825.

[52] GONCALVES F., KOO J. H. and AHMADIAN M. 2003 Experimental approach for finding the response time of MR dampers for vehicle applications DETC 2003 19th Biennial Conf. on Mechanical Vibration and Noise (Chicago, IL, Sept. 2003).

[53] STRECKER, Z., I. MAZŮREK, J. ROUPEC and M. KLAPKA, 2015. Influence of MR damper response time on semiactive suspension control efficiency. Meccanica. 50(8), 1949-1959. DOI: 10.1007/s11012-015-0139-7. ISSN 0025-6455.

[54] STRECKER, Z., J. ROUPEC, I. MAZŮREK and M. KLAPKA, 2015. Limiting factors of the response time of the magnetorheological damper. International journal of applied electromagnetics and mechanics. 47(2), 541-550. DOI: 10.3233/JAE-140006.

[55] KOO, J. H., F. D. GONCALVES and M. AHMADIAN, 2006. A comprehensive analysis of the response time of MR dampers. Smart Materials and Structures. 15(2), 351-358. DOI: 10.1088/0964-1726/15/2/015. ISSN 0964-1726.

[56] SAHIN, H., N. M. WERELEY, R. TAO, F. GORDANINEJAD, X. WANG and Y. LIU, 2012. Response time of magnetorheological fluids and magnetorheological valves under various flow conditions. Journal of Intelligent Material Systems and Structures. 23(9), 949-957. DOI: 10.1177/1045389X12447984. ISSN 1045-389X.

[57] BEWLEY, L. V. and H. PORITSKY, 1937. Intersheet Eddy-Current Loss in Laminated Cores. Transactions of the American Institute of Electrical Engineers. 56(3), 344-346. DOI: 10.1109/T-AIEE.1937.5057543. ISSN 0096-3860.

[58] BOTTAUSCIO, O., M. CHIAMPI and D. CHIARABAGLIO, Advanced model of laminated magnetic cores for two-dimensional field analysis. IEEE Transactions on Magnetics. 36(3), 561-573. DOI: 10.1109/20.846219. ISSN 00189464.

[59] FIORILLO, F., C. BEATRICE, O. BOTTAUSCIO and E. CARMI, 2014. Eddy-Current Losses in Mn-Zn Ferrites. IEEE Transactions on Magnetics. 50(1), 1-9. DOI: 10.1109/TMAG.2013.2279878. ISSN 0018-9464.

[60] MUKERJI, S. K., M. GEORGE, M. B. RAMAMURTHY and K. ASADUZZAMAN, 2008. Eddy Currents in Laminated Rectangular Cores. Progress In Electromagnetics Research. 83, 435-445. DOI: 10.2528/PIER08062101. ISSN 1559-8985.

[61] P/M Parts, ©2018. Sumitomo Electrics [online]. Sumitomo Electric Industries [cit. 2018-06-20]. http://global-sei.com/pmp/product_e/seihin01_eng.html.

[62] WANG, S., P. GAO, Y. HU and B. LI, 2017. A Novel Dual–Parallelogram Passive Rocking Vibration Isolator: A Theoretical Investigation and Experiment. Applied Sciences. 7(4), 367. DOI: 10.3390/app7040367. ISSN 2076-3417.

[63] GUO, C., X. GONG, L. ZONG, C. PENG and S. XUAN, 2014. Twin-tube- and bypass-containing magneto-rheological damper for use in railway vehicles. Proceedings of the Institution of Mechanical Engineers, Part F: Journal of Rail and Rapid Transit. 229(1), 48-57. DOI: 10.1177/0954409713497199. ISSN 0954-4097.

[64] NGUYEN, Q. H. and S.-B. CHOI, 2009. Optimal design of a vehicle magnetorheological damper considering the damping force and dynamic range. Smart Materials and Structures. 18(1), 015013. DOI: 10.1088/0964-1726/18/1/015013. ISSN 0964-1726.

[65] PATRASCU, D., How Magnetorheological Suspension Works. Autoevolution [online]. 2009 [cit. 2018-06-20]. https://www.autoevolution.com/news/how-magnetorheological-suspension-works-8947.html.

[66] KELSO, J. and E. LINDER. Magnetorheological Fluid Vibration Isolator. US20040195061 A1. 2004-10-07.

[67] CARUNTU, D. I. and C. SHOVE. Overview of payload vibration isolation systems.Proceedings of the ASME Design Engineering Division. New York: 2005.

[68] KUBÍK, M., O. MACHÁČEK, Z. STRECKER, J. ROUPEC and I. MAZŮREK, 2017. Design and testing of magnetorheological valve with fast force response time and great dynamic force range. Smart Materials and Structures. 26(4), 047002-. DOI: 10.1088/1361-665X/aa6066. ISSN 0964-1726.

[69] ALAM, M. N, A. AKHLAQ and N. RAHMAN. Dynamic analysis and vibration control of a multi-body system using MSC Adams. Latin American Journal of Solids and Structures. 2015, 12(8), 1505-1524. DOI: 10.1590/1679-78251598. ISSN 1679-7825.

[70] MACHÁČEK, O., M. KUBÍK and P. NOVÁK, 2017 A New Method of Magnetorheological Damper Quality Evaluation. In ENGINEERING

MECHANICS 2017. Praha: Institute of Thermomechanics Academy of Sciences of the Czech Republic, pp. 594-597. ISBN: 978-80-214-5497-2.

[71] Metal Bellows Manual, 2002. Witzenmann [online]. Pforzheim [cit. 2018-06-20]. https://www.witzenmann.de/en/media/Metal_bellows_manual_0441e_02_04_10_20_download.pdf.

[72] STRECKER, Z., J. ROUPEC, I. MAZUREK, O. MACHACEK, M. KUBIK and M. KLAPKA, Design of magnetorheological damper with short time response. Journal of Intelligent Material Systems and Structures. -. DOI: 10.1177/1045389X15591381. ISSN 1045-389x.

[73] Katalog olejů Paramo, 2007. Loziska.cz [online]. Pardubice: PARAMO [cit. 2018-06-20]. Dostupné z: https://www.loziska.com/store/katalog_paramo.pdf.

[74] *Vacuum schmelze*. 2017 [online]. Link: http://www.vacuumschmelze.de

[75] KUBÍK M.; MACHÁČEK O.; STRECKER Z.; ROUPEC J.; MAZUREK I.; KOUTNY D.; PALOUŠEK D., 2017. Struktura jádra obsahujícího pruty z feromagnetického materiálu a způsob jejího vytvoření. Czech Republic, PV 2017-91.

[76] MACHÁČEK, O.; KUBÍK, M.; MAZŮREK, I.; STRECKER, Z.; ROUPEC, J. Frictionless Bellows Unit Connected with the Magnetorheological Valve. In ENGINEERING MECHANICS 2016. First edition, 2016. Praha: Institute of Thermomechanics Academy of Sciences of the Czech Republic, 2016. s. 354-357. ISBN: 978-80-87012-59- 8.

[77] MRF-122EG, 2015. LORD MR Store [online]. Mid Atlantic Rubber [cit. 2018-06-20]. http://www.lordmrstore.com/lord-mr-products/mrf-122eg-magneto-rheological-fluid.

[78] RUAN, X., Y. WANG, S. XUAN a X. GONG, 2017. Magnetic field dependent electric conductivity of the magnetorheological fluids: the influence of oscillatory shear. Smart Materials and Structures. 26(3), 035067-. DOI: 10.1088/1361-665X/aa5fe5. ISSN 0964-1726.

[79] MACHÁČEK, O., 2017. Vývoj semiaktivního odpružení pro kosmonautiku. Brno. Pojednání k disertační práci. Brno University of Technology.

[80] WIJKER, Jaap J. Spacecraft structures. Berlin: Springer, c2008, 504 p. ISBN 35-407-5553-5.

9 LIST OF FIGURES